Engineered Graphene and Metal-Organic Framework Nanocomposites for Supercapacitor and Sensing Applications

A thesis submitted in fulfilment of the requirement for the degree of

Master of Philosophy

Chemical Engineering and Advanced Materials

by **Truc Van Ngo**

August 2019

THE UNIVERSITY of ADELAIDE

School of Chemical Engineering and Advanced Materials

Faculty of Engineering, Computer and Mathematical Sciences

The University of Adelaide, South Australia SA 5000, Australia

Dedication

To my parents

"**Hoa Van Ngo**" and "**Phuong Thi Lai**"

who are always beside me with their generous loves

&

To my beloved wife "**Trang Hong Pham**" and my mother-in-law "**Hong Dieu Truong**", who always motive me with their endless support

&

To my 7-year-daughter "**Kim Khanh Pham Ngo**, who is smart and cute.

Table of contents

Declaration

I certify that this thesis is my work conducted at the Losic Research Group, School of Chemical Engineering and Advanced Materials, Faculty of Engineering, Computer and Mathematical and Sciences (ECMS), The University of Adelaide under the supervision of Professor Dusan Losic and Dr Tran Thanh Tung. The thesis was completed in the allocated period of scholarship program as a full-time international student of the master by research (Master of Philosophy, MPhil).

I certify that this work contains no material which has been accepted for the award of any other degree or diploma in my name, in any university or other tertiary institution and, to the best of my knowledge and belief, contains no material previously published or written by another person, except where due reference has been made in the text. In addition, I certify that no part of this work will, in the future, be used in a submission in my name, for any other degree or diploma in any university or other tertiary institution without the prior approval of the University of Adelaide and where applicable, any partner institution responsible for the joint-award of this degree.

I acknowledge that copyright of published works contained within this thesis resides with the copyright holder(s) of those works.

I also give permission for the digital version of my thesis to be made available on the web, via the University's digital research repository, the Library Search and also through web search engines, unless permission has been granted by the University to restrict access for a period of time.

Name: Truc Van Ngo ID: 1697315

Signature: Date: 12 August 2019

Abstract

The thesis focuses on the preparation of pristine graphene (pG), graphene oxide (GO) and graphene oxide quantum dots (GOQDs), and their nanocomposites with metal-organic frameworks (MOFs) including Cu-1,3,5 benzenetricarboxylate (BTC) framework (HKUST-1), zeolitic imidazolate framework (ZIF-8), and $Zr_6O_4(OH)_4(C_8H_4O_4)_6$ framework (UiO-66), for supercapacitors and sensors applications. These engineered composite materials will find applications, firstly for supercapacitors; the GO/HKUST-1 composite material was laser-scribed, forming a novel morphology, highly porous and conductive L-rGO-C-MOF structure. As a result, the nano-porous architecture material displays a high capacitance of 390 F/g. Secondly, for sensor application, the pG-MOF nanocomposites show acceptable sensing responses towards different chemical vapours and their discriminations. In short, the thesis is dealing with extensive experiments of synthesis and characterisation of nanocomposite materials based on graphene derivatives and MOFs. The remarkable properties of these materials are expected to place them as promising materials for energy storage and sensing devices.

Acknowledgements

The completion of this Master of Philosophy (MPhil)'s thesis would not be possible without the enormous support of my supervisors, colleagues, and my family. I would like to express my immense gratitude to all who were always beside me and contributed to this success of my research journey in different ways.

The first and foremost, I would like to express my most profound gratitude to Prof. Dusan Losic, who greatly supervised, instructed and directed me from the beginning of my candidature. Without his support and supervision, there would not have my success today. Although I have been slow in my research progress due to lack of knowledge, research skills as well as personal issues such as language barrier and homesickness, he has encouraged and put his belief on me which made me more motivated and confident. Talking, discussing and sharing the ideas with him make me feel that he is like my second father who taught me from the fundamental issues of the research to the life outdoors. I would say that Prof. Dusan has forever been my sincere supervisor, and I wish him and his family all the warmest life and happiness. Secondly, I would also like to say thanks to my co-supervisor, Dr Tran Thanh Tung, who was acquainted with me when I studied at Ha Noi University of Science and Technology (HUST) (2003-2008). During my master program at The University of Adelaide, I have received a lot of enthusiastic support in many ways from him for the preparation of experiments to the characterization of samples, the analyses of results, etc. Once again, thanks to Dr Tung for everything he has done for me.

I would also like to thank Dr Diana Tran, who has given me a wide range of training sessions on different instruments which are fundamentally crucial for my research career, and all of my co-workers in the Losic Research Group, especially Dr Mahmoud Moussa, who has substantially supported me and taught me much about supercapacitors.

I would like to acknowledge the entire finance support of the 599-Master scholarship program sponsored by Vietnam Ministry of Education and Training and their joint-award cooperation program with the University of Adelaide. I acknowledge the support from the ARC Research Hub for Graphene Enabled Industry

Transformation, (IH150100003), the School of Chemical Engineering and Advanced Materials, the Adelaide Microscopy, The University of Adelaide for providing all materials and facilities during my research.

Last but not least, I would like to say thanks to my whole family, my parents “Hoa Van Ngo” and “Phuong Thi Lai”, my beloved wife “Trang Hong Pham”, my mother-in-law “Hong Dieu Truong”, my sisters “Cham Thi Ngo” and “Dung Thi Ngo” and my cute daughter “Kim Khanh Pham Ngo” for their constant support and sacrifice for my study in all ways.

I dedicate all the efforts I have made in my Master of Philosophy to five exceptional people in my life

To my parents “Hoa Van Ngo” and “Phuong Thi Lai” &

To my beloved wife “Trang Hong Pham”, my mother-in-law “ Hong Dieu Truong”

And lastly my lovely daughter “Kim Khanh Pham Ngo”.

List of Tables

List of Figures

Overview and thesis outline

The content of the thesis focuses on the engineering of new nanocomposite materials made of graphene and MOFs for applications in the field of supercapacitors and sensors. Graphene is a single layer of carbon atoms arranged in a hexagonal lattice, in which it owns excellent properties, e.g. high thermal and electrical conductivity, mechanical properties and high electron mobility [1-3]. These remarkable properties promote it as an ideal material for various practical applications, e.g. transparent and flexible thin films [4], semiconductors [5], energy storage [6] including supercapacitors [7-9], sensors [10-12]. However, graphene sheets usually restack, resulted in a decrease in its surface area and porosity, and therefore leading to unsatisfactory performance of these devices. Although much tremendous advancement of graphene-based materials has been made, the improvement of the energy density of graphene-based composite supercapacitors has still been a huge challenge. For chemical vapour sensing applications, the research on a new generation of graphene-based nanocomposites with desired structures and properties is rapidly developing but still in the early stage. The thesis aims to explore the potential applicability of graphene derivative-MOF composite materials for multiple practical applications with specific objectives: *first* - fabrication of a novel class of graphene-MOF (Copper-based MOF, HKUST-1) composite for high-performance supercapacitor, *second*- fabrication of a novel structure of HKUST-1@GQDs nanocomposite for a potential photoluminescent sensor, and *third* - fabrication of new nanocomposites of pG and various MOFs (HKUST-1, ZIF-8, and UiO-66) for chemical vapour sensors.

The outline of the thesis comprises five chapters, and the main content of each chapter is described as follows:

Chapter 1 provides the introductory information, background about the development of graphene and its derivatives, MOF materials, graphene-MOF composites, GQD-MOF composites and their related applications. Finally, the research gaps, aims and objectives are presented at the end of the chapter.

Chapter 2 introduces general information on materials preparation and characterisation techniques. Pristine graphene (PG), graphene oxide (GO), graphene (oxide) quantum

dots (GQDs or GOQDs), and HKUST-1 MOF were prepared, and they were used as the starting materials for other experiments in the following chapters. Besides, the general characterisation techniques for all composites and materials are illustrated regarding fundamental theory, sample preparation and the real instruments. These instruments include SEM, TEM, XRD, FTIR, TGA, UV-Vis spectrometer, Raman spectroscopy. The specific characterisations, such as electrochemical measurement, photoluminescent spectra and chemical vapour monitoring, are presented in the corresponding chapters.

Chapter 3 reports the synthesis of highly porous 3D structured graphene – HKUST-1 composites for a supercapacitor application, which corresponds to the first objective of the thesis. The composite was synthesised by the growth of HKUST-1 microrods into GO matrix. The new morphology of composite with microrods as the spacers in GO matrix was prepared and then post-treated by laser to form a porous structure of L-rGO-C-MOF, in which GO was reduced into L-rGO, and HKUST-1 microrods were carbonised into C-MOF. The hybrid structure of composite delivers a high porosity and surface area of the composite, which enhances the high performance of the supercapacitor. The high capacitance and energy density are achieved, indicating that the as-fabricated composite is potential for energy storage devices. The content of the chapter is used to write one research paper.

Chapter 4 reports the nanocomposites made of the GQDs and HKUST-1 for the promising application that corresponds to the second objective of the thesis. The GQD was synthesised by the ultrasonic shearing cutting method, which produced GQDs with their smallest diameter of ~30-50 nm corresponding to 15 h sonicating. The 15-h-sonicating-GQDs were then mixed with HKUST-1 microrods to form the nanocomposites. The UV-Vis and PL spectra indicate that the nanocomposites are promising for the optical sensing applications. However, more works and characterisations need to be done to explore the feasibility of practical applications of the materials.

Chapter 5 presents the nanocomposites made of pristine graphene and three types of MOFs (HKUST-1, ZIF-8, and UiO-66) for chemical vapour sensor that corresponds to the third objective of the thesis. The characterisations (XRD, SEM and TEM) of the pG-MOF nanocomposites show that MOF particles are intercalated into/onto the surface of

graphene, confirming the formation of nanocomposites. The sensing characterisation is conducted by a collaborated partner, the CNRS 6027, UBS, Lorient, France, where sensing characteristics are adequately monitored and investigated. The content of this chapter will be incorporated in a research paper as the co-author.

Chapter 6: Conclusions and future works briefly summarise the presented and discussed information, the potential works and future studies.

Publications from this Master of Philosophy project

1. Journal papers submitted:

Hybridization of MOFs and graphene: a new strategy for synthesis of porous 3D carbon composites for high performing supercapacitors.

Truc Van Ngo[1,2], Mahmoud Moussa[1,2], Tran Thanh Tung[1,2], Campbell Coghlan[1,2], Dusan Losic[1,2]*.

[1]School of Chemical Engineering, The University of Adelaide

[2]ARC Research Hub for Graphene Enabled Industry Transformation

The University of Adelaide, Adelaide, 5005 North Terrace, South Australia, Australia.

Corresponding author*

E-mail address: dusan.losic@adelaide.edu.au

Manuscript paper was submitted in Chemical Engineering Journal, 2019 (Elsevier).

2. Journal papers in preparation

Chemoresistive Sensors made of Graphene and Metal-Organic Framework Composites for VOC Biomarkers Analysis.

Tran Thanh Tung[1], Manh Trung Tran[2], Mickaël Castro[2], Jean-François Feller[2]*, Truc Van Ngo[1], Kamrul Hassan[1], Campbell J Coghlan[1], Md. J. Nine[1], Dusan Losic[1]*.

[1] School of Chemical Engineering, University of Adelaide, Adelaide, Australia

[2] Smart Plastics Group, Bretagne Loire University (UBL), IRDL CNRS 6027 – UBS, Lorient, France.

Corresponding: Prof Dusan Losic¸ School of Chemical Engineering, University of Adelaide, Adelaide 5005 SA, Australia; and Prof. Jean-François Feller, Bretagne Loire University (UBL), IRDL CNRS 6027 –UBS, Lorient, France.

Corresponding author*

E-mail address: dusan.losic@adelaide.edu.au

Manuscript paper is preparing for submission in Sensor and Actuator B, 2019 (Elsevier).

3. Other journal papers with my contribution out of this thesis

Facile synthesis of ternary graphene nanocomposites with doped metal oxide and conductive polymers as electrode materials for high performance supercapacitors

Saira Ishaq[1,2], Mahmoud Moussa[2], Farah Kanwal[1], Muhammad Ehsan[1], Muhammad Saleem[1], Truc Ngo Van[2], Dusan Losic[2*].

[1]Institute of Chemistry, University of the Punjab, Lahore 54590, Pakistan

[2]School of Chemical Engineering, ARC Research Hub for Graphene Enabled Industry Transformation, The University of Adelaide, Adelaide 5005, SA, Australia

Corresponding author[*]

E-mail address: dusan.losic@adelaide.edu.au

The paper was published in Scientific Reports, 12 April 2019.

< https://www.nature.com/articles/s41598-019-41939-y> or

< https://doi.org/10.1038/s41598-019-41939-y>.

References

1. Zhu, Y., et al., *Graphene and graphene oxide: synthesis, properties, and applications.* Advanced materials, 2010. **22**(35): p. 3906-3924.
2. Liu, Y., X. Dong, and P. Chen, *Biological and chemical sensors based on graphene materials.* Chemical Society Reviews, 2012. **41**(6): p. 2283-2307.
3. Li, X., et al., *Transfer of large-area graphene films for high-performance transparent conductive electrodes.* Nano letters, 2009. **9**(12): p. 4359-4363.
4. Eda, G., G. Fanchini, and M. Chhowalla, *Large-area ultrathin films of reduced graphene oxide as a transparent and flexible electronic material.* Nature nanotechnology, 2008. **3**(5): p. 270-274.
5. Kim, M., et al., *Fabrication and characterization of large-area, semiconducting nanoperforated graphene materials.* Nano letters, 2010. **10**(4): p. 1125-1131.
6. Han, S., et al., *Porous graphene materials for advanced electrochemical energy storage and conversion devices.* Advanced Materials, 2014. **26**(6): p. 849-864.
7. Wu Q, X.Y., Yao Z, Liu A, & Shi G*, *Supercapacitors Based on Flexible Graphene/Polyaniline Nanofiber Composite Films.* 2010.
8. Xu, Y., et al., *Holey graphene frameworks for highly efficient capacitive energy storage.* Nature Communications, 2014. **5**: p. 4554.
9. Yang, X., et al., *Liquid-mediated dense integration of graphene materials for compact capacitive energy storage.* Science, 2013. **341**(6145): p. 534-7.
10. Chen, G., T.M. Paronyan, and A.R. Harutyunyan, *Sub-ppt gas detection with pristine graphene.* Applied Physics Letters, 2012. **101**(5): p. 053119.
11. Dan, Y., et al., *Intrinsic Response of Graphene Vapor Sensors.* Nano Letters, 2009. **9**(4): p. 1472-1475.
12. Rumyantsev, S., et al., *Selective Gas Sensing with a Single Pristine Graphene Transistor.* Nano Letters, 2012. **12**(5): p. 2294-2298.

Chapter 1- Literature review

This chapter provides introductory information and previously reported studies about graphene and its derivatives, organic-metal framework (MOF) materials, graphene-MOF and graphene oxide quantum dots (GOQDs)-MOF nanocomposites from synthesis strategies to characteristics, and related applications for supercapacitors and sensors. This chapter also introduces the research gaps, aims and objectives of the thesis.

1.1 Background

2D structure and morphology

The structures of materials can be classified as the zero-dimensional (0D), one-dimensional (1D), two-dimensional (2D) and three-dimensional (3D). Examples of these structures are particles/dots, nanowires, and thin films, and bulk materials, respectively [1]. Amongst these classes of materials, 2D materials have emerged as promising candidates for many practical applications due to their unique structures and excellent properties. The 2D structure materials are defined as single-atomic-layer thick materials with strong in-plane chemical bonds, and they usually stack in multilayered materials in which the bonding between the layers is weak [2]. The isolation of monolayer graphene by mechanical exfoliation of bulk graphite was the first successful example confirming the formation of stable 2D materials. This discovery was awarded by Nobel prize in 2010. Following this discovery, many different sub-classes of 2D materials including transition metal-dichalcogenides (TMDs), hexagonal boron nitride (h-BN), and black phosphorus or phosphorene [3] have been developed as presented in Table 1.1 and Figure 1.1. However, the graphene family has been received much more attention over the other 2D families.

In graphene family that includes different forms such as pristine graphene (pG) and graphene oxide (GO), reduced GO, doped graphene, functionalized graphene, GOQDs or graphene quantum dots (GQDs) have been recently developed for various emerging applications due to their unique structure and excellent properties. Graphene, which is known as a ‘miracle material’, has recently attracted the significant interests of the worldwide scientific community due to its extraordinary structural, mechanical and electronic properties. Discovered in 2004 at Manchester University by Andre Geim and Konstantin Novoselov, who received the Nobel Prize in Physics in 2010, graphene has become one of the most attractive materials with many academic papers and scientific patents published yearly to discover its valuable properties for various potential applications [4].

Table 1.1 2D material family (Reproduced with permission from Ref.[5])

<table>
<tr><td>Graphene family</td><td colspan="2">Graphene</td><td>h-BN
“white graphite”</td><td>BCN</td><td>Flourographene</td><td>GO</td></tr>
<tr><td rowspan="3">2D chalcogenides</td><td colspan="2">MoS_2, WS_2, $MoSe_2$, WSe_2</td><td colspan="2">Semiconducting dichalcogenides: $MoTe_2$, WTe_2, ZrS_2, $ZrSe_2$, etc.</td><td colspan="2">Metallic dischalcogenides: $NbSe_2$, NbS_2, TaS_2, TiS_2, $NiSe_2$, etc.
Layered Semiconductors: GaSe GaTe, InSe, Bi_2Se_3 etc.</td></tr>
<tr><td>Micas, BSCCO</td><td>MoO_3, WO_3</td><td rowspan="2">Perovskite-type: $LaNb_2O_7$, $(Ca,Sr)_2Nb_3O_{10}$, $Bi_4Ti_3O_{12}$, $Ca_2Ta_2TiO_{10}$, etc.</td><td colspan="2">Hydroxides: $Ni(OH)_2$, $Eu(OH)_2$, etc.</td></tr>
<tr><td>2D oxides</td><td>Layered Cu oxides</td><td>TiO_2, MnO_2, V_2O_5 TaO_3 RuO_2, etc.</td><td colspan="2">Others</td></tr>
</table>

Stable monolayers under ambient conditions (room temperature in the air) are shaded blue; shaded green materials are probably stable in the air, and shaded pink materials are unstable in the air but maybe stable in an inert atmosphere. Successfully exfoliated 3D compounds down to monolayers, which are observed from Atomic force microscopy (AFM), are shaded grey. ‘Others’ include borides, carbides, and nitrides, and so on.

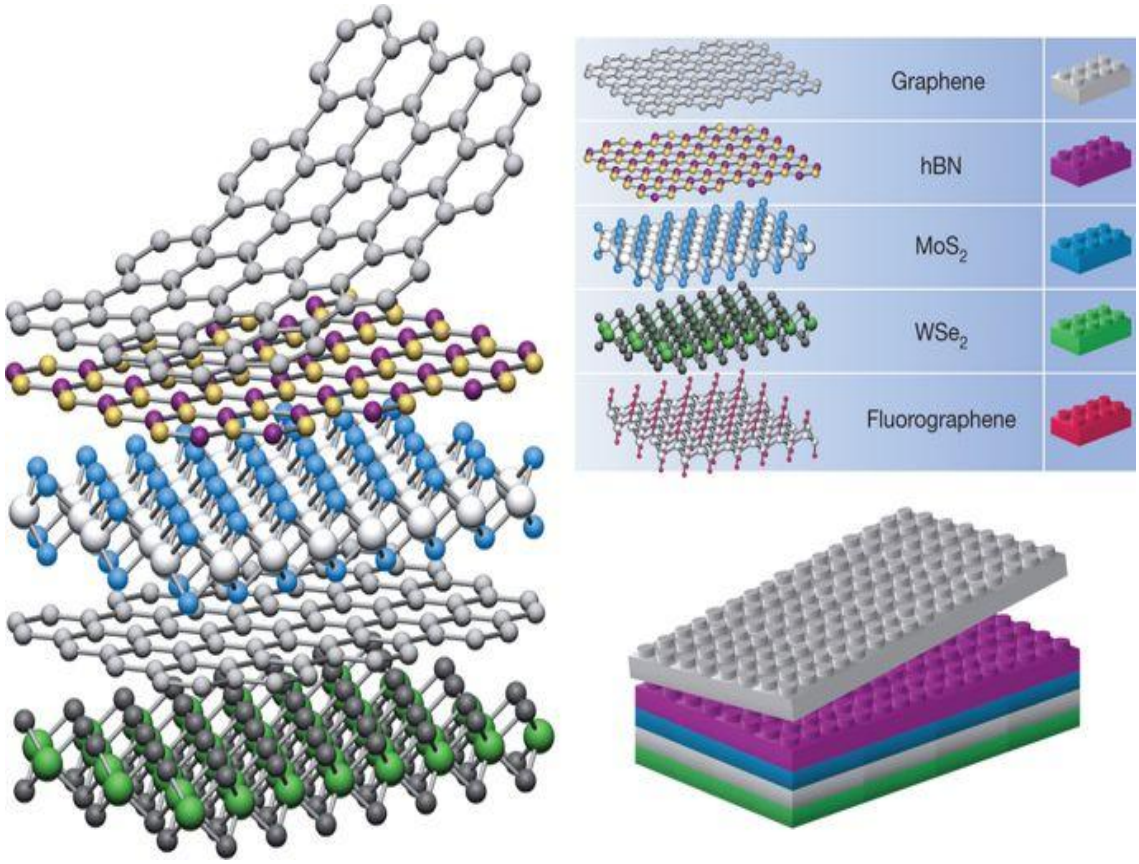

Figure 1.1 Models of Van der Waals structures. Structures of 2D crystals can be considered as Lego block (right panel). Conceptually, this atomic-scale Lego resembles molecular beam epitaxy but employs different "construction" rules and distinct sent of materials [5]. (Copyright Nature. Reprinted with permission from Ref. [5]).

1.2 Graphene and its derivatives

1.2.1 Graphene: structure and properties

a. Structure of graphene

Graphene is a one-atom-thick layer of honeycomb carbon network with the C-sp^2 hybridised chemical structure with carbon-carbon lengths of 1.42 A^o [6]. The s, p_x, p_y orbitals on each carbon form sp^2 hybridisation structure, and the p_z orbital overlaps with its three adjacent carbons to form π-orbitals [7]. Graphene is one of the millions of single layers in the graphite structure, which is orderly arranged. The interlayer bonding between graphene layers is only a weak van der Waals force. Also, the dimensionality of graphene is different from those of other allotropes of carbon, including fullerene (0D), CNTs (1D), bulk graphite (3D) as shown in Figure 1.2.

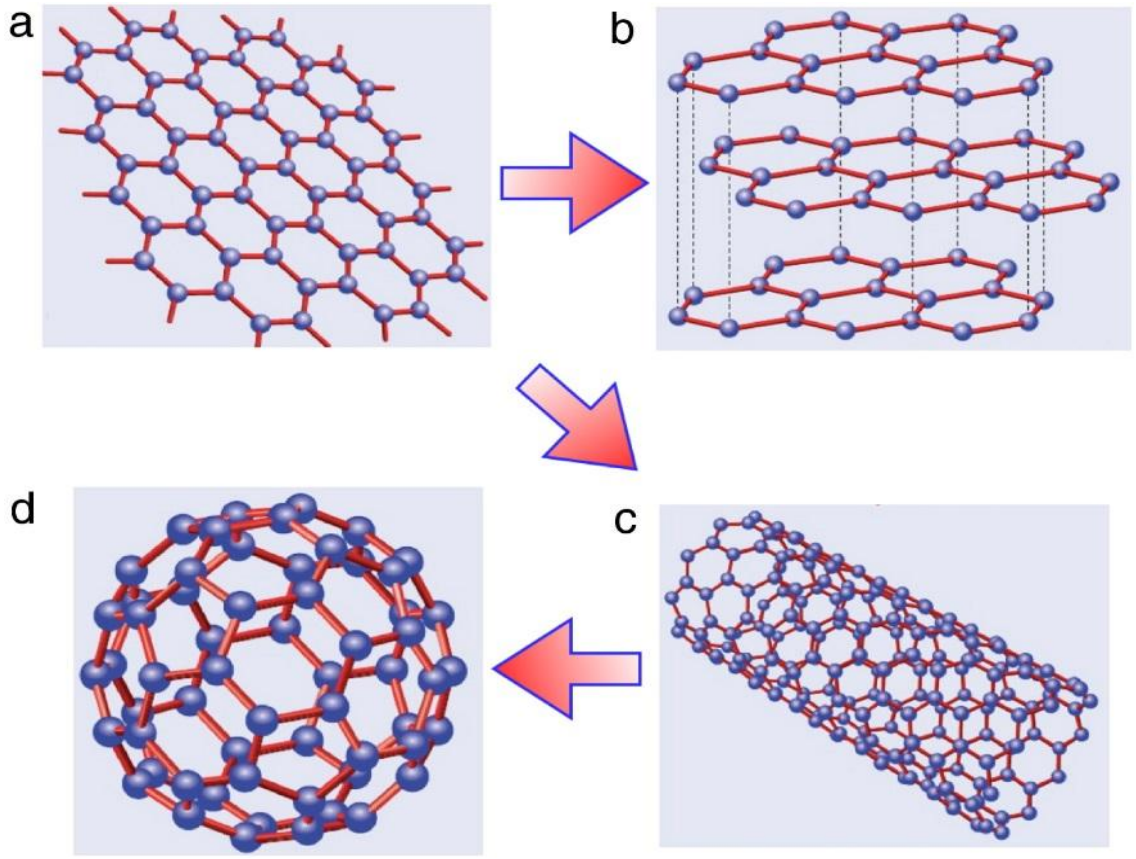

Figure 1.2 Schematic structures of (a) graphene, (b) graphite, (c) carbon nanotubes (CNTs) and (d) fullerene [8]. (Copyright Elsevier Ltd. Reprinted with permission from Ref. [8]).

b. Properties of graphene

The excellent properties of graphene results from the unique 2D structure, which make it different from fullerene, carbon nanotubes, and bulk graphite. A mono- or bilayer graphene is nearly transparent in the air with the optical transmittance of 97.7 % [9]. This excellent optical property has promoted it as a potential candidate for fabricating optical devices. Moreover, a single layer of graphene has a theoretically high surface area of 2630 m^2/g [10, 11], which is nearly twofold higher than that of single-walled carbon nanotubes (SWCNTs) and by far higher than those of most carbon black and activated carbon materials [12]. Therefore, the surface-volume ratio of graphene is high, which is crucial for applications in gas absorption and gas sensor. The pG, unlike 2D TMDs, is also a defect-free zero-bandgap material, which means no discontinuity in energy level between the conduction band and covalence band in their electron energy

configuration exists. This structural feature promotes graphene as an excellent thermal conductor with the high thermal conductivity of ~ 5000 *W/m.K*, and an exceptional electrical conductor with electron mobility of as high as $2x10^5$ m.V/s, and quantum Hall effect at the ambient temperature [11, 13]. Furthermore, graphene is the thinnest, strongest and hardest material with its theoretically high Young's modulus of up to 1060 MPa [11]. Nevertheless, graphene is not dispersible in water and many other organic solvents such as ethanol, acetone.

1.2.2 Graphene synthesis

Up to date, various methods have been developed to synthesise graphene, but in general, they can be categorised as top-down and bottom-up approaches. The top-down methods produce graphene by breaking the bulk graphite materials, while the bottom-up methods generate graphene by bonding carbon molecules, which are typically from alternative sources (i.e. chemical vapour deposition).

a.1 Top–down methods

In graphite material, single layers of graphene stacked together with the weak interlayer van der Walls force, and therefore they can be produced simply by breaking that physical interaction between them.

Micromechanical exfoliation

Micromechanical exfoliation was the first method to produce graphene from bulk highly ordered pyrolytic graphite (HOPG) by Geim and Novoselov in 2004 by using "Scotch tape" and discovered its outstanding properties [14]. In this method, the Scotch tape is applied to the surface of HOPG and then exerts a normal force. The graphitic layers are taken out of HOPG and adhere on the tape. The graphene layers are thinner and thinner by wrapping and rewrapping the tape several times, and finally, single-layer graphene is obtained. The procedure of the micromechanical method is described in Figure 1.3. Although this method is not suitable for mass production, it provides high-quality graphene sheets.

Liquid phase exfoliation

The phase liquid exfoliation was introduced by Coleman groups in 2008 to produce a high-yield production of graphene from graphite with the aid of sonication [15]. In their work, graphene dispersion is formed by dispersing graphite powers in specific organic solvents such as *N*, *N*-dimethylformamide (DFM) and N-methyl pyrrolidone (NMP), and the mixture is then sonicated and centrifuged. The results show that the fraction of monolayer graphene is estimated at ~28% among few-layer graphene production [15].

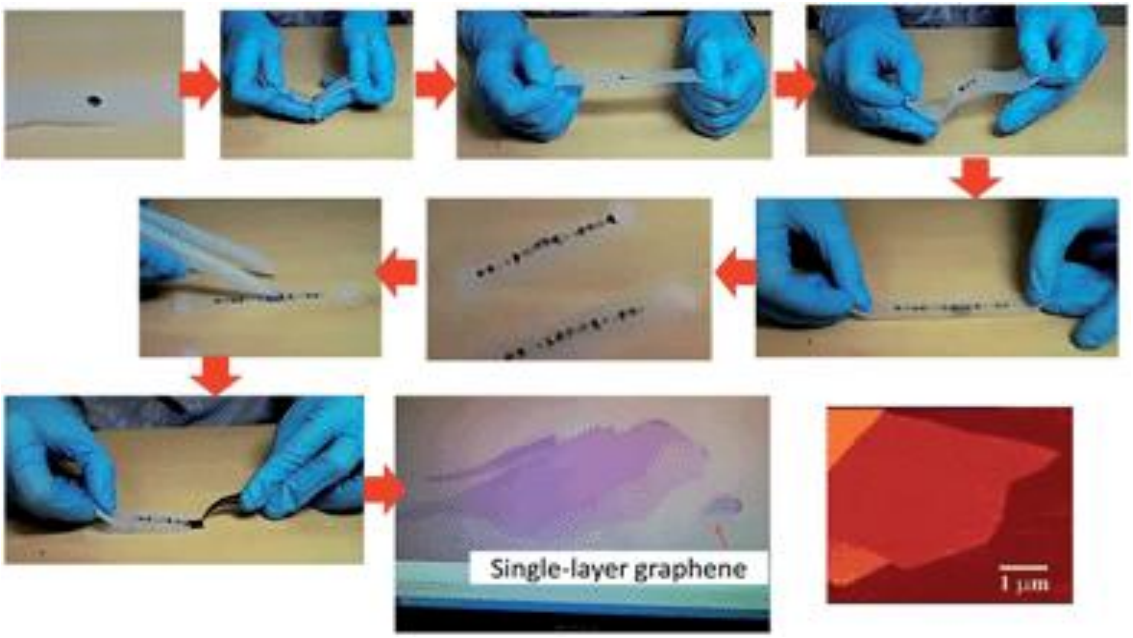

Figure 1.3 Micromechanical method used by Geim and Novoselov in 2004 for mechanical exfoliation of pristine graphene from graphite precursor. (Copyright Royal Society of Chemistry. Reprinted with permission from Ref. [16]).

In general, although the exfoliation yield of graphene is low, this method shows its low-cost and simplicity. Based on this method, many other works have been developed to increase the high-concentration of graphene by using surfactant/water solution [17], cationic surfactant [18], surfactant-stabilized [19], solvent exchange method [20], exfoliating graphene in ionic liquid polymer [21], ionic liquid [22], low-boiling point solvent [23], surfactant-free method [24], ultrasonic exfoliation with continuous surfactant addition [25], liquid phase noncovalent exfoliation method [26].

Electrochemical exfoliation

Electrochemical exfoliation is one of the most common methods to produce a massive mass production of graphene. The structure of this method consists of two electrodes, an electrolyte, and a potential is applied as an electrical source. When graphite reacts with chemicals, both covalent and ionic graphite intercalated compounds (GICs) are formed, and in ionic GIC intercalants can be either electron acceptors (H_2SO_4, HNO_3, $FeCl_3$, etc.) or electron donors (K, Rb, Li, etc.) [27]. The formation of GICs and the physical expansion of the graphite electrode are the base of electrochemical exfoliation method. There are two primary methods of preparation of graphene basing on the interaction of either anions or cations into graphite electrodes.

-Anodic preparation of graphene

In this method, graphite rods, platinum were used as an anode and counter electrode, respectively, and the electrolytes were concentrated sulfuric acids, chloro-and fluoro-sulphonic, selenic, perchloric and nitric acid, in which graphite was exfoliated to thin flakes of 20 layers [28, 29]. The requirement of mass production of graphene promoted the modification of electrolytes, voltage, time, and even concentration, etc. The other works are summarised in Table 1.2, and Figure 1.4 shows the mechanism of the anodic preparation method of graphene.

Table 1.2 A comparison of different works for anodic preparation of graphene

Electrolytes (solution)	Voltage (V)	Time (h)	Results	Ref.
Poly (sodium-4-styrenesulphonate) (PSS) solution	5	20 min	Graphene flake (1-2μm) lateral size	[30]
Sodium dodecylbenzene sulphonate (SDBS)	30	48	Graphene sheets (thickness of ca. 1.2nm)	[31]
	25	6		
Copper phthalocyanine tetrasulphonic acid	12	-	Graphene particles (1-6 layers)	[32]
6-amino-4-hydroxy-2-naphthalene-sulphonic acid mixed with NaOH	20	10-12	-	[33]

Ammonium sulphate ($(NH_4)_2SO_4$), sodium sulphate (Na_2SO_4), and potassium sulphate (K_2SO_4),	-	-	Flakes (>5 μm) ~ 85% (1-3 layers)	[34]

Some later works (not mentioned here) used sonication as the final step to obtain better-exfoliated graphene sheets.

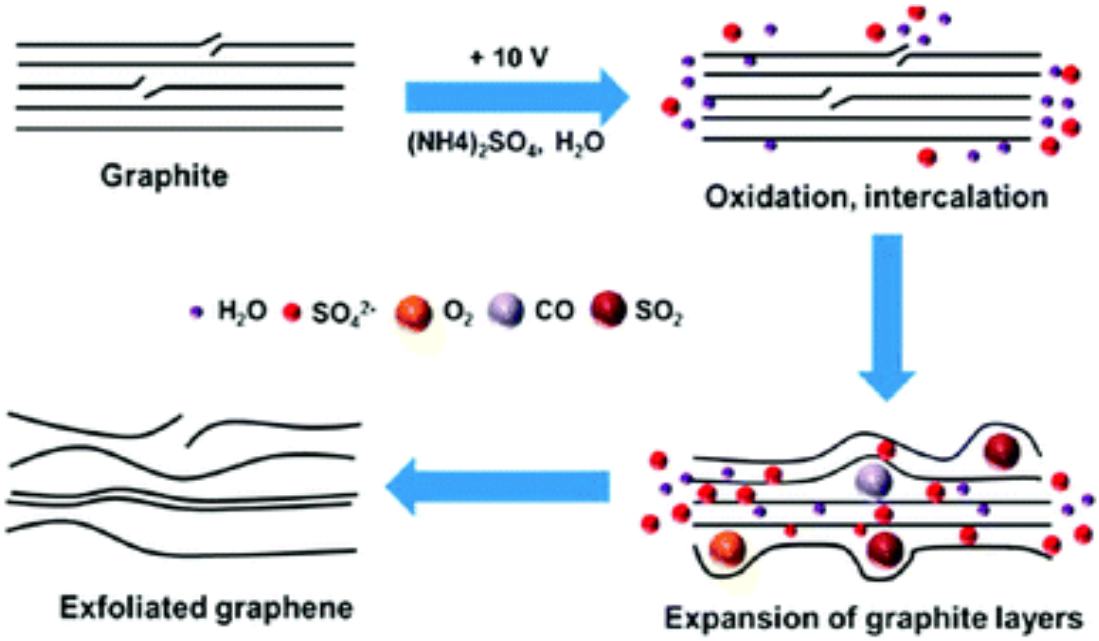

Figure 1.4 The concept of exfoliation through the intercalation of graphite with sulphate ions [34]. (Reprinted with permission from Ref. [34]. Copyright 2014 American Chemical Society).

-Cathodic production of graphene

Graphite has been used as negative electrodes in lithium-ion batteries for decades, in which lithium could be intercalated between graphene sheets [27]. The lithium-graphite substances were decomposed in aqueous solution, leading to the formation of graphene sheets, which worked as a base for the cathodic preparation of graphene. However, lithium exhibits a slow intercalation process; therefore, to produce graphene upon exfoliation in water, further intercalation, water decomposition and sonicating steps are needed to achieve complete exfoliation. Table 1.3 summaries the work followed the cathodic production of graphene.

Table 1.3 A comparison of different works for the cathodic production of graphene

Electrolytes (solution)	Voltage (V)	Sonication	Results	Ref.
NaCl, DMSO, and thionin acetate salt	5	yes	Stable graphene dispersion	[35]
A pure ionic liquid, N-butyl, methyl-pyrrolidinium bis(trifluoromethylsulfonyl)-imide (BMPTF2N)	-	yes	Defect-free graphene sheets (2-5 layers)	[36]
Lithium/propylene carbonate (PC)	In excess of -15	yes	-	[37]
Tetraalkylammonium salts	-2	-	Exfoliated materials (2 -5 layers)	[38]

Preparation of reduced GO

The abundant oxygen functional groups cause a high level of defects and disorder of graphene structure, and therefore, the electrical conductivity of graphene is sacrificed, which limits its applications in the electronic fields. As a consequence, to recover this property of pG, the reduction of GO is essential. The reduction of GO is the removal of oxygen functional groups by using either physical energy sources (e.g. thermal) or chemical reduction reactions to restore the structure of pG. After the reduction of GO, there will be a difference in visual observation, electrical conductivity, and the ratio of C/O. There have been various reduction methods of GO; however, they can be divided into two major categories: thermal reduction and chemical reduction. In the thermal reduction methods, the reducing agents are the thermal energy from different sources, for example, thermal annealing, microwave irradiation, while the chemical reduction methods use the chemical reducing agents such as hydrazine, hydroiodic acid (HI). These reduction methods are summarised in Table 1.4 below.

Table 1.4 Comparison of typical reduction methods of GO

Reduction method	Form of GO	C/O ratio	σ (S/cm)	Ref.
Chemical reduction				
Hydrazine hydrate	Powder	10.3	2	[40]
Hydrazine reduction	Film	NA	72	[41]
150mM $NaBH_4$ solution, 2 h	Film	8.6	0.045	[42]
Vitamin C	Film	12.5	77	[43]
55% HI reduction	Film	>14.9	298	[44]
Thermal reduction				
Thermal annealing, 1100ºC, UHV	Film	NA	~10^3	[45]
Thermal annealing, 1100ºC, Ar/H_2	Film	NA	727	[46]
Microwave irradiation	GO powder	NA	NA	[47]
Flash reduction (9 times)	Film	NA	10	[48]
Chemical-thermal reduction methods				
Hydrazine vapour	Film	~8.8	NG	[49]
Thermal annealing at 900ºC, UHV[a]		~14.1	NG	

a2. Bottom-up methods

Chemical vapour deposition (CVD)

This method base on the growth of graphene on substrates which are mainly metals such as copper (Cu) and nickel (Ni) as catalysts due to their low-cost, etchability and large grain size [39]. Generally, the method is conducted in a closed chamber or tube with carbon sources and at a high temperature. At elevated temperature, carbon sources such as CH_4, decompose to generate active carbon atoms which deposit on the surface of the substrate and form graphene due to the bonding of these atoms. The growth mechanism of graphene depends on the characteristics of substrates such as solubility of carbon in these substrates at the elevated temperature. The thin-film graphene is then obtained by removing substrates and washing. Figure 1.5 describes the typical CVD

method of graphene on Ni film substrate, the mechanism of graphene growth as well as the characteristics. The CVD methods of the growth of graphene on Ni and Cu substrates are listed in Table 1.5 and 1.6, respectively.

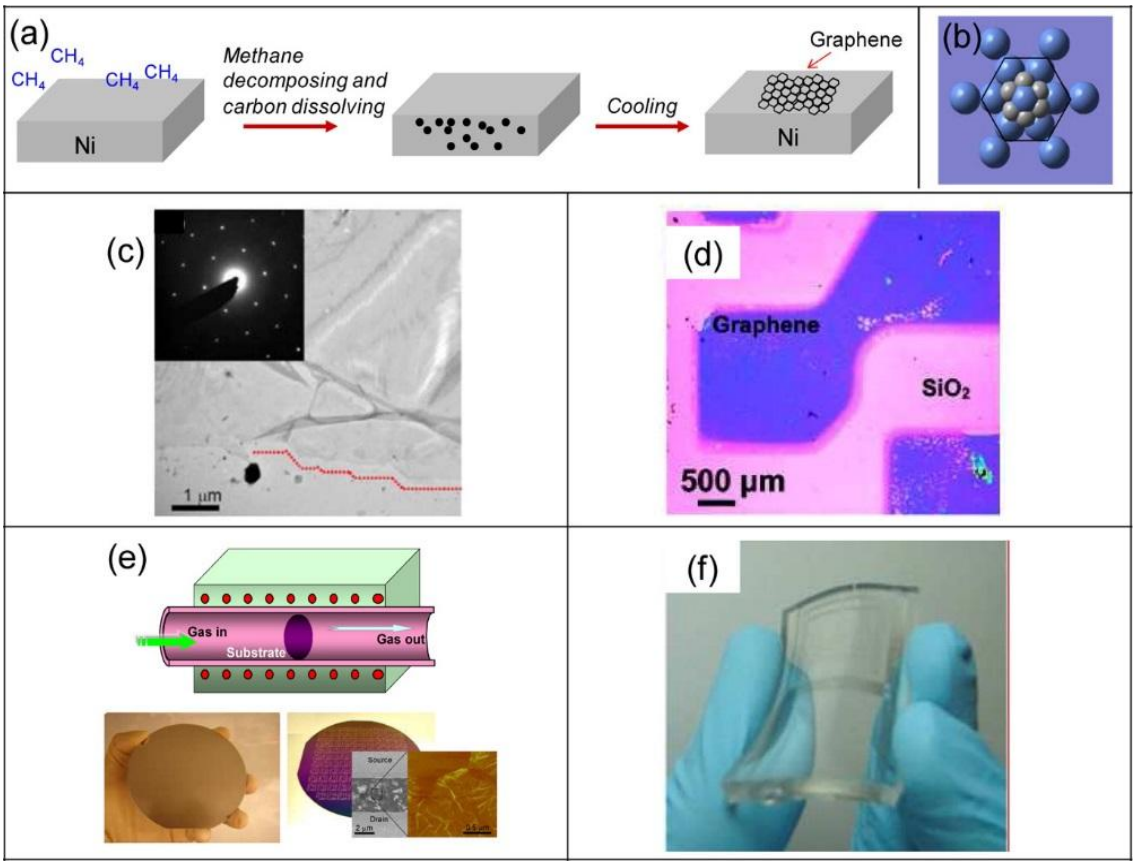

Figure 1.5 (a) Schematic diagram of graphene formation on Ni. (b) Schematic diagram of graphene lattice on Ni (111) lattice (larger atoms). (c) TEM image of graphene edges (adapted from ref [50]). (d) An optical image of graphene transferred from the Ni surface to SiO_2/Si substrate (adapted from Ref [51]. Copyright 2009 American Chemical Society). (e) Full-wafer scale deposition of graphene layers on polycrystalline Ni (adapted from ref [52]). (f) Transparent and flexible graphene films on the PDMS substrates (adapted from Ref [53]). Reprinted with permission from Ref [53*], Copyright 2013 American Chemical Society.

Table 1.5 Typical Ni film substrates in CVD of graphene

Ni film (thickness, nm)	**Growth conditions:** gas flow rate (standard cubic centimetres per minute-sccm), time (min), pressure (atm), temperature (ºC)	**Cooling condition** Cooling rate (ºC/s)	**No. of layers**	**Ref.**
Polycrystalline Ni foils (0.5)	CH_4 (15), H_2 (100), Ar (200), 1 atm, 20 min, 1000ºC	Cooling rates: fast (20), medium (10), slow (0.1)	3-4	[50]
Ni film on SiO_2/Si wafer, (500)	CH_4(5-25), H_2 (1500), 1 atm, 5-10 min, 900-1000 ºC	-	1-12	[51]
Ni film on SiO_2/Si wafer, (100)	CH_4(100), H_2(600), 1 atm, 8 min, 800 ºC	-	2-3	[52]
Ni film on SiO_2/Si wafer, (300)	CH_4(550), H_2(65), Ar (200), 7 min, 1000 ºC	10 in air	Mono & bilayer	[53]
Polycrystalline Ni film on SiO_2/Si wafer, (200)	0.4-4x10^{-3} Pa, 0-100 min, 1100 ºC	2-50	Mono & bilayer up to 95%	[54]

Table 1.6 Typical Cu film substrate in CVD of graphene

Growth conditions: gas flow rate (sccm), pressure (atm), time (min), temperature (ºC)	**Graphene morphology**	**Graphene grain size**	**Ref.**
CH_4(35), H_2(2), 500 mTorr, 30 min, 1000 ºC	Continuous	-	[55]
CH_4(50 ppm) in Ar (300), H_2(20), 1 atm, 20 min, 1050 ºC	Hexagonal	~18 μm	[56]
CH_4 (0.5), H_2(500), 1 atm, 15 min, 1045 ºC	Regular square	0.4x0.4 mm^2	[57]
CH_4 (0.5 & 1.3), 8 & 21 mTorr. H_2(2) 27 & 17 mTorr, 90 min, 1035 ºC	Hexagonal symmetry	~0.5 mm	[58]
CH_4(2), H_2(25), 200 mTorr, 30 min, 1000 ºC	Six-lobe flowers (four lobe flowers)	~100 μm	[59]
H_2 (10), CH_4 & alcohol, 10 mTorr, 20 min, 850 ºC, then 1 Torr,	Homogenous & uniform	3x3 cm^2	[60]

Plasma-enhanced chemical vapour deposition (PECVD)

PECVD of graphene is a variation of CVD, in which the thin film of graphene is formed upon the deposition of vapour of gases on the substrate under the energy created by plasma rather than heat energy. Therefore, PECVD method operates at a lower temperature than CVDs, and the plasma energy is generated from radio frequency (RF), microwave (MW) source, and direct current discharge (DCD) between two electrodes [61]. In a typical PECVD, the substrate is placed on an electrode directly facing the source of gas in a closed chamber. Under plasma energy, the gases are ionized and become reacting gases, which deposit on the surface of the substrate to form the thin films. The graphene thin film is then obtained by etching the substrate using organic solvents such as $FeCl_3$ salt. The PECVD methods of several typical works are presented in Table 1.7.

Epitaxial growth

Epitaxial growth method of graphene is the deposition of one crystalline graphene layer over a crystalline substrate, and this layer is called an epitaxial film. If the overlayer deposits on the substrate of the same material, it is called homoepitaxy, for example, Si on Si substrate; otherwise, it is called heteroepitaxy such as graphene on Si wafer. Generally, the epitaxial growth method is typically conducted at an elevated temperature in an ultrahigh vacuum (UHV) chambers and carbon sources involved to form highly oriented single crystals. The substrates in the epitaxial growth method are highly crystal materials, and they have high melting points. Table 1.8 summarizes the epitaxial growth methods of graphene on different substrates and growth conditions.

Table 1.7 Plasma-enhanced chemical vapour deposition (PECVD)

Plasma sources	**Growth conditions:** substrate, power (W), gas flow rate (sccm), time (min), pressure (atm), the temperature of the substrate (ºC)	**Graphene morphology**	**No. of layers**	**Ref.**
RF, 200W	1. Co film, H_2 (10), Ar (20), 13 Pa, then 220 Pa. 2. 800ºC, H_2(15) Ar (60), CH_4(3)	Horizontally grown	1-5	[62]
6kW, 2.5 GHz MW resonator	1. H_2 (200), 20 min, 2kW. 2. 700ºC, CH_4/H_2 (1/8, a total of 200), 2 kW, 40 Torr, 1-3000 sec	Vertical flakes	Few layers	[63]
3-5 kW MW generator	Cu foil, CH_4/Ar (30/10), CH_4/ Ar/H_2 (30/20/10), 3 or 5 Pa, 30-180 sec, <400ºC	Large-area film	-	[64]
Remote RF (13.56 MHz)	1. $CH_4 + NH_3$ (30% NH3, 46 mTorr), 700 ºC, 4 min 2. 650 ºC, 100 min.	Continuous film	Predominantly monolayer	[65]
2.45 GHz, 1400 W MW generator	Polycrystalline Ni foil, 450-750 ºC, 20 Torr, H_2/CH_4 (8/1 ratio)	Large area film	Monolayer	[66]
RF	Ni film, 650 ºC, CH_4 (2-8), 30-60 sec	Large area film	Single and multilayer	[67]
RF	1. Ni layer, H_2 (50), 5 min, 50 W 2. Ni foil (100nm), 380 ºC, $CH_4/Ar/H_2$, 10 min, 100W	Large area film	multilayer	[68]

Table 1.8 Epitaxial growth methods of graphene

Substrate	Epitaxial growth conditions Carbon source, pressure (atm), temperature (ºC)	No. of graphene layers	Ref.
n-typeHexagonal 6H SiC (0001)	1150-1400ºC, UHV	Few layers	[69]
Cu (111)	C_2H_4, 10^{-5} bar, ~1000ºC	Monolayer graphene	[70]
4H-SiC	1. H_2, 1600ºC. 2. 700ºC, $2x10^{-7}$ mbar. 3. 1475-1600ºC, 10 min	Few layers	[71]
Si-terminated 6H- or 4H SiC (0001)	1. 1100ºC. 2. 1200ºC or higher, 2 min, $5x10^{-9}$ mbar	Monolayer (1200ºC) Bilayer (1250ºC)	[72]
Ir (111)	C_2H_4, 10^{-11} mbar, 1500K	Monolayer	[73]
4H-SiC	~10^{-5} Torr, 1400ºC, 1 h	Large area film	[74]

Besides pG, there are many types of graphene materials, and they have been developed to meet the urgent demands of novel morphology, structure, properties, functionality, and applications. These materials are GO, rGO, GOQDs, GQDs N-doped graphene, functionalized-graphene, etc., and they play a crucial role in the development of graphene materials and their applicability in emerging applications of nearly all engineering fields in the current 21st century. The following paragraphs introduced two derivatives of graphene, which are GO, GQDs.

1.2.3 GO and reduced graphene oxide (RGO): structure, properties, and synthesis

GO is one important derivative of graphene. Unlike graphene, the structure of GO contains numerous oxygen functional groups such as hydroxyl (O-H), carbonyl (C=O), carboxyl (COOH) and epoxy (-O-) on its basal plane and edges [75]. Although GO was found later in comparison to graphene, it has been proven to significantly contribute to the development of graphene-based materials due to its practical applications. Besides, GO is also a valuable material to produce graphene, and the method of reduction of GO become one of the most effective and common approaches to restore the original

structure and properties of pristine graphene. Like graphene, GO has also received tremendous interest due to its unique properties and ability to host and react with chemical compounds to serve in specific applications, which may not be observed from pristine graphene. One of the most important physical properties of GO is its solubility in water and many organic solvents, which has promoted this material as an ideal candidate for synthetic material processes that a well-dispersed solution is a priority.

1.2.3.1 Structure and properties of GO

a. Structure of GO

The structure of GO consists of a matrix of a predominant domain of C-sp^3 carbon atoms and C-sp^2 carbon domains. The generated structure results from the oxidation of graphite layers in a strongly oxidized acidic environment. However, up to date, the exact structure of GO is still a controversial issue amongst scientists, and there have been many structures of GO given, in which GO structure in Figure 1.6 is the most widely accepted model so far.

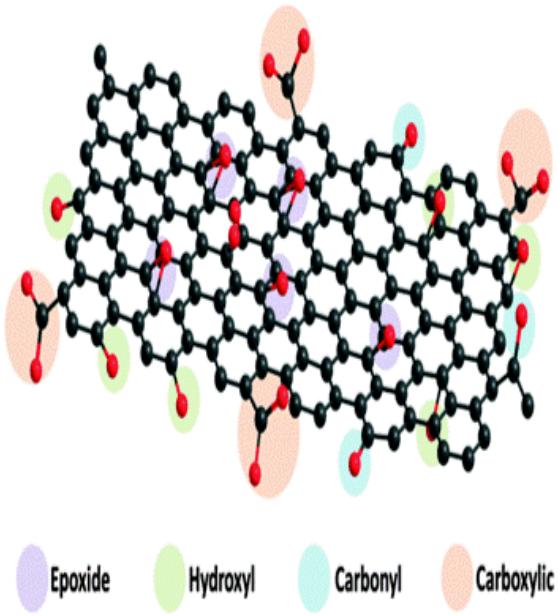

Figure 1.6 Schematic diagram of the GO structure including epoxide, hydroxyl, carbonyl and carboxyl groups [78]. (Copyright Elsevier Ltd. Reprinted from [78] with permission).

In this structure of GO, epoxy groups are stacked on the basal planes, and the other groups are attached on the edges. Pristine graphene sheets are stacked in graphite by weak van der Waal forces with d-spacing of two layers is 0.34nm [76]. However, this value in the GO structure significantly increases to 0.794 nm, which is confirmed by XRD at the diffraction angle of 11.1^{o} [77]. The increasing d-spacing is due to the contribution of oxygen functional groups and gives rise to the interlayer space between GO sheets. Therefore, GO can trap water and store them in its structure. Moreover, the oxygen functional groups of GO with negative and positive charges make GO soluble in water, and various solvents since there exist the hydrogen-bonding and electrostatic interactions between these functional groups with solvent molecules.

b. Properties of GO

Unlike graphene, GO is a semi-conducting material with a high level of defects, which results from chemical oxidation reactions to form oxygen-containing functional groups [77]. The C/O atomic ratio in the GO structure is ~2 [79]. The highly defect structure of GO leads to its low electrical conductivity, which limits it to be applied widely in electronic applications of GO. However, the electrical conductivity of GO is sacrificed; the functionalized structure of GO is a significant compensation regarding functionality and complex structure with underlying properties.

Reduced graphene oxide (RGO) is another form of GO, in which the oxygen functional groups are removed partially or mostly depended on different reduction methods. The C-sp^3 carbon atoms are reduced into C-sp^2 ones; therefore, RGO has a significantly recovered structure of graphene with fewer defects and an increase in electrical conductivity. Many reduction methods of GO have been presented previously.

1.2.3.2 Synthesis of GO

The dry and wet mediums are two main approaches employed to synthesise GO. The dry synthetic method conducted a chemical reaction between graphene and oxygen in ultrahigh vacuum conditions, while the wet path used graphite as the starting material [80]. The first GO was prepared by Brodie in 1959, by mixing graphite with potassium chloride ($KClO_3$) and nitric acid [81]. In 1898 Staudenmaier modified the Brodie's method by adding sulfuric acid (H_2SO_4), leading to a more oxidised graphitic material;

however, this method produced a toxic gas of ClO_2 [80]. In 1958 Hummer and Offeman proposed another approach, in which graphite was mixed with concentrated acid (H_2SO_4), sodium nitrate ($NaNO_3$) and potassium permanganate ($KMnO_4$), followed by addition of water and hydrogen peroxide (H_2O_2) to further oxidize and eliminate manganese from the suspension, and the final product was washed with warm water, but the GO amount is insignificant [82]. In 2010 Tour's group at Rice University had proposed an improvement of Hummer method, used a mixture of H_2SO_4/H_3PO_4 (9:1) and an increasing KMnO4 amount, and the resulting GO obtained has a higher hydrophilic degree in comparison with Hummer methods, no toxic gases (NO_2, N_2O_4, and ClO_2) generated [83]. Up to date, this method is still the most common approach employed to synthesise GO.

1.2.4 GQDs or GOQDs: structure, properties, and synthesis

a. Structure and properties of GQDs

GQDs are also another derivative of graphene. Generally, they are smaller fragments of graphene and GO, respectively, with their sizes of usually less than 100 nanometres, and typically around 20 nanometres (nm) [84]. It not only possesses the general properties of graphene or GO but also exhibits the quantum confinement and edge effects due to its small dimension. For example, GQDs with their diameters of around 10 nm exhibits the photoluminescence spectra owing to tuning the size, shape and the fraction of sp^2 domain in the sp^3 matrix [85]. Under an excitation energy source such as the laser, the free electrons confined in a narrow space are excited to jump up to the high energy level and then emit the photon to return its original energy state. This unique property promotes GQDs and GOQDs as potential candidates for sensing and bioimaging applications.

b. Synthesis of GQDs

Up to now, many synthetic methods of preparation of GQDs have been developed, and these approaches can be classified into two categories: top-down and bottom-up. The former cut the large graphene or GO sheets into smaller pieces, in which the method is low-cost, inexpensive, and straightforward, and therefore, it is more practical to synthesise the materials [84-86]. The latter bases on the growth mechanism of GQDs

molecules into the bigger one, but it requires advanced technology and high cost [86]. The schematic diagram of the top-down and bottom-up methods are illustrated in Figure 1.7.

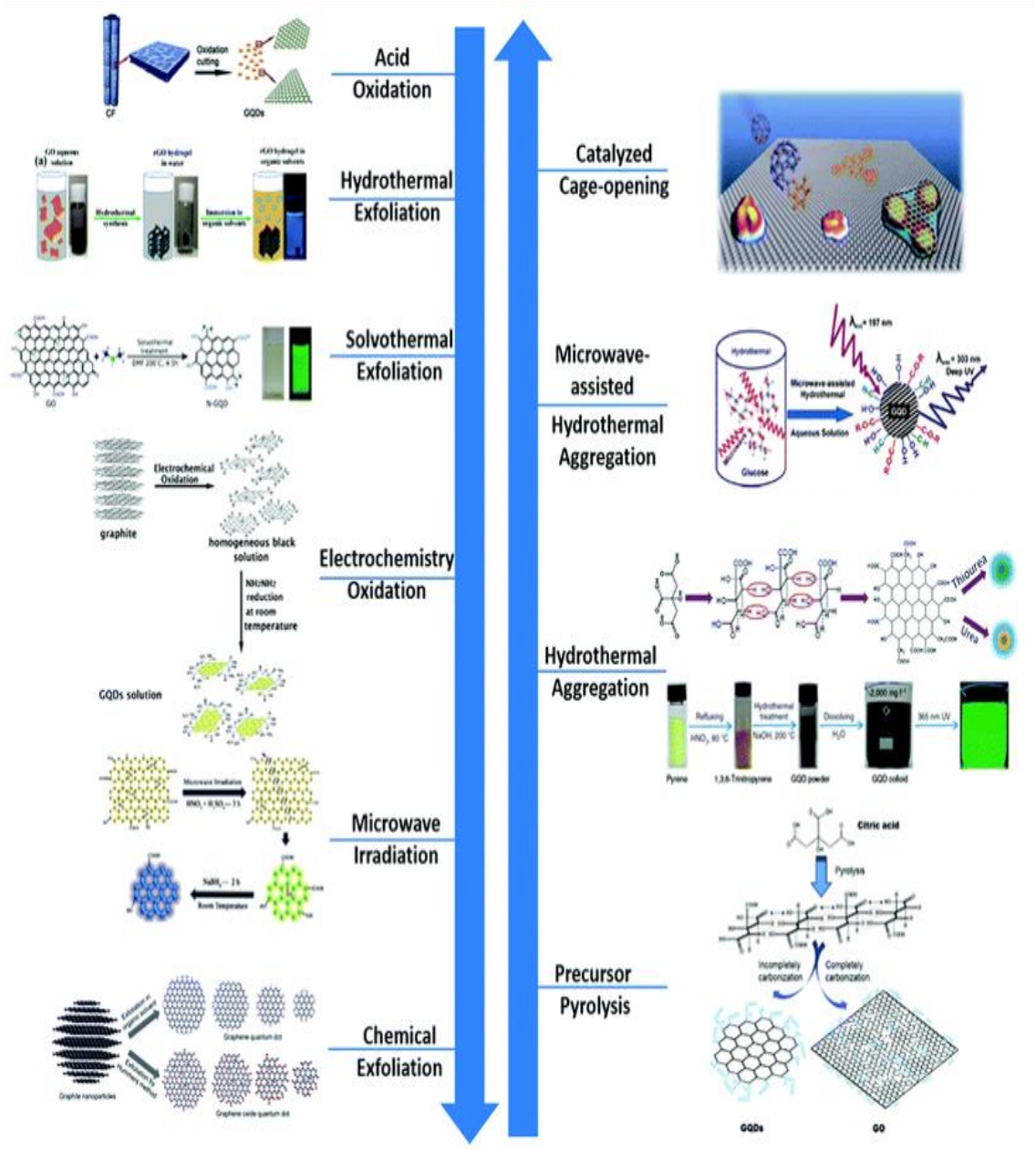

Figure 1.7 Top-down and bottom-up methods for synthesising GQDs [86]. (Copyright Royal Society of Chemistry. Reprinted with permission from Ref. [86]).

b.1 The top-down methods

The top-down synthetic method of GQDs is presented in Table 1.9 below.

Table 1.9 Top–down method for GQDs synthesis

Methods	**Conditions:** materials, chemicals	**QGDs diameter, properties**	**Ref.**
Microwave	H_2SO_4 & HNO_3, then $NaBH_4$	Blue-luminescent GQDs, 2-7 nm	[85]
Microwave radiation	GO, H_2SO_4 & HNO_3	GQDs, 2-5nm	[87]
	Ripped graphene sheets	GQDs, 9.6 nm average	[88]
Hydrothermal	Graphene hydrogels	GQDs, <4 nm	[89]
Solvothermal	GO	GQDs, ~5.3 nm	[90]
	GO, nitrogen source	N-GQDs, ~3 nm	[91]
Electrochemical oxidations	Graphite rods, 0.1 NaOH solution, Pt foil	GQDs, 5-10 nm	[92]
Electrochemical	Hydrazine	GQDs, epoxy & OH reduced	[93]
Liquid-phase exfoliation	Platelet graphite nanofibers, DMSO	GQDs, 10-30 nm	[94]
Chemical exfoliation	Graphite nanoparticles,	Monolayer GQDs, <4 nm	[95]
Ultrasonic	-	GQDs, 3-5 nm	[96]

b2. The bottom-up methods

The bottom-up methods of GQDs are summarised in Table 1.10

Table 1.10 Bottom-up method for GQDs synthesis

Method	**Conditions** Materials	**Diameter, properties**	**Ref.**
Metal-catalyzed cage opening	C_{60}, Ru (0001)	GQDs, ~2.7 nm	[97]
Molecular fusion	-	Single crystalline GQDs	[98]
Hydrothermal	GQDs, N & S sources	S, N-GQDs, 2.69-3.1 (±~0.5) nm	[99]
Tuning carbonisation of organic precursors	GO, NaOH, Citric acid	GQDs, ~15 nm	[100]
Pyrolysis	-	-	[101]

1.2.5 Applications of graphene and its derivatives

Besides graphene and its derivatives, other graphene-based materials, for example, element-doped graphene, functionalized graphene, graphene-based composites, etc., are attempted to include in this section. The applications of these materials are myriad and they are summarised in Table 1.11.

Table 1.11 Typical applications of graphene materials [102].

Engineering field	**Application**	**Percentage, %**
Electronics, devices	Semiconductors, transistor, RFIC, LEDs, etc.	27
Energy storage	Batteries, supercapacitors, solar cells, etc.	19
Sensors	Chemical, photoluminescent sensors, etc.	2
Coatings	Coating, packaging and paints	12
Healthcare	Drug delivery, diagnostics, etc.	3
Telecommunications	Antennas, Flexible display, touch panel, etc.	2
Automotive	Automotive, airplane components	3
Composites	Plastics, composites	17
Aerospace & defences	Wearable clothes etc.	15

1.3 Metal-organic framework (MOF) materials

MOF materials are a novel class of architecturally highly porous structure materials, which have been made from chemically strong bonds between metal ions (e.g. Cu^{2+}, Zn^{2+}, Co^{2+}, Mg^{2+}, Ni^{2+}, Al^{3+}) with organic ligands to yield architecturally 3D structures with identical pore size distribution [103].

1.3.1 Classification of MOFs

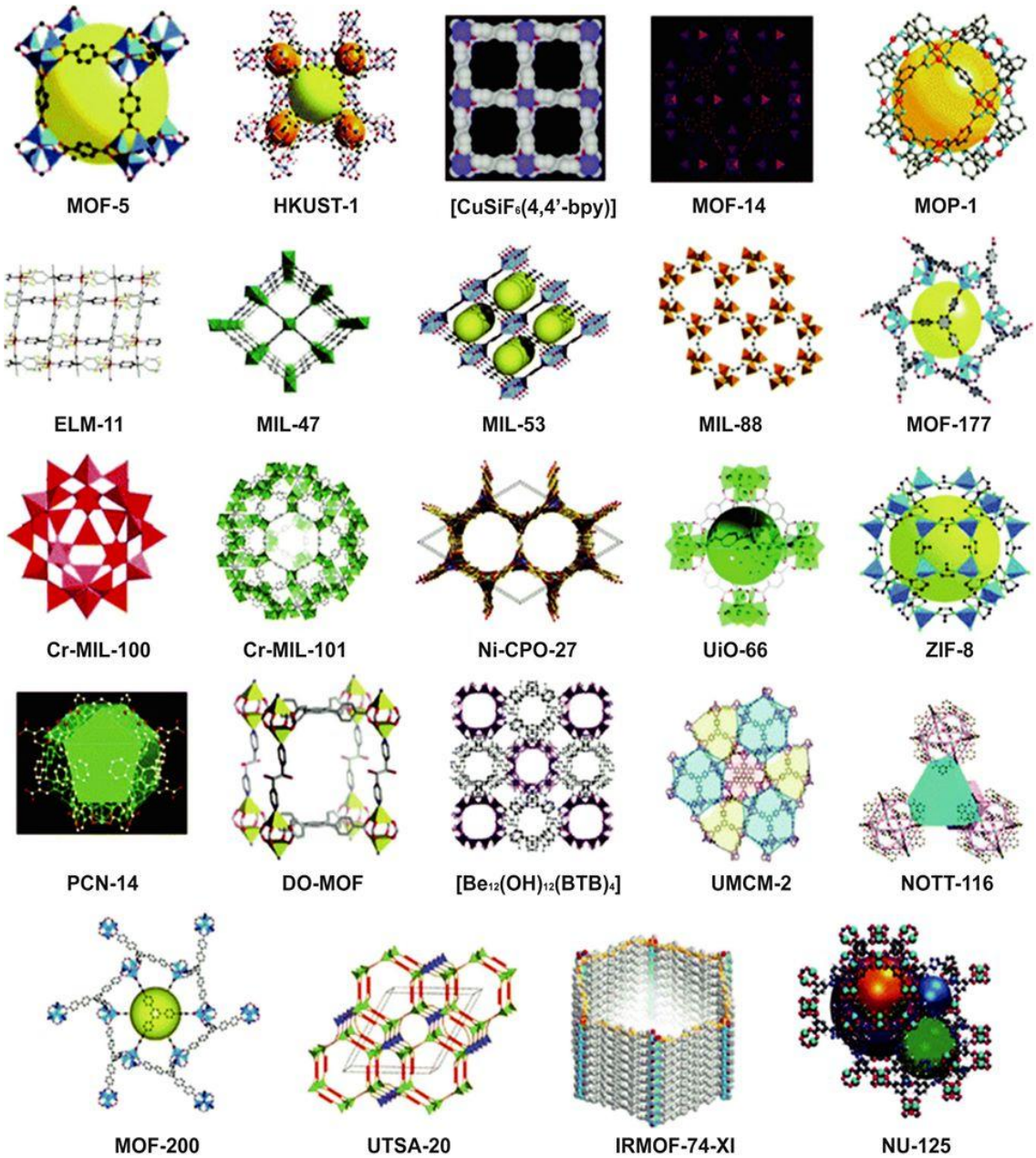

Figure 1.8 Classification of MOF structures [104]

(Copyright Elsevier. Reprinted with permission from Ref. [104]).

Many types of MOFs have been synthesised up to date, and Figure 1.9 shows the typical structures of MOFs materials.

In the thesis, three types of MOF materials, including Cu-based MOF (HKUST-1), zeolitic imidazolate framework (ZIF-8), and Zr-based MOF (UiO-66) are studied due to their popularity and potential applications in sensors and supercapacitors.

HKUST-1 is chemically built from paddle wheel dimeric copper carboxylate units and benzene-1,3,5-tricarboxylate groups to form with a 3D structure [105]. HKUST-1 materials exhibit a high surface area of 2260 m^2/g [106] and high porosity with a microporous volume of 0.27 cm^3/g [107]. However, they have low chemical stability, or they are even unstable in water [108]. ZIF-8s are chemically formed from 4-connected nets of tetrahedral units, in which metal ions (Zn^{2+}) are bonded through N atoms in ditopic imidazolate anions, with their surface area of 1250-1600 m^2/g [109]. UiO-66s, which are chemically made from 12-linked $[Zr_6(\mu_3\text{-}O)_4(\mu_3\text{-}OH)_4(O_2C)_{12}]$ cluster, terephthalic acid (BDC) and their isoreticular series, with a high surface area [110, 111]. UiO-66 exhibits high thermal and chemical stability [110].

1.3.2 Synthesis of MOF materials

Various methods of synthesising MOF materials are schematically shown in Figure 1.10. Liquid-phase methods are commonly employed for synthesising most types of MOFs, in which the reaction is conducted after mixing metal salt, ligand solution and solvents [112]. In these methods, the role of solvent is crucial in forming the structure of MOFs and their properties. Besides, the solid-phase methods are also applied as they are more rapidly and simple, but these methods suffer from achieving single crystals [112].

1.3.3 Applications

Due to excellent properties and unique structure with a high surface area, MOFs materials are employed in many applications and some of the significant applications are discussed below.

a. Light-emitting devices

This application bases on the ability of light emission of the MOF materials. The colour and intensity of emission depend on various factors, e.g., metal types, energy transport

process, etc. [113]. Liu *et al.* used the MOF of Tb(BTC)(H_2O).3H_2O: Eu^{3+} to investigate the colour change in respect with the concentration of Eu^{3+} ions, and the results show that from 0.1 to 10% Eu^{3+}, the green turned into green-yellow, orange, and red-orange [114].

b. Gas storage

The high porosity and high surface are the typical features of MOF structures. These characteristics make MOFs materials as the ideal candidates for gas storage application [115]. The synthesis conditions commonly used for MOF preparation (a) and the indicative summary of the percentage of MOFs synthesised using the various preparation routes are presented in **Table 1.12** below. A MOF = metal salt + ligant + solvent.

Table 1.12 Synthesis methods and the percentage of synthesised MOFs [112].

Synthesis methods				%
Methods	**Energy**	**Time**	**Temperature, ^oK**	
Solvothermal	Thermal energy	48-96 hr	353-453	~70
Microwave	Microwave radiation	4 min – 4 hr	303-373	~8
Sonochemical	Ultrasonic radiation	30-180 min	273-313	~4
Electrochemical	Electrical energy	10-30 min	273-303	~1
Mechanochemical	Mechanical energy	30 min – 2 hr	298	~3
Slow Evaporation	No external energy	7 days – 7 months	298	~14

c. Magnets

The application of MOF materials can be made upon the assimilation of magnetic moment carriers from their structure [116]. However, the interactions between these carriers are needed to complete form the magnetism of MOF materials.

d. Other applications: MOFs are also used for catalysts [117], drug delivery [118, 119], batteries and supercapacitors, recently [103, 120-127].

1.4 Nanocomposites made of graphene derivatives and MOFs and applications

This section presents the graphene derivatives-MOF materials and their applications.

1.4.1 Graphene –MOF nanocomposites

Composites can be mechanically defined as materials that constitute two different components. In chemical engineering, composites usually refer to the hybrid materials which are formed via chemical reactions or chemical modifications. The chemical structures of composites are a combination of both typical structures of their components, and therefore, the composites own both their components' characteristic properties. This combination usually makes these materials stronger, more stable, flexible, and consequently, they are more suitable for practical applications. Nanocomposites refer to composites at nano-scale. In general, the purpose of fabricating composites is to improve and enhance specific properties that are required for applications. Numerous strategies have been developed to advance the graphene-based composites, for instance, graphene-based polymer composites, graphene- metal/ceramic composites, graphene-based hybrid multicomponent composites [128].

Cooperation of graphene and MOF materials was possibly one valid approach to improve the electrical conductivity and surface area; therefore, the performance efficiency of electronic devices was enhanced. Graphene-MOF composites are the hybrid materials in which MOFs are grown into graphene matrix. These composites are ideal for applications such as gas absorption [129, 130], photo anodic [131], catalyst [132], etc. In the following paragraphs, the graphene-MOF composites for supercapacitors and sensors are presented.

a. Graphene-MOF nanocomposites for supercapacitors

In recent years, graphene and its derivatives (GO and RGO) have been attracted as the most common carbon-based materials for supercapacitor electrodes due to their mechanical durability, high electrical conductivity, large surface areas [133, 134]. However, porous graphene materials deliver capacitances of less than 200 F/g [135],

leading to a low energy density. Therefore, the high-performance supercapacitors with high capacitance, energy density, and long cycles, have not been satisfied with graphene materials only. However, the graphene-MOF composites for supercapacitors have recently attracted many research groups due to their significant improvement in the capacitance and energy density.

Srimuk *et al.* prepared a mesoporous rGO/MOF composite coated on carbon fibre paper for supercapacitor electrodes, which exhibit excellent electrochemical properties [136]. The 10% RGO /HKUST-1 composite has a high specific surface area of 1241 m^2/g and a specific pore volume of 0.78 cm^3/g, which delivers a capacitance of 385 F/g, a power density of 3100 W/kg, and an energy density of 42 Wh/kg [136]. Banerjee *et al.* produced a hybridization form of Ni-doped MOF-5/RGO composite with an improvement of its the electrical conductivity and the porosity of MOFs, in which electrode composites exhibited a high capacitance of 758 F/g and a power density of 227 W/kg at an energy density of 37.8 Wh/kg [137]. In another report, Cao *et al.* fabricated rGO–wrapped MoO_3 composites for solid-state flexible supercapacitors, which delivered a high capacitance of 617 F/g at 1 A/g, a power density of 55 W/kg at the energy density of 400 Wh/kg and a high cyclic retention of 87% after 6000 cycles [138]. A very high-performance supercapacitor was fabricated by Ni-MOF@ GO composite with GO content of 3%, showed a high capacitance of 2194.4 F/g at 1 A/g, and the cyclic retention of 85.1 % after 3000 cycles, but a low surface area of 126 m^2/g [139]. Wang *et al.* fabricated Co-MOF/rGO composites as supercapacitor electrodes, which exhibit a high specific capacitance of 1521.6 F/g at 0.2 A/g, and of 1117.6 at 12 A/g [140]. A flexible 3D composites in the solid-state of rGO/Fe_2O_3 aerogels obtained via a three-step process of hydrogel formation, free-dry and calcination phases, showed an excellent rate capability with a high capacitance of 869.2 F/g at 1 A/g as well as a long cycle life after 5000 cycles [141]. Also, in this report, rGO/Fe_2O_3 composite aerogels exhibited a high volumetric capacitance of 250 mF/cm^3 at 6.4 mA/cm^3 and cyclic retention of 96.3 % after 5000 cycles at 50.4 mA/cm^3 and high flexibility. Recently, Yu *et al.* prepared layer-by-layer structured MOF/GO composite films as supercapacitor electrodes, which deliver a high energy density of 50.5 Wh/kg at the power density of 853.3 W/kg [142].

b. Graphene-MOF nanocomposites for sensors

Although graphene and MOFs materials are employed to fabricate various types of sensors, including biosensors, electrochemical sensors [143] and electrochemical, optical, electronic, chemical, MOF sensors [144, 145], a limited number of composites made from both of them (graphene-MOF composites) have been fabricated for the sensing applications. Wang *et al.* prepared Cu-MOF/chitosan (CS)-RGO composite for detecting H_2O_2, in which Cu-MOF was formed on CS-rGO surface that results in a perfect electrochemical performance towards the reduction of H_2O_2 with a linear range of concentration (0.065-410 μM) and a low detection limit of 0.019 μM [146]. Yang *et al.* fabricated a sensitive glucose sensor from a hollow $CuCo_2O_4$ polyhedron/porous GO composite (Cu-Co-ZIFs-8/PrGO), in which Cu-Co-ZIF-8 grew and anchored onto PrGO sheets, providing various active sites and high electrocatalytic activity, of which the sensor exhibited a reasonable performance with a linear range of 0.5-3354 μM, and a low detection limit of 0.15 μM [147]. It indicates that graphene-MOF nanocomposites are still in the early stage, and further research is needed to discover the potentials of these materials in the sensing field.

c. Graphene-MOF nanocomposites for other applications

Besides two mainly focused applications mentioned above, graphene-MOF composites are promising materials for numerous applications due to their exhibited unique features, such as clearly defined crystal structures, high surface areas, tunable and porous structures. These materials have a potential application as an adsorbent material for the removal of organic dyes from aqueous solution [148], H_2S absorption [149], heterogeneous catalysts [150], etc.

1.4.2 GQD-MOF nanocomposites

Quantum dots-MOFs (QDs@MOFs) materials are one type of nanocomposites, in which QDs distributed into and bonded with MOFs molecules to form unique structures. Many types of these structures are shown in Figure 1.10. These materials include oxide-based QD@MOF, S/Se/Te-basedQD@MOF, nitride-based QD@MOF, carbon-based QD@MOF nanocomposites, and coordinating polymers as QDs. These nanocomposites and their applications are summarised in Table 1.13.

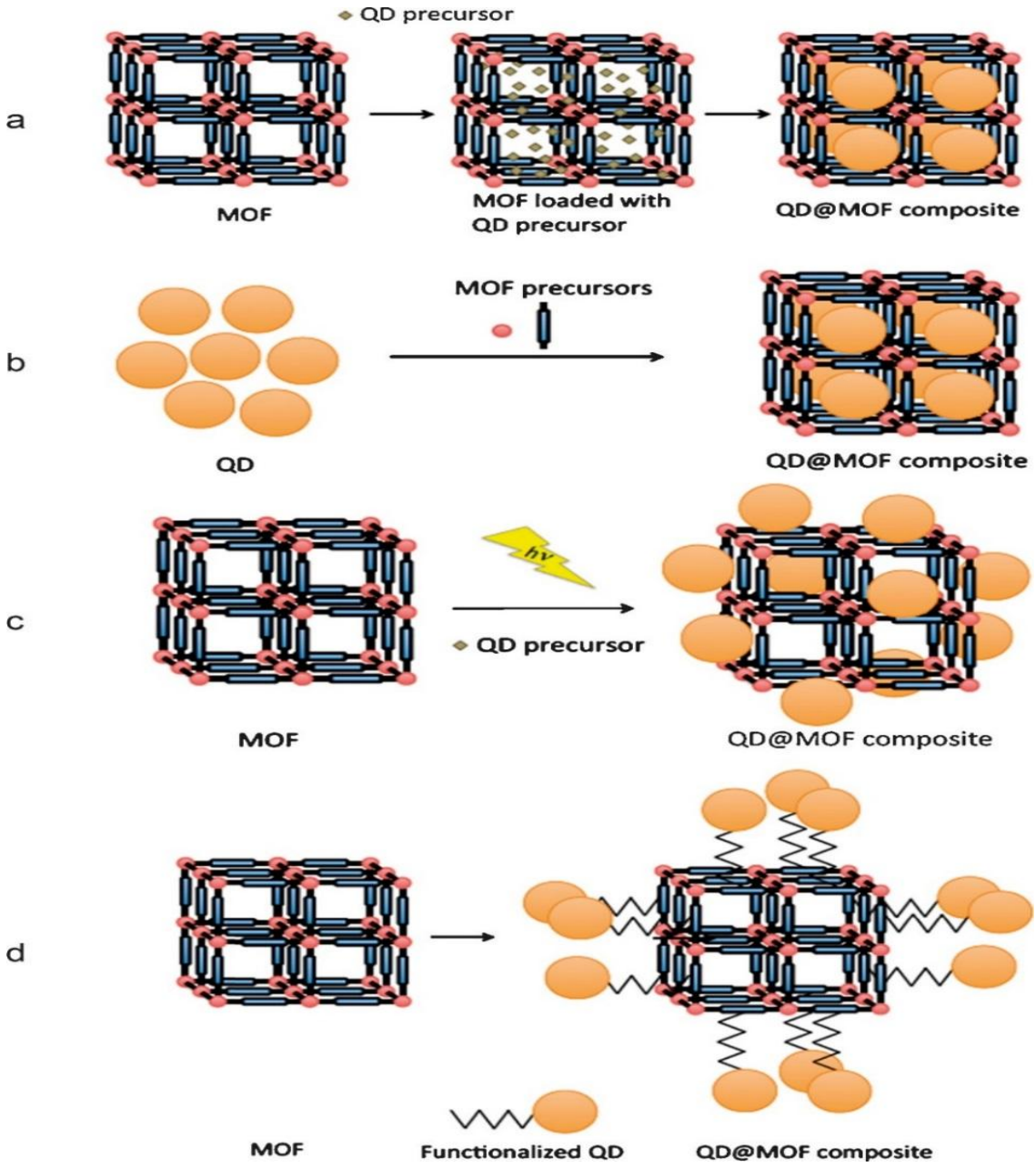

Figure 1.9 QD-MOF nanocomposite structures [151].

(Copyright Elsevier. Reprinted with permission from Ref. [151])

Table 1.13 Types of QD@MOF composites

QD	MOF	Application	Ref.
ZnO	MOF-5	Photocatalysis, catalysts, sensors	[152, 153] [154]
ZnO	ZIF-8	Photocatalysis, electrochemical sensors	[155] [156]
SnO2	ZIf-8	Supercapacitors	[157]
TiO2	HKUST-1	Photocatalysis	[158]
CdSe/CdS/cCd0.5Zn0.5S/ZnS	MOF-5	Fluorescent sensing	[159]
CdSe	EuOF	Sensing	[160]
CdTe	ZIF-8	Sensing	[161]
CdS	MIL-101	Hydrogen evolution	[162]
CdS	UiO-66, UiO-66-NH2	Hydrogen evolution, selective photocatalysis	[163, 164]
CdSe/ZnS	F-MOF, DA-MOF	Light-harvesting	[165]
C-dots	ZIF-8	Sensing, drug-delivery fluorescence imaging	[166] [167]
GQDs	PZn	Cellular probes	[168]

Although QDs@MOF nanocomposites have been fabricated for numerous applications; however, there has been only one report about the GQD@MOF nanocomposites for the cellar probes, raising the demand for the fabrication of these nanocomposite materials for promising applications such as sensing.

1.5 Research gaps

a. Supercapacitor: the urgent demands for development of the lightweight, flexible and wearable electric devices have motived the discovery of the new design of composite materials for energy storage devices. As analysed in the literature review, the low energy density is one major drawback of graphene-based materials for supercapacitors. Although the design of graphene-based MOF composites has been developed recently, the challenge still exists, and therefore, it is essential to improve the current status of graphene-MOF composites by designing the new structures of materials, and as a result, new properties or enhancing properties can be achieved.

b. GQDs and GQD-MOF nanocomposites for promising applications

GQDs exhibit many unique properties, such as quantum confinement and edge effects due to their small sizes. Similarly, MOF materials are also excellent candidates for sensing purposes due to their unique structure and electron transfer effect in their structures. Up to date, the work on GQD-MOF composite for sensing and other applications is rare. The GQD-MOF composites are expected to bring out a new design of nanocomposite which can benefit advances of GQDs and MOFs in order for them to be applied to potential applications such as sensing and catalyst, etc.

c. Graphene–MOF nanocomposites

The current development of graphene-MOF nanocomposites for sensing purposes is still in the early stage with an insignificant number of reports. Graphene-MOF nanocomposites show high surface areas, high porosity, with functionalities on their structures, which are suitable to use as sensing probes for detecting gas, vapour, etc. These properties result from the combination of graphene and MOF structures, which can be more beneficial in comparison with graphene only or MOF only for the same sensing purposes. Hence, it is crucial to research this topic to contribute to the current development of gas sensing applications of the graphene-based nanocomposites.

1.6 Aims and objectives of the thesis and thesis outline

The thesis aims to explore the potential applicability of graphene derivatives-MOF composites for practical applications.

The aims of the thesis are:

Aim 1: Engineering a new class of graphene-MOF composite materials for energy storage devices (chapter 3).

Objective 1: Fabrication of highly porous 3D structured graphene- HKUST-1 composites for high-performing supercapacitors, using the laser as the friendly-environmentally and ultrafast treatment technique.

Aim 2: Designing a new type of GQD – MOF composites for photoluminescent sensing applications (Chapter 4).

Objective 1: Fabrication of GQD-HKUST-1 composites and the characterisation of their optical properties, and explore the potential application for the optical sensors.

Aim 3: Designing a new nanocomposite of graphene-MOF for chemical sensing applications (chapter 5).

Objective 1: Fabrication of three pG-MOF nanocomposites and explore the application for chemical vapour sensors.

1.7 Significance and novelty

Significance

The work in the thesis provides the fundamentals of graphene and its derivatives, MOF materials, and the composites of graphene-MOF composites. Furthermore, the thesis also provides findings of the practical applications for supercapacitors and chemical vapour sensors. For the supercapacitor applications, the energy density of electrode materials was significantly improved, and this improvement contributes to the development of the graphene–MOF composites for supercapacitors. For chemical vapour sensing applications, the results indicate the acceptable responses of the fabricated sensors to the different chemical vapours (i.e. methanol, ethanol).

Novelty

Firstly, the thesis presents a new approach to fabricate the graphene-MOF composites by combining these individual materials using the mechanical method, which is simple,

facile and effective. Another novelty in the thesis is the use of the CO_2 laser as the advanced technique to reduce and carbonise the GO-HKUST-1 composite, with its simplicity, effectiveness, ultrafast and friendly- environmentally features. Moreover, the fabrication of a new GQD-HKUST-1 composite material with their promising optical properties also contributes to the development of the graphene–based composites for emerging applications.

References

1. Mas-Ballesté, R., et al., *2D materials: to graphene and beyond.* Nanoscale, 2011. **3**(1): p. 20-30.
2. Gupta, A., T. Sakthivel, and S. Seal, *Recent development in 2D materials beyond graphene.* Progress in Materials Science, 2015. **73**: p. 44-126.
3. Akinwande, D., et al., *A review on mechanics and mechanical properties of 2D materials—Graphene and beyond.* Extreme Mechanics Letters, 2017. **13**: p. 42-77.
4. Lee, H.C., et al., *Synthesis of Single-layer Graphene: A Review of Recent Development.* Procedia Chemistry, 2016. **19**: p. 916-921.
5. Geim, A.K. and I.V. Grigorieva, *Van der Waals heterostructures.* Nature, 2013. **499**: p. 419.
6. Lonkar, S.P., Y.S. Deshmukh, and A.A. Abdala, *Recent advances in chemical modifications of graphene.* Nano Research, 2014. **8**(4): p. 1039-1074.
7. Allen. J M, T.V.C., and Kaner. R B *Honeycomb Carbon: A Review of Graphene.* Chemical Reviews, 2010. **110**.
8. Tetlow, H., et al., *Growth of epitaxial graphene: Theory and experiment.* Physics Reports, 2014. **542**(3): p. 195-295.
9. Cui, X., et al., *Liquid-phase exfoliation, functionalization and applications of graphene.* Nanoscale, 2011. **3**(5): p. 2118-2126.
10. Han, S., et al., *Porous graphene materials for advanced electrochemical energy storage and conversion devices.* Advanced Materials, 2014. **26**(6): p. 849-864.
11. Zhu, Y., et al., *Graphene and graphene oxide: synthesis, properties, and applications.* Advanced materials, 2010. **22**(35): p. 3906-3924.
12. Chen, J., C. Li, and G. Shi, *Graphene materials for electrochemical capacitors.* The journal of physical chemistry letters, 2013. **4**(8): p. 1244-1253.
13. Wang, S.J., et al., *Fabrication of highly conducting and transparent graphene films.* Carbon, 2010. **48**(6): p. 1815-1823.
14. Novoselov, K.S., et al., *Electric Field Effect in Atomically Thin Carbon Films.* Science, 2004. **306**(5696): p. 666-669.
15. Hernandez, Y., et al., *High-yield production of graphene by liquid-phase exfoliation of graphite.* Nature Nanotechnology, 2008. **3**: p. 563.
16. Yi, M. and Z. Shen, *A review on mechanical exfoliation for the scalable production of graphene.* Journal of Materials Chemistry A, 2015. **3**(22): p. 11700-11715.
17. Lotya, M., et al., *Liquid Phase Production of Graphene by Exfoliation of Graphite in Surfactant/Water Solutions.* Journal of the American Chemical Society, 2009. **131**(10): p. 3611-3620.
18. Vadukumpully, S., J. Paul, and S. Valiyaveettil, *Cationic surfactant mediated exfoliation of graphite into graphene flakes.* Carbon, 2009. **47**(14): p. 3288-3294.
19. Lotya, M., et al., *High-Concentration, Surfactant-Stabilized Graphene Dispersions.* ACS Nano, 2010. **4**(6): p. 3155-3162.
20. Zhang, X., et al., *Dispersion of graphene in ethanol using a simple solvent exchange method.* Chemical Communications, 2010. **46**(40): p. 7539-7541.
21. Zhou, X., et al., *Dispersion of graphene sheets in ionic liquid [bmim][PF6] stabilized by an ionic liquid polymer.* Chemical Communications, 2010. **46**(3): p. 386-388.
22. Nuvoli, D., et al., *High concentration few-layer graphene sheets obtained by liquid phase exfoliation of graphite in ionic liquid.* Journal of Materials Chemistry, 2011. **21**(10): p. 3428-3431.
23. O'Neill, A., et al., *Graphene Dispersion and Exfoliation in Low Boiling Point Solvents.* The Journal of Physical Chemistry C, 2011. **115**(13): p. 5422-5428.
24. Li, J., et al., *A simple route towards high-concentration surfactant-free graphene dispersions.* Carbon, 2012. **50**(8): p. 3113-3116.

25. Notley, S.M., *Highly Concentrated Aqueous Suspensions of Graphene through Ultrasonic Exfoliation with Continuous Surfactant Addition.* Langmuir, 2012. **28**(40): p. 14110-14113.
26. Xu, L., et al., *Production of High-Concentration Graphene Dispersions in Low-Boiling-Point Organic Solvents by Liquid-Phase Noncovalent Exfoliation of Graphite with a Hyperbranched Polyethylene and Formation of Graphene/Ethylene Copolymer Composites.* The Journal of Physical Chemistry C, 2013. **117**(20): p. 10730-10742.
27. Abdelkader, A.M., et al., *How to get between the sheets: a review of recent works on the electrochemical exfoliation of graphene materials from bulk graphite.* Nanoscale, 2015. **7**(16): p. 6944-6956.
28. Siecke, W.R.a.W.-F., Chem. Ber, 1958. **91**: p. 1348–1354.
29. M. J. Bottomley, G.S.P., A. R. Ubbelohde and and D. A. Young, *Electrochemical Preparation of Salts from Well-oriented Graphite.* J. Chem. Soc., 1963: p. 5741–5745.
30. Wang, G., et al., *Highly efficient and large-scale synthesis of graphene by electrolytic exfoliation.* Carbon, 2009. **47**(14): p. 3242-3246.
31. Li, P., et al., *One-Step Process for the Exfoliation and Surface Modification of Graphene by Electrochemical Method.* Advanced Materials Research, 2010. **123-125**: p. 743-746.
32. Mensing, J.P., et al., *Facile preparation of graphene–metal phthalocyanine hybrid material by electrolytic exfoliation.* Journal of Materials Chemistry, 2012. **22**(33): p. 17094-17099.
33. Kuila, T., et al., *One-step electrochemical synthesis of 6-amino-4-hydroxy-2-napthalene-sulfonic acid functionalized graphene for green energy storage electrode materials.* Nanotechnology, 2013. **24**(36): p. 365706.
34. Parvez, K., et al., *Exfoliation of Graphite into Graphene in Aqueous Solutions of Inorganic Salts.* Journal of the American Chemical Society, 2014. **136**(16): p. 6083-6091.
35. Zhou, M., et al., *Few-layer graphene obtained by electrochemical exfoliation of graphite cathode.* Chemical Physics Letters, 2013. **572**: p. 61-65.
36. Yang, Y., et al., *Electrochemically cathodic exfoliation of graphene sheets in room temperature ionic liquids N-butyl, methylpyrrolidinium bis(trifluoromethylsulfonyl)imide and their electrochemical properties.* Electrochimica Acta, 2013. **113**: p. 9-16.
37. Wang, J., et al., *High-Yield Synthesis of Few-Layer Graphene Flakes through Electrochemical Expansion of Graphite in Propylene Carbonate Electrolyte.* Journal of the American Chemical Society, 2011. **133**(23): p. 8888-8891.
38. Cooper, A.J., et al., *On the controlled electrochemical preparation of R4N+ graphite intercalation compounds and their host structural deformation effects.* Journal of Electroanalytical Chemistry, 2014. **730**: p. 34-40.
39. Zhang, Y., L. Zhang, and C. Zhou, *Review of Chemical Vapor Deposition of Graphene and Related Applications.* Accounts of Chemical Research, 2013. **46**(10): p. 2329-2339.
40. Stankovich, S., et al., *Synthesis of graphene-based nanosheets via chemical reduction of exfoliated graphite oxide.* Carbon, 2007. **45**(7): p. 1558-1565.
41. Li, D., et al., *Processable aqueous dispersions of graphene nanosheets.* Nature Nanotechnology, 2008. **3**: p. 101.
42. Shin, H.-J., et al., *Efficient Reduction of Graphite Oxide by Sodium Borohydride and Its Effect on Electrical Conductance.* Advanced Functional Materials, 2009. **19**(12): p. 1987-1992.
43. Fernández-Merino, M.J., et al., *Vitamin C Is an Ideal Substitute for Hydrazine in the Reduction of Graphene Oxide Suspensions.* The Journal of Physical Chemistry C, 2010. **114**(14): p. 6426-6432.
44. Pei, S., et al., *Direct reduction of graphene oxide films into highly conductive and flexible graphene films by hydrohalic acids.* Carbon, 2010. **48**(15): p. 4466-4474.

45. Becerril, H.A., et al., *Evaluation of Solution-Processed Reduced Graphene Oxide Films as Transparent Conductors.* ACS Nano, 2008. **2**(3): p. 463-470.
46. Wang, X., L. Zhi, and K. Müllen, *Transparent, Conductive Graphene Electrodes for Dye-Sensitized Solar Cells.* Nano Letters, 2008. **8**(1): p. 323-327.
47. Zhu, Y., et al., *Microwave assisted exfoliation and reduction of graphite oxide for ultracapacitors.* Carbon, 2010. **48**(7): p. 2118-2122.
48. Cote, L.J., R. Cruz-Silva, and J. Huang, *Flash Reduction and Patterning of Graphite Oxide and Its Polymer Composite.* Journal of the American Chemical Society, 2009. **131**(31): p. 11027-11032.
49. Yang, D., et al., *Chemical analysis of graphene oxide films after heat and chemical treatments by X-ray photoelectron and Micro-Raman spectroscopy.* Carbon, 2009. **47**(1): p. 145-152.
50. Yu, Q., et al., *Graphene segregated on Ni surfaces and transferred to insulators.* Applied Physics Letters, 2008. **93**(11): p. 113103.
51. Reina, A., et al., *Large Area, Few-Layer Graphene Films on Arbitrary Substrates by Chemical Vapor Deposition.* Nano Letters, 2009. **9**(1): p. 30-35.
52. Arco, L.G.D., et al., *Synthesis, Transfer, and Devices of Single- and Few-Layer Graphene by Chemical Vapor Deposition.* IEEE Transactions on Nanotechnology, 2009. **8**(2): p. 135-138.
53. Kim, K.S., et al., *Large-scale pattern growth of graphene films for stretchable transparent electrodes.* Nature, 2009. **457**: p. 706.

53* Zhang, Y., Zhang, L., and Zhou, C., *Review of Chemical Vapor Deposition of Graphene and Related Applications. Acc. Chem. Res.* 2013. 46 (10) p. 2329-2339.

54. Liu, N., et al., *Universal Segregation Growth Approach to Wafer-Size Graphene from Non-Noble Metals.* Nano Letters, 2011. **11**(1): p. 297-303.
55. Li, X., et al., *Large-Area Synthesis of High-Quality and Uniform Graphene Films on Copper Foils.* Science, 2009. **324**(5932): p. 1312-1314.
56. Wu, W., et al., *Growth of single crystal graphene arrays by locally controlling nucleation on polycrystalline Cu using chemical vapor deposition.* Adv Mater, 2011. **23**(42): p. 4898-903.
57. Wang, H., et al., *Controllable Synthesis of Submillimeter Single-Crystal Monolayer Graphene Domains on Copper Foils by Suppressing Nucleation.* Journal of the American Chemical Society, 2012. **134**(8): p. 3627-3630.
58. Li, X., et al., *Large-Area Graphene Single Crystals Grown by Low-Pressure Chemical Vapor Deposition of Methane on Copper.* Journal of the American Chemical Society, 2011. **133**(9): p. 2816-2819.
59. Zhang, Y., et al., *Vapor Trapping Growth of Single-Crystalline Graphene Flowers: Synthesis, Morphology, and Electronic Properties.* Nano Letters, 2012. **12**(6): p. 2810-2816.
60. Guermoune, A., et al., *Chemical vapor deposition synthesis of graphene on copper with methanol, ethanol, and propanol precursors.* Carbon, 2011. **49**(13): p. 4204-4210.
61. Bo, Z., et al., *Plasma-enhanced chemical vapor deposition synthesis of vertically oriented graphene nanosheets.* Nanoscale, 2013. **5**(12): p. 5180-5204.
62. Wang, S.M., et al., *Synthesis of graphene on a polycrystalline Co film by radio-frequency plasma-enhanced chemical vapour deposition.* Journal of Physics D: Applied Physics, 2010. **43**(45): p. 455402.
63. Vitchev, R., et al., *Initial stages of few-layer graphene growth by microwave plasma-enhanced chemical vapour deposition.* Nanotechnology, 2010. **21**(9): p. 095602.
64. Kim, J., et al., *Low-temperature synthesis of large-area graphene-based transparent conductive films using surface wave plasma chemical vapor deposition.* Applied Physics Letters, 2011. **98**(9): p. 091502.

65. Wei, D., et al., *Low Temperature Critical Growth of High Quality Nitrogen Doped Graphene on Dielectrics by Plasma-Enhanced Chemical Vapor Deposition.* ACS Nano, 2015. **9**(1): p. 164-171.
66. Kim, Y., et al., *Low-temperature synthesis of graphene on nickel foil by microwave plasma chemical vapor deposition.* Appl Phys Lett, 2011. **98**(26): p. 263106-2631063.
67. Qi, J., et al., *Synthesis of graphene on a Ni film by radio-frequency plasma-enhanced chemical vapor deposition.* Chinese Science Bulletin, 2012. **57**(23): p. 3040-3044.
68. Othman, M., et al., *Low-temperature plasma-enhanced chemical vapour deposition of transfer-free graphene thin films.* Materials Letters, 2015. **158**: p. 436-438.
69. Emtsev, K.V., et al., *Interaction, growth, and ordering of epitaxial graphene on SiC{0001} surfaces: A comparative photoelectron spectroscopy study.* Physical Review B, 2008. **77**(15): p. 155303.
70. Gao, L., J.R. Guest, and N.P. Guisinger, *Epitaxial Graphene on Cu(111).* Nano Letters, 2010. **10**(9): p. 3512-3516.
71. Biedermann, L.B., et al., *Insights into few-layer epitaxial graphene growth on $4H\text{-SiC}(000\overline{1})$ substrates from STM studies.* Physical Review B, 2009. **79**(12): p. 125411.
72. Huang, H., et al., *Bottom-up Growth of Epitaxial Graphene on 6H-SiC(0001).* ACS Nano, 2008. **2**(12): p. 2513-2518.
73. Alpha, T.N.D., et al., *Structure of epitaxial graphene on Ir(111).* New Journal of Physics, 2008. **10**(4): p. 043033.
74. Shivaraman, S., et al., *Free-Standing Epitaxial Graphene.* Nano Letters, 2009. **9**(9): p. 3100-3105.
75. Chen, M., et al., *Layer-dependent fluorination and doping of graphene via plasma treatment.* Nanotechnology, 2012. **23**(11): p. 115706.
76. McAllister, M.J., et al., *Single Sheet Functionalized Graphene by Oxidation and Thermal Expansion of Graphite.* Chemistry of Materials, 2007. **19**(18): p. 4396-4404.
77. Tran, D.N.H., S. Kabiri, and D. Losic, *A green approach for the reduction of graphene oxide nanosheets using non-aromatic amino acids.* Carbon, 2014. **76**: p. 193-202.
78. Chua, C.K. and M. Pumera, *The reduction of graphene oxide with hydrazine: elucidating its reductive capability based on a reaction-model approach.* Chemical Communications, 2016. **52**(1): p. 72-75.
79. Some, S., et al., *High-quality reduced graphene oxide by a dual-function chemical reduction and healing process.* Sci Rep, 2013. **3**: p. 1929.
80. Pendolino, F. and N. Armata, *Synthesis, Characterization and Models of Graphene Oxide.* 2017: p. 5-21.
81. Brodie, B.C., *On the Atomic Weight of Graphite.* Royal Society. **Vol. 149 (1859)**: p. 249-259.
82. Hummers, W.S. and R.E. Offeman, *Preparation of Graphitic Oxide.* Journal of the American Chemical Society, 1958. **80**(6): p. 1339-1339.
83. Marcano, D.C., et al., *Improved Synthesis of Graphene Oxide.* ACS Nano, 2010. **4**(8): p. 4806-4814.
84. Bacon, M., S.J. Bradley, and T. Nann, *Graphene Quantum Dots.* Particle & Particle Systems Characterization, 2014. **31**(4): p. 415-428.
85. Li, L.L., et al., *A Facile Microwave Avenue to Electrochemiluminescent Two-Color Graphene Quantum Dots.* Advanced Functional Materials, 2012. **22**(14): p. 2971-2979.
86. Xie, R.B., et al., *Graphene quantum dots as smart probes for biosensing.* Analytical Methods, 2016. **8**(20): p. 4001-4016.
87. Chen, S., et al., *Unusual emission transformation of graphene quantum dots induced by self-assembled aggregation.* Chemical Communications, 2012. **48**(61): p. 7637-7639.
88. Pan, D., et al., *Hydrothermal route for cutting graphene sheets into blue-luminescent graphene quantum dots.* Adv Mater, 2010. **22**(6): p. 734-8.

89. Qin, H., et al., *Near-UV-emitting graphene quantum dots from graphene hydrogels.* Carbon, 2015. **94**: p. 181-188.
90. Zhu, S., et al., *Strongly green-photoluminescent graphene quantum dots for bioimaging applications.* Chemical Communications, 2011. **47**(24): p. 6858-6860.
91. Liu, Q., et al., *Strong Two-Photon-Induced Fluorescence from Photostable, Biocompatible Nitrogen-Doped Graphene Quantum Dots for Cellular and Deep-Tissue Imaging.* Nano Letters, 2013. **13**(6): p. 2436-2441.
92. Zhang, M., et al., *Facile synthesis of water-soluble, highly fluorescent graphene quantum dots as a robust biological label for stem cells.* Journal of Materials Chemistry, 2012. **22**(15): p. 7461-7467.
93. Zhang, M., et al., *Facile synthesis of water-soluble, highly fluorescent graphene quantum dots as a robust biological label for stem cells.* Journal of materials chemistry, 2012. **22**(15): p. 7461-7467.
94. Shih, Y.-W., et al., *Graphene quantum dots derived from platelet graphite nanofibers by liquid-phase exfoliation.* Acta Materialia, 2014. **78**: p. 314-319.
95. Liu, F., et al., *Facile synthetic method for pristine graphene quantum dots and graphene oxide quantum dots: origin of blue and green luminescence.* Adv Mater, 2013. **25**(27): p. 3657-62.
96. Zhuo, S., M. Shao, and S.-T. Lee, *Upconversion and downconversion fluorescent graphene quantum dots: ultrasonic preparation and photocatalysis.* ACS nano, 2012. **6**(2): p. 1059-1064.
97. Lu, J., et al., *Transforming C60 molecules into graphene quantum dots.* Nature Nanotechnology, 2011. **6**: p. 247.
98. Wang, L., et al., *Gram-scale synthesis of single-crystalline graphene quantum dots with superior optical properties.* Nature Communications, 2014. **5**: p. 5357.
99. Qu, D., et al., *Highly luminescent S, N co-doped graphene quantum dots with broad visible absorption bands for visible light photocatalysts.* Nanoscale, 2013. **5**(24): p. 12272-12277.
100. Dong, Y., et al., *Blue luminescent graphene quantum dots and graphene oxide prepared by tuning the carbonization degree of citric acid.* Carbon, 2012. **50**(12): p. 4738-4743.
101. Wu, X., et al., *Fabrication of highly fluorescent graphene quantum dots using l-glutamic acid for in vitro/in vivo imaging and sensing.* Journal of Materials Chemistry C, 2013. **1**(31): p. 4676-4684.
102. Ferrari, A.C., et al., *Science and technology roadmap for graphene, related two-dimensional crystals, and hybrid systems.* Nanoscale, 2015. **7**(11): p. 4598-4810.
103. Zhao, Y., et al., *Metal organic frameworks for energy storage and conversion.* Energy Storage Materials, 2016. **2**: p. 35-62.
104. Silva, P. et al., *Multifunctional metal–organic frameworks: from academia to industrial applications*. Chem. Soc. Rev., 2015, 44, 6774-6803.
105. Shoaee, M., M.W. Anderson, and M.P. Attfield, *Crystal growth of the nanoporous metal-organic framework HKUST-1 revealed by in situ atomic force microscopy.* Angew Chem Int Ed Engl, 2008. **47**(44): p. 8525-8.
106. Wong-Foy, A.G., A.J. Matzger, and O.M. Yaghi, *Exceptional H2 Saturation Uptake in Microporous Metal−Organic Frameworks.* Journal of the American Chemical Society, 2006. **128**(11): p. 3494-3495.
107. Prestipino, C., et al., *Local Structure of Framework Cu(II) in HKUST-1 Metallorganic Framework: Spectroscopic Characterization upon Activation and Interaction with Adsorbates.* Chemistry of Materials, 2006. **18**(5): p. 1337-1346.
108. Burtch, N.C., H. Jasuja, and K.S. Walton, *Water Stability and Adsorption in Metal–Organic Frameworks.* Chemical Reviews, 2014. **114**(20): p. 10575-10612.
109. Lee, Y.-R., et al., *ZIF-8: A comparison of synthesis methods.* Chemical Engineering Journal, 2015. **271**: p. 276-280.

110. Kandiah, M., et al., *Synthesis and Stability of Tagged UiO-66 Zr-MOFs.* Chemistry of Materials, 2010. **22**(24): p. 6632-6640.
111. Lin, Q., et al., *New Heterometallic Zirconium Metalloporphyrin Frameworks and Their Heteroatom-Activated High-Surface-Area Carbon Derivatives.* Journal of the American Chemical Society, 2015. **137**(6): p. 2235-2238.
112. Dey, C., et al., *Crystalline metal-organic frameworks (MOFs): synthesis, structure and function.* Acta Crystallogr B Struct Sci Cryst Eng Mater, 2014. **70**(Pt 1): p. 3-10.
113. Gangu, K.K., et al., *A review on contemporary Metal–Organic Framework materials.* Inorganica Chimica Acta, 2016. **446**: p. 61-74.
114. Liu, K., et al., *Facile and rapid fabrication of metal–organic framework nanobelts and color-tunable photoluminescence properties.* Journal of Materials Chemistry, 2010. **20**(16): p. 3272-3279.
115. Morris, R.E. and P.S. Wheatley, *Gas storage in nanoporous materials.* Angew Chem Int Ed Engl, 2008. **47**(27): p. 4966-81.
116. Blundell, S.J. and F.L. Pratt, *Organic and molecular magnets.* Journal of Physics: Condensed Matter, 2004. **16**(24): p. R771-R828.
117. Lee, J., et al., *Metal-organic framework materials as catalysts.* Chem Soc Rev, 2009. **38**(5): p. 1450-9.
118. Langer, R., *Drug delivery and targeting.* Nature, 1998. **392**(6679 SUPPL.): p. 5-10.
119. Salonen, J., et al., *Mesoporous Silicon in Drug Delivery Applications.* Journal of Pharmaceutical Sciences, 2008. **97**(2): p. 632-653.
120. Wang, H., et al., *Metal-Organic Frameworks for Energy Applications.* Chem, 2017. **2**(1): p. 52-80.
121. Maiti, S., et al., *Cu 3 (1,3,5-benzenetricarboxylate) 2 metal-organic framework: A promising anode material for lithium-ion battery.* Microporous and Mesoporous Materials, 2016. **226**: p. 353-359.
122. Kim, A.Y., et al., *One-Step Catalytic Synthesis of CuO/Cu2O in a Graphitized Porous C Matrix Derived from the Cu-Based Metal-Organic Framework for Li- and Na-Ion Batteries.* ACS Appl Mater Interfaces, 2016. **8**(30): p. 19514-23.
123. Ji, D., et al., *Facile fabrication of MOF-derived octahedral CuO wrapped 3D graphene network as binder-free anode for high performance lithium-ion batteries.* Chemical Engineering Journal, 2017. **313**: p. 1623-1632.
124. Yan, X., et al., *Porous carbons prepared by direct carbonization of MOFs for supercapacitors.* Applied Surface Science, 2014. **308**: p. 306-310.
125. Wang, L., et al., *Metal–organic frameworks for energy storage: Batteries and supercapacitors.* Coordination Chemistry Reviews, 2016. **307**: p. 361-381.
126. Khan, I.A., et al., *A copper based metal-organic framework as single source for the synthesis of electrode materials for high-performance supercapacitors and glucose sensing applications.* International Journal of Hydrogen Energy, 2014. **39**(34): p. 19609-19620.
127. Ke, F.-S., Y.-S. Wu, and H. Deng, *Metal-organic frameworks for lithium ion batteries and supercapacitors.* Journal of Solid State Chemistry, 2015. **223**: p. 109-121.
128. Mohan, V.B., et al., *Graphene-based materials and their composites: A review on production, applications and product limitations.* Composites Part B: Engineering, 2018. **142**: p. 200-220.
129. Kumar, R., et al., *Growth of 2D sheets of a MOF on graphene surfaces to yield composites with novel gas adsorption characteristics.* Dalton Transactions, 2014. **43**(20): p. 7383-7386.
130. Szczęśniak, B., J. Choma, and M. Jaroniec, *Gas adsorption properties of hybrid graphene-MOF materials.* Journal of Colloid and Interface Science, 2018. **514**: p. 801-813.

131. Kaur, R., K.-H. Kim, and A. Deep, *A convenient electrolytic assembly of graphene-MOF composite thin film and its photoanodic application.* Applied Surface Science, 2017. **396**: p. 1303-1309.
132. Zhu, G., et al., *Microwave assisted synthesis of reduced graphene oxide incorporated MOF-derived ZnO composites for photocatalytic application.* Catalysis Communications, 2017. **88**: p. 5-8.
133. Wang, Y., et al., *Supercapacitor Devices Based on Graphene Materials.* The Journal of Physical Chemistry C, 2009. **113**(30): p. 13103-13107.
134. Huang, X., et al., *Graphene-based materials: synthesis, characterization, properties, and applications.* Small, 2011. **7**(14): p. 1876-902.
135. Zhang, X., Zhang, H., Li, C., Wang, K., Sun, X. & Ma, Y, *Recent advances in porous graphene materials for supercapacitor applications.* RSC Advances, 2014: p. 45862-45884.
136. Srimuk, P., et al., *Solid-type supercapacitor of reduced graphene oxide-metal organic framework composite coated on carbon fiber paper.* Electrochimica Acta, 2015. **157**: p. 69-77.
137. Banerjee, P.C., et al., *Electrochemical Capacitance of Ni-Doped Metal Organic Framework and Reduced Graphene Oxide Composites: More than the Sum of Its Parts.* ACS Applied Materials & Interfaces, 2015. **7**(6): p. 3655-3664.
138. Cao, X., et al., *Reduced graphene oxide-wrapped MoO3 composites prepared by using metal-organic frameworks as precursor for all-solid-state flexible supercapacitors.* Adv Mater, 2015. **27**(32): p. 4695-701.
139. Zhou, Y., et al., *In-Situ Fabrication of Graphene Oxide Hybrid Ni-Based Metal–Organic Framework (Ni–MOFs@GO) with Ultrahigh Capacitance as Electrochemical Pseudocapacitor Materials.* ACS Applied Materials & Interfaces, 2016. **8**(42): p. 28904-28916.
140. Wang, Z., et al., *Electrochemical performance and transformation of Co-MOF/reduced graphene oxide composite.* Materials Letters, 2017. **193**: p. 216-219.
141. Xu, X., et al., *Facile Fabrication of Three-Dimensional Graphene and Metal–Organic Framework Composites and Their Derivatives for Flexible All-Solid-State Supercapacitors.* Chemistry of Materials, 2017. **29**(14): p. 6058-6065.
142. Yu, D., et al., *A general route to the synthesis of layer-by-layer structured metal organic framework/graphene oxide hybrid films for high-performance supercapacitor electrodes.* Journal of Materials Chemistry A, 2017. **5**(32): p. 16865-16872.
143. Justino, C.I.L., et al., *Graphene based sensors and biosensors.* TrAC Trends in Analytical Chemistry, 2017. **91**: p. 53-66.
144. Chidambaram, A. and K.C. Stylianou, *Electronic metal–organic framework sensors.* Inorganic Chemistry Frontiers, 2018. **5**(5): p. 979-998.
145. Kreno, L.E., et al., *Metal-organic framework materials as chemical sensors.* Chem Rev, 2012. **112**(2): p. 1105-25.
146. Wang, L., et al., *Cu-Hemin Metal-Organic-Frameworks/Chitosan-Reduced Graphene Oxide Nanocomposites with Peroxidase-Like Bioactivity for Electrochemical Sensing.* Electrochimica Acta, 2016. **213**: p. 691-697.
147. Yang, J., et al., *Metal–organic framework derived hollow polyhedron CuCo 2 O 4 functionalized porous graphene for sensitive glucose sensing.* Sensors and Actuators B: Chemical, 2017. **242**: p. 728-735.
148. Luo, S. and J. Wang, *MOF/graphene oxide composite as an efficient adsorbent for the removal of organic dyes from aqueous solution.* Environmental Science and Pollution Research, 2018. **25**(6): p. 5521-5528.
149. Petit, C., B. Mendoza, and T.J. Bandosz, *Hydrogen sulfide adsorption on MOFs and MOF/graphite oxide composites.* Chemphyschem, 2010. **11**(17): p. 3678-84.

150. Yan, J.-M., et al., *AuPd-MnOx/MOF-Graphene: An Efficient Catalyst for Hydrogen Production from Formic Acid at Room Temperature.* Advanced Energy Materials, 2015. **5**(10): p. 1500107.
151. Aguilera-Sigalat, J. and D. Bradshaw, *Synthesis and applications of metal-organic framework–quantum dot (QD@MOF) composites.* Coordination Chemistry Reviews, 2016. **307**: p. 267-291.
152. Ameloot, R., et al., *Metal-organic framework single crystals as photoactive matrices for the generation of metallic microstructures.* Adv Mater, 2011. **23**(15): p. 1788-91.
153. Müller, M., et al., *Loading of MOF-5 with Cu and ZnO Nanoparticles by Gas-Phase Infiltration with Organometallic Precursors: Properties of Cu/ZnO@MOF-5 as Catalyst for Methanol Synthesis.* Chemistry of Materials, 2008. **20**(14): p. 4576-4587.
154. Zhao, D., et al., *Metal–organic frameworks (MOFs) combined with ZnO quantum dots as a fluorescent sensing platform for phosphate.* Sensors and Actuators B: Chemical, 2014. **197**: p. 50-57.
155. Wee, L.H., et al., *Local transformation of ZIF-8 powders and coatings into ZnO nanorods for photocatalytic application.* Nanoscale, 2014. **6**(4): p. 2056-2060.
156. Zhan, W.-w., et al., *Semiconductor@Metal–Organic Framework Core–Shell Heterostructures: A Case of ZnO@ZIF-8 Nanorods with Selective Photoelectrochemical Response.* Journal of the American Chemical Society, 2013. **135**(5): p. 1926-1933.
157. Gao, Y., et al., *The electrochemical performance of SnO2 quantum dots@zeolitic imidazolate frameworks-8 (ZIF-8) composite material for supercapacitors.* Materials Letters, 2014. **128**: p. 208-211.
158. Li, R., et al., *Integration of an inorganic semiconductor with a metal-organic framework: a platform for enhanced gaseous photocatalytic reactions.* Adv Mater, 2014. **26**(28): p. 4783-8.
159. Buso, D., et al., *Highly luminescent metal-organic frameworks through quantum dot doping.* Small, 2012. **8**(1): p. 80-8.
160. Kaur, R., A.K. Paul, and A. Deep, *Nanocomposite of europium organic framework and quantum dots for highly sensitive chemosensing of trinitrotoluene.* Forensic Science International, 2014. **242**: p. 88-93.
161. Lu, G., et al., *Imparting functionality to a metal–organic framework material by controlled nanoparticle encapsulation.* Nature Chemistry, 2012. **4**: p. 310.
162. He, J., et al., *Significantly enhanced photocatalytic hydrogen evolution under visible light over CdS embedded on metal–organic frameworks.* Chemical Communications, 2013. **49**(60): p. 6761-6763.
163. Lin, R., et al., *Enhanced photocatalytic hydrogen production activity via dual modification of MOF and reduced graphene oxide on CdS.* Chemical Communications, 2014. **50**(62): p. 8533-8535.
164. Shen, L., et al., *CdS-decorated UiO–66(NH2) nanocomposites fabricated by a facile photodeposition process: an efficient and stable visible-light-driven photocatalyst for selective oxidation of alcohols.* Journal of Materials Chemistry A, 2013. **1**(37): p. 11473-11482.
165. Jin, S., et al., *Energy Transfer from Quantum Dots to Metal–Organic Frameworks for Enhanced Light Harvesting.* Journal of the American Chemical Society, 2013. **135**(3): p. 955-958.
166. Lin, Q.-j., et al., *Multifractal analysis for Cu/Ti bilayer thin films.* Surface and Interface Analysis, 2013. **45**(8): p. 1223-1227.
167. He, L., et al., *Carbon nanodots@zeolitic imidazolate framework-8 nanoparticles for simultaneous pH-responsive drug delivery and fluorescence imaging.* CrystEngComm, 2014. **16**(16): p. 3259-3263.
168. Zhang, L., et al., *Water-dispersed quantum dots of coordination polymers with strong photoluminescence.* Chemical Communications, 2012. **48**(49): p. 6166-6168.

Chapter 2. Methodology

This chapter presents the preparation and characterisation techniques of materials (pG, GO, GQDs, and HKUST-1 MOF) that are used in the whole thesis.

2.1 Chemicals and raw materials

Natural graphite rocks (Uley, Eyre Peninsula, SA) were obtained and milled into a fine powder using a benchtop ring mill (Rock labs). Potassium permanganate ($KMnO_4$, Sigma–Aldrich), 98% sulfuric acid (H_2SO_4, Sigma–Aldrich), 85% phosphoric acid (H_3PO_4, Chem-Supply), 30% hydrogen peroxide (H_2O_2, Chem-Supply), 35% hydrochloric acid (HCl, Merck), and ethanol (Chem-Supply), Copper nitrate trihydrate ($Cu(NO_3)_2$, Sigma–Aldrich), 1,3,5-benzenetricarboxylic acid (Sigma–Aldrich) were used directly without further purification. Exfoliated graphite (EG) was synthesised at Graphene lab at The University of Adelaide. All aqueous solutions were prepared with Milli-Q water (Purelab Option-Q) with a surface tension of 72.8 mN/m at 20^{o}C, a specific resistivity of 18.2 MΩ·cm at 25^{o}C and a pH of 5.6, unless otherwise stated.

2.2 Material preparation

2.2.1 Preparation of GO

GO was prepared by the modified Hummer's method, as reported previously [1]. Briefly, in the first step, the graphite powders (3.0 g) were mixed with $KMnO_4$ (18.0 g) in an Erlenmeyer flask, and a mixture of H_2SO_4 and H_3PO_4 acids (360:40 ml) was then transferred to another flask. Both mixtures were cooled for 4 h at 4 ℃. The two mixtures were subsequently combined slowly, and the mixture was heated to 55℃ in an oil bath and magnetically stirred continuously for 12 h. When the reaction was completed, the solution poured onto ice and H_2O_2 30% (3 mL) was added to halt the reaction. Subsequently, the solution was washed with hydrochloric acid (HCl 32%) (200 mL) twice and then with distilled water several times until the pH value reached 7.

2.2.2 Preparation of pristine graphene (pG)

The pG was prepared by solvent exfoliation methods, as reported in [2,3]. Firstly, 200 mL of 0.5 mg/mL GO suspension was obtained by dispersing GO (100 mg) in 200 mL of Milli-Q water. Subsequently, expanded graphite (EG) powder (300 mg) was ground with NaCl salt (1500 mg) for 20 min in an agate mortar to achieve a homogenous mixture. The NaCl crystallites were then removed by washing with water under vacuum filtration several times. The resulting EG sheets were then mixed with water (300mL) in a 500 mL round-bottom flask before the mixture was sonicated in a bath sonicator for 1

h. The mixture was then mixed with 200 mL of GO suspension and sonicated by UIP1000hd (Hielscher) 22 mm-diameter sonotrode at the power of 150 W and the amplitude of 80%, in which the temperature of the mixture was maintained at less than 40ºC. After that, the mixture was left for 24 h for large graphite particles to deposit, and the supernatant was extracted by centrifuging the mixture at 4200 rpm for 1 h. The graphene, which was precipitated in GO, was decanted and washed a few times with water and then dried in a vacuum oven overnight.

2.2.3 Preparation of GQDs

GQDs was synthesised by the shearing cutting method, as reported in [4]. 100 mL of well-dispersed GO solution (~6.0 mg/mL) was added 500 ml miliQ water to form a 1 mg/mL GO suspension. Subsequently, the solution was sonicated by using UIP1000hd (Hielscher) 22 mm-diameter sonotrode at the power of 200 W and the amplitude of 80%, for 5 h, 10 h and 15 h, in which the temperature of the solution was kept at less than 40ºC. After each 5 h, 50 ml of solution was taken out for other characterisations until the sonicating time reached 15 h. In the next step, the solution was cooled down to the ambient temperature. After that, the sonicating solution was centrifuged at 4,000 rpm for 2 h and then 10,000 rpm for 2 h to remove the large particles. To obtain the fine GQDs, the centrifuged solution was filtered by using syringe filters with the pore size of 400 nm, 200 nm and 100 nm, 10 times each, respectively.

2.2.4 Preparation of HKUST-1 MOF

The mass ratio of starting materials and the kind of solvent play a vital role in synthesising HKUST-1 MOF and other MOFs (chapter 5) to obtain their expected structures. In this experiment, copper nitrate trihydrate (1.75 g) and 1,3,5-benzenetricarboxylic acid (0.84 g) and 50 mL of ethanol were mixed in a 100 mL round-bottom flask. The mixture was then heated up at reflux overnight. In the next step, the magnetic stirring of the solution was ceased, and the solution was slowly cooled to the room temperature. Finally, the precipitate formed was filtered off, and wash with water (2 x 20 mL) followed by ethanol (2 x 20 mL).

2.3 Material characterisation techniques

Characterisation of materials plays an essential role in materials sciences and other scientific fields since it supports to determine the elements, chemical bonds, structures of materials, and the typical properties of any materials. The instruments consist of various advanced characterising techniques. Scanning electron microscopy (SEM) and Transmission electron microscopy (TEM) are the most widely used equipment to characterise the morphology of materials, and the nanostructure of materials, respectively. Chemical and physical properties of the synthesised nanomaterials are systematically characterised by various analytical techniques such as X-ray diffractometer (XRD), Fourier transformation infrared (FTIR), Raman spectroscopy, Thermal gravimetric analyser (TGA), UV-Visible instrument (UV-Vis), Photoluminescence (PL), etc. In this chapter, the preparation approaches of graphene derivatives, as well as MOFs, are briefly described. Subsequently, the fundamentals of methods for characterisations of prepared materials are introduced.

2.3.1 SEM and EDAX

SEM is one of the most widely used techniques employed in morphology characterisation of nanomaterials and nanostructures. SEM can provide magnifications in the range from ~10 X to over 300,000 X. It also provides chemical composition information near the surface of the samples. In a typical SEM, a source of electrons is focused into a beam that is projected over the surface of the specimen by deflection coils. When the electrons are directed onto the surface of a sample, they interact with atoms of top surface material, and some of which have become the secondary electrons and they are detected by detectors. The detectors are connected with a computer program to convert the signals into the images of samples surface. EDAX is usually combined with SEM; therefore, SEM not only provides the image of the morphology of nanostructured materials but also provide detailed information on chemical composition and elemental spectra. The preparation of samples for SEM measurement is also vital to obtain the satisfactory quality of SEM images. For non-conductive materials, they are required to coat a thin layer on top of samples by highly conductive materials such as gold, platinum or even carbon using coaters. The purpose of the coating layer is to inhibit electric charging interaction between the electron beam and sample surface,

reduces the damage and improve the second electron signal. Therefore, high-quality SEM images can be achieved. The SEM Quanta 450, (Adelaide Microscopy, The University of Adelaide) (Figure 2.1) is used to analyse microstructural characteristics of the HKUST-1, GO/HKUST-1, and L-rGO, and L-rGO-C-MOF composites, pG-MOF nanocomposites. The SEM samples were prepared by putting the samples on the carbon tape stuck on SEM stubs. Before capturing, the samples were coated platinum with the thickness of the coating layer of around 10 nm. The EDAX is used to determine the presence of elements in GO/HKUST-1, and L-rGO-C-MOF composites.

Figure 2.1. SEM Quanta 450.

2.3.2 TEM

TEM is one of the most powerful and versatile techniques for the characterisation of nanostructured systems. It has unique characteristics that allow us to achieve atomic resolution of crystal lattices at the sub-nanometer scale.

The interaction of an electron beam with a solid specimen results in several elastic or inelastic scattering phenomena (backscattering or reflection, emission of secondary electrons, X rays or optical photons, and transmission of the no deviated beam along with beam deviated as a consequence of elastic – single atom scattering, diffraction – or inelastic phenomena) [5, 6]. The TEM technique is dedicated to the analysis of the transmitted or forward-scattered beam. Such a beam is passed through a series of lenses, among which the objective lens mainly determines the image resolution, to obtain the magnified image. The photo of Tecnai G2 TEM is shown in Figure 2.2.

Figure 2.2 TEM Tecnai, G2, 120 kV.

In this thesis, the Tecnai G2 TEM is used to analyse the nanostructure characteristics of the GO/HKUST-1 nanocomposite. The Titan Themis TEM is employed to measure the crystallinity of pG-MOF nanocomposites. The TEM samples were all prepared by sonicating for 1 h before dropping two droplets on copper grids and dried for TEM capturing. (Adelaide Microscopy, The University of Adelaide).

2.3.3 XRD

XRD is one of the powerful tools to characterise the crystalline of materials. The spectrum of XRD can be scanned in a wide range of 2θ angles ranging from 3º to 80º, with adjustable scan speed, but the normal speed is 10º/min. The typical XRD machine operates at the column voltage of 40 kV and 15 mA (Cu $K\alpha$ radiation, λ = 1.5406 Å). The sample preparation for XRD is the most crucial step to obtain the desired results. Since the sample surface receives the incident X-rays, it must be flat and positioned at the rotation centre of the goniometer. The diffracted X-rays shifts towards a lower angle side if the sample surface is concave. In contrast, a convex sample surface can result in a shift of the diffracted X-rays towards to higher angle side. The samples are in the forms of thin films or fine powders.

Figure 2.3 Rigaku MiniFlex 600 X-Ray Diffractometer.

The Rigaku MiniFlex 600 X-Ray Diffractometer (Figure 2.3) used in this chapter to characterise HKUST-1 diamonds, HKUTS-1 microrods, L-rGO and L-rGO/C-MOF composite, pG-MOF nanocomposites.

2.3.4 TGA

TGA is a scientific instrument to investigate the changes in the mass of materials with temperature. A TGA consists of three main components: a microgram balance, an

autosampler, and a thermocouple. In a typical TGA instrument, the temperature ranges from the ambient temperature to ~1000ºC, depending on the thermocouple type. The gas system in TGA can be air or nitrogen or both of them. The operation principle of TGA is simple. When the temperature increases, the mass of samples also changes due to either evaporation of H_2O or decomposition of materials, or even chemical reactions, leading to the decrease or the increase in the sample mass. For a typical material, its mass decreases with the increasing temperature. The samples were placed on the platinum pans when heating in a furnace under a flow of the air or nitrogen or both. TGA Q500, TA instrument was used in the thesis, as shown in Figure 2.4. The TGA is used to measure the weight loss with respect to the temperature for L-rGO and L-rGO-C-MOF composites, HKUST-1 microrods, GO, GO/HKUST-1.

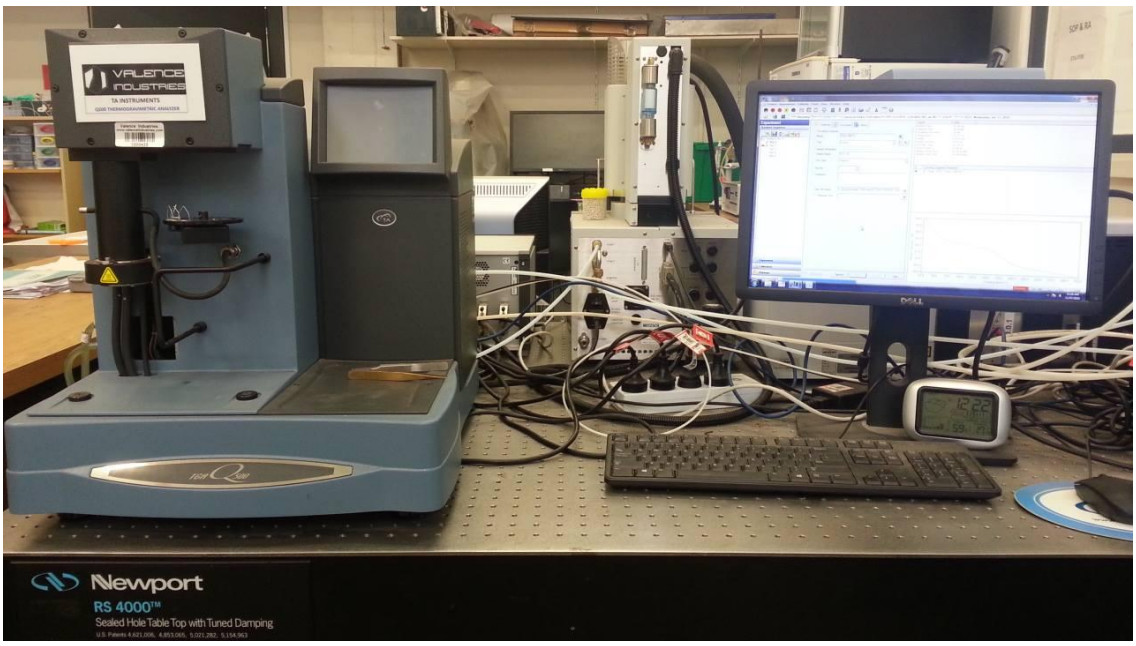

Figure 2.4 TGA Q500, TA instrument.

2.3.5 Raman spectroscopy

Raman spectroscopy is the most common tool to analyse the chemical structure of carbon-based materials including carbon black, carbon nanotubes, graphene and their derivatives [7-10]. Raman spectra provide much information on the material structures, for example, the defect level or disorder of chemical structures, the number layer of thin film, etc. In the thesis, Raman spectra were recorded from 500 to 3500 cm^{-1} on Raman spectroscopy (LabRAM HR Evolution, HORIBA JOBIN YVON, Japan) with a 532 nm

laser (Figure 2.5). Samples, which are L-rGO, L-rGO-C-MOF composites, and G-MOF nanocomposites, were placed on the 2 x 4 cm glass slides before they were then placed in the sample chamber for measuring.

Figure 2.5 HORIBA JOBIN YVON Raman spectroscopy.

2.3.6 UV-Vis spectroscopy

Figure 2.6 Cary 60 UV-Vis spectrometer.

UV-Vis is a commonly used tool in analytical chemistry, in which the absorption spectroscopy or reflectance spectroscopy occurs in the ultraviolet-visible spectral region [11], and the wavelength range is from 200 to 800 nm. HKUST-1@GQDs, HKUST-1 microrods, GQDs, and GO were characterised using the Cary 60 UV-Vis spectrometer (Figure 2.6). UV-Vis samples were prepared by sonicating GQDs and shaking (HKUST-1@ GQDs nanocomposites, and HKUST-1 microrods in water) with different concentrations of 0.5, 0.25, 0.1 mg/mL.

2.3.7 FTIR

FTIR is a useful technique for material analysis in the laboratory, recently for determining the functional groups in the chemical structure of materials. FTIR instrument using the Fourier transformation performed by a computer provides the desired spectral information. In a typical FTIR instrument, the background spectrum must be measured without samples.

Figure 2.7 Nicolet 6700 Thermo Fisher.

The spectrum of FTIR can be presented in transmittance or absorbance with respect to wavenumber (cm-1). The transmittance or absorbance peaks provides the information on the functional groups in the materials, according to their vibrational frequencies. FTIR spectrometer (Nicolet 6700 Thermo Fisher) (Figure 2.7) was applied for inspecting the functional groups in the chemical structures of the GO, QGDs, L-rGO

and L-rGO-C-MOF, GO and GO/HKUST-1 composite. The wavenumber range is from 400 to 4000 cm-1, and the samples are powders and thin films.

Conclusion

The chapter has provided the preparation of pG, GO, GQDs, and HKUST-1, followed by general characterisation techniques. These materials have been successfully synthesised, and they are employed as the starting materials for other experiments in the three following chapters. Besides, all characterisation methods are also theoretically introduced and practically applied for materials. The specific characterisation techniques, such as electrochemical measurement, PL measurement, and Nano sight measurement, are presented explicitly in the corresponding chapters.

References

1. Tran, D.N.H., S. Kabiri, and D. Losic, *A green approach for the reduction of graphene oxide nanosheets using non-aromatic amino acids.* Carbon, 2014. **76**: p. 193-202.
2. Tung, T.T., et al., *Scalable realization of conductive graphene films for high-efficiency microwave antennas.* Journal of Materials Chemistry C, 2016. **4**(45): p. 10620-10624.
3. Tung, T.T., et al., *Graphene Oxide-Assisted Liquid Phase Exfoliation of Graphite into Graphene for Highly Conductive Film and Electromechanical Sensors.* ACS Applied Materials & Interfaces, 2016. **8**(25): p. 16521-16532.
4. Zhuo, S., M. Shao, and S.-T. Lee, *Upconversion and downconversion fluorescent graphene quantum dots: ultrasonic preparation and photocatalysis.* ACS nano, 2012. **6**(2): p. 1059-1064.
5. Williams, D.B. and C.B. Carter, *Diffraction from Crystals*, in *Transmission Electron Microscopy: A Textbook for Materials Science*. 2009, Springer US: Boston, MA. p. 257-269.
6. Williams, D.B. and C.B. Carter, *High Energy-Loss Spectra and Images*, in *Transmission Electron Microscopy: A Textbook for Materials Science*. 2009, Springer US: Boston, MA. p. 715-739.
7. Dresselhaus, M.S., et al., *Raman spectroscopy of carbon nanotubes.* Physics Reports, 2005. **409**(2): p. 47-99.
8. Ferrari, A.C., *Raman spectroscopy of graphene and graphite: Disorder, electron–phonon coupling, doping and nonadiabatic effects.* Solid State Communications, 2007. **143**(1): p. 47-57.
9. Gruber, T., T.W. Zerda, and M. Gerspacher, *Raman studies of heat-treated carbon blacks.* Carbon, 1994. **32**(7): p. 1377-1382.
10. Malard, L.M., et al., *Raman spectroscopy in graphene.* Physics Reports, 2009. **473**(5): p. 51-87.
11. Mitochondrial Function, Gregory P. Holmes-Hampton, ... Tracey A. Rouault, in Methods in Enzymology, 2014. <https://www.sciencedirect.com/topics/chemistry/uv-vis-spectroscopy >.

Chapter 3. Hybridisation of MOFs and graphene: a new strategy for synthesis of highly porous 3D structures for high performing supercapacitors

This chapter reports a novel porous 3D-structured nanohybrid material with a unique architecture by combining graphene and metal-organic framework (MOF) (HKUST-1) microrods for high performing supercapacitors has been synthesised and characterised. The HKUST-1 microrods were prepared by a new method, converting their diamond-like shape into microrods via mechanical shear mixing in an aqueous solution. Grinding of HKUST-1 and graphene oxide (GO) resulted in the formation of a 3D GO-MOF composite with intercalated HKUST-1 microrods between GO sheets. The composite film was treated by a laser scribing method and created a highly porous, high surface area (> 600 m^2/g), and the conductive 3D nanostructured composite film (L-rGO-C-MOF) was used as electrodes for supercapacitor applications. The prepared film showed a high capacitance of 390 F/g at 5 mV/s and cyclic stability of 97.8 % at 10 A/g after 5000 cycles. The symmetrical supercapacitor delivered an excellent power density of 8037.5 W/kg with an outstanding energy density of 22.3 Wh/kg confirming a new pathway to design new 3D porous graphene-MOF composites for high-performance energy storage devices.

Journal paper is submitted:

Hybridization of MOFs and graphene: a new strategy for synthesis of porous 3D carbon composites for high performing supercapacitors.

Truc Van Ngo[1,2], Mahmoud Moussa[1,2], Tran Thanh Tung[1,2], Campbell Coghlan[1,2], Dusan Losic[1,2]*.

[1]School of Chemical Engineering, The University of Adelaide

[2]ARC Research Hub for Graphene Enabled Industry Transformation

The University of Adelaide, Adelaide, 5005 North Terrace, South Australia, Australia. Corresponding author*

E-mail address: dusan.losic@adelaide.edu.au

Manuscript paper is submitted for publication in Chemical Engineering Journal, 2019 (Elsevier).

Statement of Authorship

Title of Paper	Hybridization of MOFs and graphene: a new strategy for synthesis of highly porous 3D structures for high performing supercapacitors
Publication Status	☐ Published ☐ Accepted for Publication ☑ Submitted for Publication ☐ Unpublished and Unsubmitted work written in manuscript style
Publication Details	Truc Van Ngo, Mahmoud Moussa, Tran Thanh Tung, Campbell Coghlan, Dusan Losic*. Hybridization of MOFs and graphene: a new strategy for synthesis of highly porous 3D structures for high performing supercapacitors. Chemical Engineering Journal, 00(2019), 00-00.

Principal Author

Name of Principal Author (Candidate)	Truc Van Ngo		
Contribution to the Paper	Design and run all the experiments, analysed and interpreted data, made the first draft of manuscript, and revised the manuscript.		
Overall percentage (%)	80%		
Certification:	This paper reports on original research I conducted during the period of my Higher Degree by Research candidature and is not subject to any obligations or contractual agreements with a third party that would constrain its inclusion in this thesis. I am the primary author of this paper.		
Signature		Date	6 April 2019

Co-Author Contributions

By signing the Statement of Authorship, each author certifies that:

i. the candidate's stated contribution to the publication is accurate (as detailed above);
ii. permission is granted for the candidate in include the publication in the thesis; and
iii. the sum of all co-author contributions is equal to 100% less the candidate's stated contribution.

Name of Co-Author	Mahmoud Moussa		
Contribution to the Paper	Analysed the electrochemical experiment data and edited the manuscript		
Signature		Date	1/04/2019

Name of Co-Author	Tran Thanh Tung		
Contribution to the Paper	Supervised the development of the work, edited the manuscript		
Signature		Date	28/03/2019

Name of Co-Author	Campbell Coghlan		
Contribution to the Paper	Provided the HKUST-1 MOF material for experiment and edited the manuscript.		
Signature		Date	27/3/2019

Name of Co-Author	Dusan Losic		
Contribution to the Paper	Supervised the development of the work, edited the manuscript and was the corresponding author.		
Signature		Date	26 March 2019

Please cut and paste additional co-author panels here as required.

3.1 Introduction

The development of flexible and lightweight electronic components and circuits has caused an increasing demand for more efficient energy storage devices. Due to their high power density, fast charge-discharge rates and long life stability, supercapacitors or ultra-capacitors are attractive as an alternative or complementary energy storage device for batteries [1-5]. Supercapacitors store energy in electrochemical double layers (EDLs), with the superior power density and charge/discharge lifetimes over batteries that operate through Faradaic processes and are designed to provide higher energy density [6].

Graphene, a monolayer of sp^2 hybridised carbon atoms, is considered as an outstanding and highly efficient material for supercapacitor electrodes owing to its remarkable properties including its high thermal and electrical conductivity, mechanical properties and high electron mobility [7-9]. However, graphene sheets usually restack through strong π-π interactions, which results in poorly interconnected channels, low electrolyte permeability, ion diffusion and slow redox reaction between the electrolyte and the active material [10, 11]. Therefore, various strategies have been trialled to develop non-stacking graphene nanocomposite materials. Current approaches typically fabricate either 3D hierarchical porous graphene-based nanocomposites with high surface areas or the layered structures of graphene composites [12, 13]. These unique architectural structures can improve the wettability of the graphene materials, enhance electrolyte ion transportation and improve the accessibility of electrolytes to the electrode surface [13]. Xu *et al.* reported the 3D hierarchical porous structure of holey graphene with a gravimetric capacitance of 310 F/g in an aqueous electrolyte. This 3D graphene framework provided large ion-accessible surface areas and efficient electron and ion transport pathways [14]. Yang *et al.* introduced the liquid-mediated process to design graphene compact film with low ion transport resistance and capacitance of 170.6 F/g [15]. Wu *et al.* prepared a composite film of rGO and polyaniline (PANi) nanofibers showed capacitance of 210 F/g [12].

Metal-organic frameworks (MOFs) are an emerging class of the highly porous materials, which are commonly employed as a platform to prepare 3D hierarchical porous carbon due to their high surface area and high porosity [13]. In general, MOF materials are made from chemically strong bonds between metal ions (e.g. Cu^{2+}, Zn^{2+}, Co^{2+}, Mg^{2+}, Ni^{2+}, Al^{3+}) and organic ligands to form 3D structures with identical pore size distribution [16]. Their highly porous structures with high surface areas make them ideal candidates for

applications in gas absorption, chemical sensor, catalysis and drug delivery [17-24]. Besides, these properties also make them especially attractive for energy storage applications such as batteries and supercapacitors [25-33]. The conversion of diamond-like shape HKUST-1 into microrods has been focused amongst other MOF materials as it is simple to make and can be scaled up with generally good properties. HKUST-1, which is chemically made from paddle wheel dimeric copper carboxylate units and benzene-1,3,5-tricarboxylate groups [34] has gained significant interest due to its high surface area (1700 m^2/g), a relatively simple synthesis [35-38], making it attractive to be used for energy storage applications.

The combination of MOF derived metal oxides and nanoporous carbon with graphene or CNTs was recognised by several groups as an excellent opportunity to create a new class of composite materials with outstanding properties for supercapacitors applications [25, 39, 40]. *Cao et al.* prepared the rGO-wrapped MoO_3 by mixing GO with molybdenum-based MOFs followed by annealing in the air [41]. This composite delivered a specific capacitance of 617 F/g at a current density of 1 A/g, showing 87.5 % capacity retention after 6000 cycles. A Mn_2O_3 nanowire coated 3D graphene network free-standing electrode was synthesised by in situ growth of a Mn-based MOF on graphene followed by thermal treatment [42], providing a capacitance of 471.1 F/g at 0.2 A/g. *Deng et al.* designed a honeycomb-like porous Co_3O_4/3D graphene networks/nickel foam to obtain the capacitance of 321 F/g at a constant current density of 1 A/g [43]. These reports highlighted that the electrochemical performance of these combined hybrid materials was significantly increased. The explained reason was that the micro- and meso-pores sites generated in these structures enhanced their specific surface area and acted as electrolyte ion reservoirs providing a continuous supply of electrolyte ions, improving the contact between the electrode material and the electrolyte. Furthermore, graphene enhances the electrical conductivity and improves charge and electron transfer rates providing further enhancement to the material properties and performances.

To date, graphene-MOF nanocomposites have been synthesised by multiple approaches including hydro-thermal, direct mixing, in situ growth and pickering emulsion polymerisation, atomic layer decomposition [44]. In situ growth of MOFs in graphene was the most common approach, but its synthetic method suffered from the aggregation of graphene due to MOFs precursors, inhomogeneous structure owning to a random distribution of MOFs in graphene, and highly restacked graphene sheets formation in the

nanocomposite [44]. Therefore, a convenient approach for the preparation of graphene-MOF composites is still challenging that needs to be addressed.

Herein, in this chapter, a new approach which overcomes these mentioned issues and combines MOFs and graphene to create the highly porous 3D architecture required for high-performing supercapacitors. The rationale is to combine the 2D structure of graphene with 1D structure of HKUST-1 microrods to generate a composite material with superior electron and charge transport properties. The proposed concept presented in Figure 3.1 bases on two innovative approaches. Firstly, a simple synthetic method was used by mechanical grinding to combine HKUST-1 microrods with GO and assemble them into a unique 3D composite structure. The blending of these two components under an aqueous shear mixing condition, allowed the HKUST-1 fragments or seeds to grow rapidly (~ min) into nano-to-micron diameter rods. These HKUST-1 microrods are distributed homogeneously throughout the GO matrix and act as spacers to prevent the GO sheets from restacking and agglomerating that support to form strong 3D structures. The composite film was further treated to impact conductive properties on the material, allowing it to act as electrodes for supercapacitors. This secondary step used a CO_2 laser scribing to covert GO into the conductive and porous material, referred to as L-rGO. In contrast, conventional GO to rGO conversion methods require either thermal or chemical reduction, which is inapplicable as they can damage or dissolve highly sensitive HKUST-1s [45-47]. The L-rGO and carbonized HKUST-1 (C-MOF) are simultaneously formed by the ultrafast laser beam irradiation improving porosity, conductivity and providing the excellent electrochemical properties required to deliver high specific capacitance and other performances. The preparation concept based on these two steps is simple, fast, low-cost, environmentally-friendly and scalable, and can be applied for engineering new types of 3D materials for multiple applications.

3.2 Experimental

3.2.1 Preparation of HKUST-1 microrods

To study the growth of HKUST-1 in milliQ-water HKUST-1 crystals (10 mg) were placed into an agate mortar, followed by addition of water (1 mL). The mixture was then manually ground, and each sample was taken out for different intervals ranging from 5 sec to 20 min. The samples were then totally dried at 50^{o}C in a convection oven for SEM imaging to study their morphology changes. Moreover, to investigate the effect of grinding on the conversion of HKUST-1s, their crystals were immersed in water for the different intervals of 1, 5, 30 min and 24 h. Finally, the growth selectivity characteristics of HKUST-1s were also investigated in organic solvents, including ethanol, acetone, dimethyl-formamide (DMF), and in the dry state. These samples were then dried at 50 ^{o}C (3 h) in a convection oven for SEM capturing.

3.2.2 Synthesis of GO-HKUST-1 composite

GO solution (5 mL of 2 mg/mL) was mixed with HKUST-1 crystals (10 mg) in the weight ratio of 1:1 in an agate mortar. The mixture was then ground manually for 20 min and then transferred to a beaker and stirred for 10 min. The final solution became a completely homogenous paste that was used for fabricating large-area free-standing films. The GO/HKUST-1 composite films were then made by drop-casting the GO-HKUST-1 solutions onto a 20-cm-diameter glass petri dish and left in a fume hood for 2 days. The resulting thin films were peeled off with their smooth surfaces. Furthermore, GO/HKUST-1 composites with different weight ratios (1:1, 1:2, 2:1) were fabricated to optimise their morphologies.

3.2.3 L-rGO-C-MOF nanocomposites for supercapacitor application

The GO/HKUST-1 composite films in the sizes of 2x2 cm were treated by the laser (40W CO_2 laser, Full spectrum Laser H-Series)with the total power of 40 watts, in which 20% of the total power was applied (equivalent to 8 watts) and the laser wavelength is 10.6 micrometers under the ambient atmospheric condition, which was the optimum parameter for treating them. The L-rGO-C-MOF composites were formed and then cut into two smaller squares of 1x1 cm, which were used as electrodes for electrochemical characterisations. Moreover, we also fabricated GO thin films in the same way and then laser-scribed them as control samples in this research.

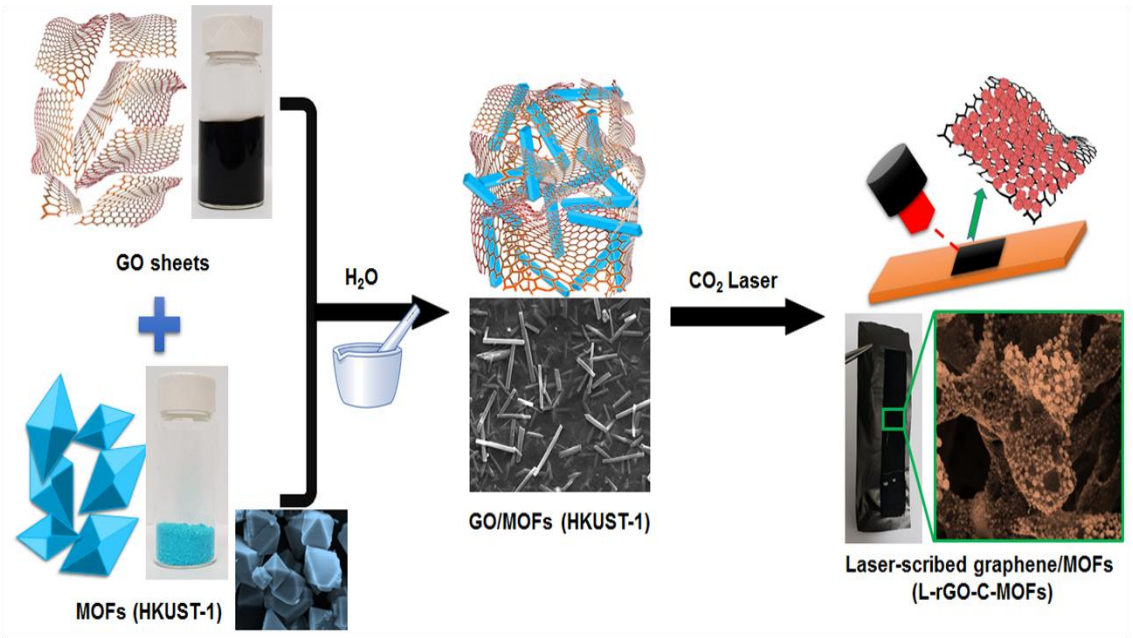

Figure 3.1 The schematic diagram of the preparation approach of the GO/HKUST-1 composite prepared by the mechanical shear blending of HKUST-1 and GO in an aqueous mediation and then the laser treatment (scribing) for forming highly porous 3D nanostructured composites used as electrodes for supercapacitor applications.

3.2.4 Specific surface area characterisation

Methylene blue (MB) procedure [48] was used to measure the specific surface area of L-rGO and L-rGO-C-MOF nanocomposites. It is a two-step method which includes the calibration curve and preparation samples for specific surface area experiment.

To prepare the calibration curve 20ml of MB in water was prepared, and different concentrations of methylene blues should be made including 0.125, 0.25, 0.5, 1, 2, 3, and 4 ppm as in Table 3.1. The relationship between the absorbance and the concentration of MB is illustrated in Figure 3.2.

To prepare the samples for SSA experiment, firstly, the L-rGO and L-rGO-C-MOF composites in the forms of fine powders in water at a concentration of 2 mg/mL were sonicated for 1 h each to avoid the aggregation of graphene sheets. In the next step, one mL of each L-rGO and L-rGO-C-MOF composite solution was put into 50 ml test tube and then topped it up to 30 ml with MB separately to form 30-ml-solutions. For the control sample of each material, 1 mL of water was added to 50 ml test tube and topped it

up to 30 ml with MB. Next, all the samples were shaken up for 24 hours and then read the Abs on the UV-Vis instrument.

Table 3.1 The relationship between the concentration of MB (ppm) and absorbance

Concentration of MB (ppm)	Absorbance (Abs)	Concentration of MB (ppm)	Absorbance (Abs)
0.125	0.055	2	0.504
0.25	0.086	2.5	0.613
0.5	0.144	3	0.725
1	0.265	4	0.959

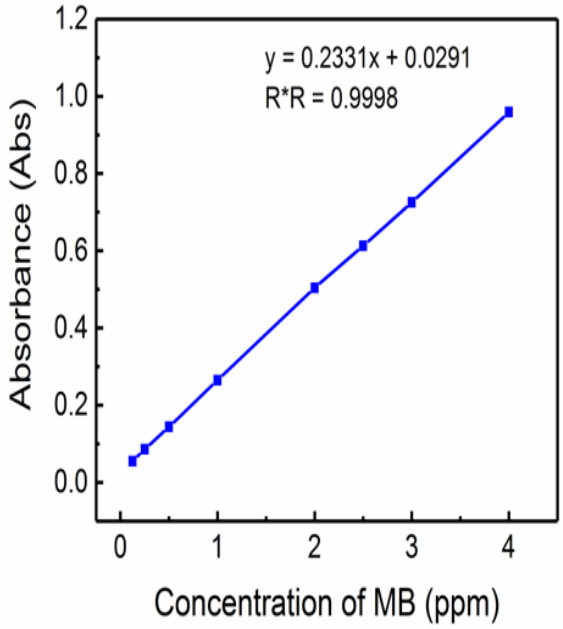

Figure 3.2. The relationship between absorbance and concentration of MB.

The following equation was used to calculate the SSA,

$$SSA = \frac{N_A A_{MB}}{m_{MB}} \frac{(C_0 - C_e)v}{m_{GN}}$$

where N_A is Avogadro number (6.02×10^{23}/mol), A_{MB} is the covered area of per MB molecule (typically assumed to be $1.35^* 10^{-18}$ m^2), C_0 and Ce are the initial and equilibrium concentrations of MB, respectively, V is the volume of the MB solution, m_{MB} is the relative molecular mass of MB (319.85 g/mol), and m_{GN} is the mass of the sample in gram.

3.2.5 Electrochemical characterisation

To measure the electrochemical characteristics of electrodes, two gold substrates were used as the standard collectors and the 1 M $NaNO_3$ was used as an electrolyte solution. Two L-rGO-C-MOF films (1x1 cm) were sandwiched between two gold foils, and a piece of filter paper was used as a separator. The L-rGO electrodes were employed as the control samples. All electrochemical measurements were conducted by employing cyclic voltammetry and galvanostatic charge and discharge (CD) in two-electrode cell configuration by CHI 760 E Electrochemical workstation (Figure 3.3).

The specific capacitance is calculated from cyclic voltammetry curves by the following equation [49]:

$$C_{wt} = \frac{4\int_{v1}^{vn} i\,dV}{m\,s\,\Delta V} \qquad (1)$$

where C_{wt} is the specific capacitance (F/g), $\int_{v1}^{vn} i\,dV$ is the integrated area of cyclic voltammetry curve, s is the scan rate (V/s), ΔV is (2 x the voltage window) from E_1 to E_2 and then back to E_1 (V), and m is the mass of the active materials on electrodes (g).

The specific power (P) in W/kg and specific energy (E) in Wh/kg are calculated by the following equations [49]:

$$P = \frac{\int_{V1}^{Vn} idV}{m}\ ,\quad E = \frac{\Delta V \int_{V1}^{Vn} idV}{3600ms} \qquad (2, 3)$$

where m is the mass of the active materials on both electrodes (kg). The other parameters are the same as those in equation (1).

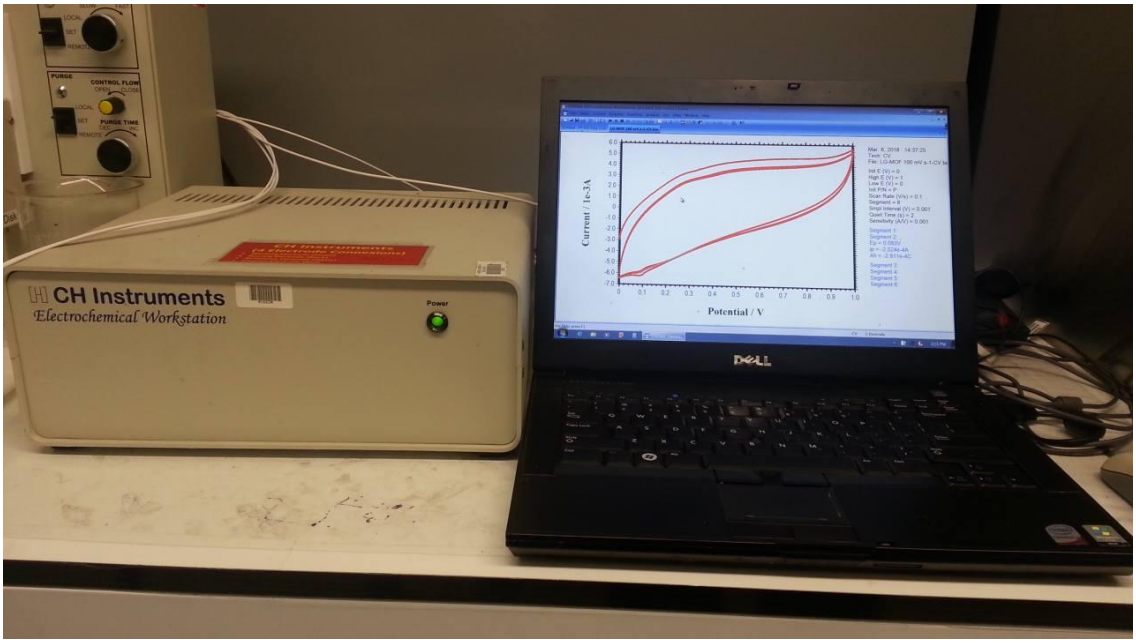

Figure 3.3. Electrochemical workstation CHI 760 E system

3.3 Results and discussions

3.3.1 Characterisations of GO/HKUST-1

It is well-known that solvents have a major influence on both the structural stability of the coordination mode of copper atoms and the crystal growth direction of HKUST-1 [50-52].

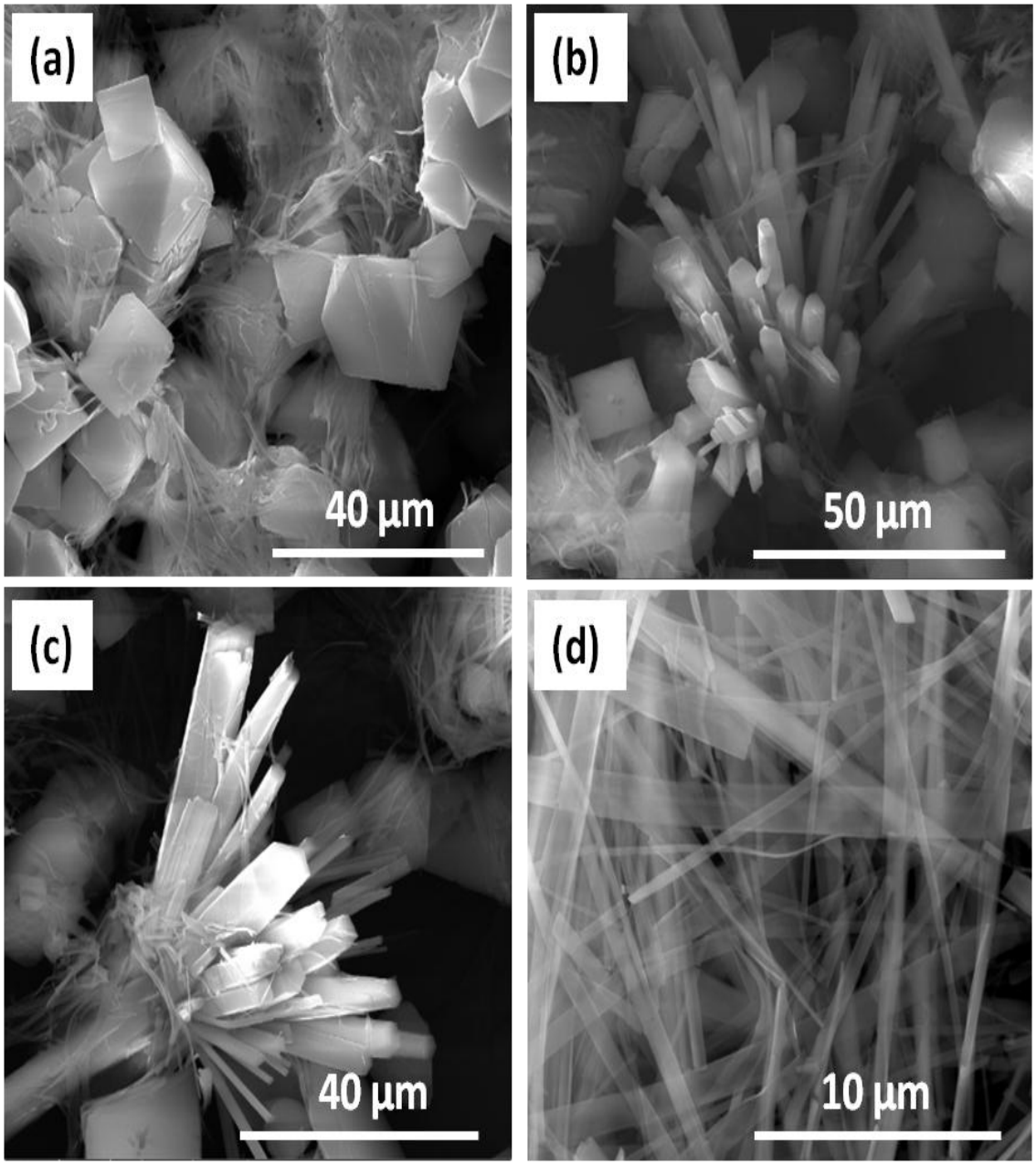

Figure 3.4. The morphology of HKUST-1 microrods in water without grinding: (a) 1 min, (b) 5 min, (c) 30 min, and (d) 24 h.

The effect of the solvents (water, ethanol, acetone and DMF) and the grinding time were initially investigated to explore the structural transformation of HKUST-1s from their diamond-like structures to mirorods. Upon immersing in water, the HKUST-1 diamonds were found to have significant structural changes at different immersion time with a

conversion of the octahedral crystals of HKUST-1 into microrod crystals (without grinding) as shown in Figure 3.4a-c. It is likely that water molecules intercalate into the HKUST-1 atoms as well as react with Cu+ ions, and they then grow into separate microrods. However, a complete conversion of HKUST-1 into its fine microrod structure can consume a long time of up to 24 h, as shown in Figure 3.4d.

To increase the rate of transformation reaction of HKUST-1 into microrods in water a grinding technique was employed. The key role of grinding activity is to provide more

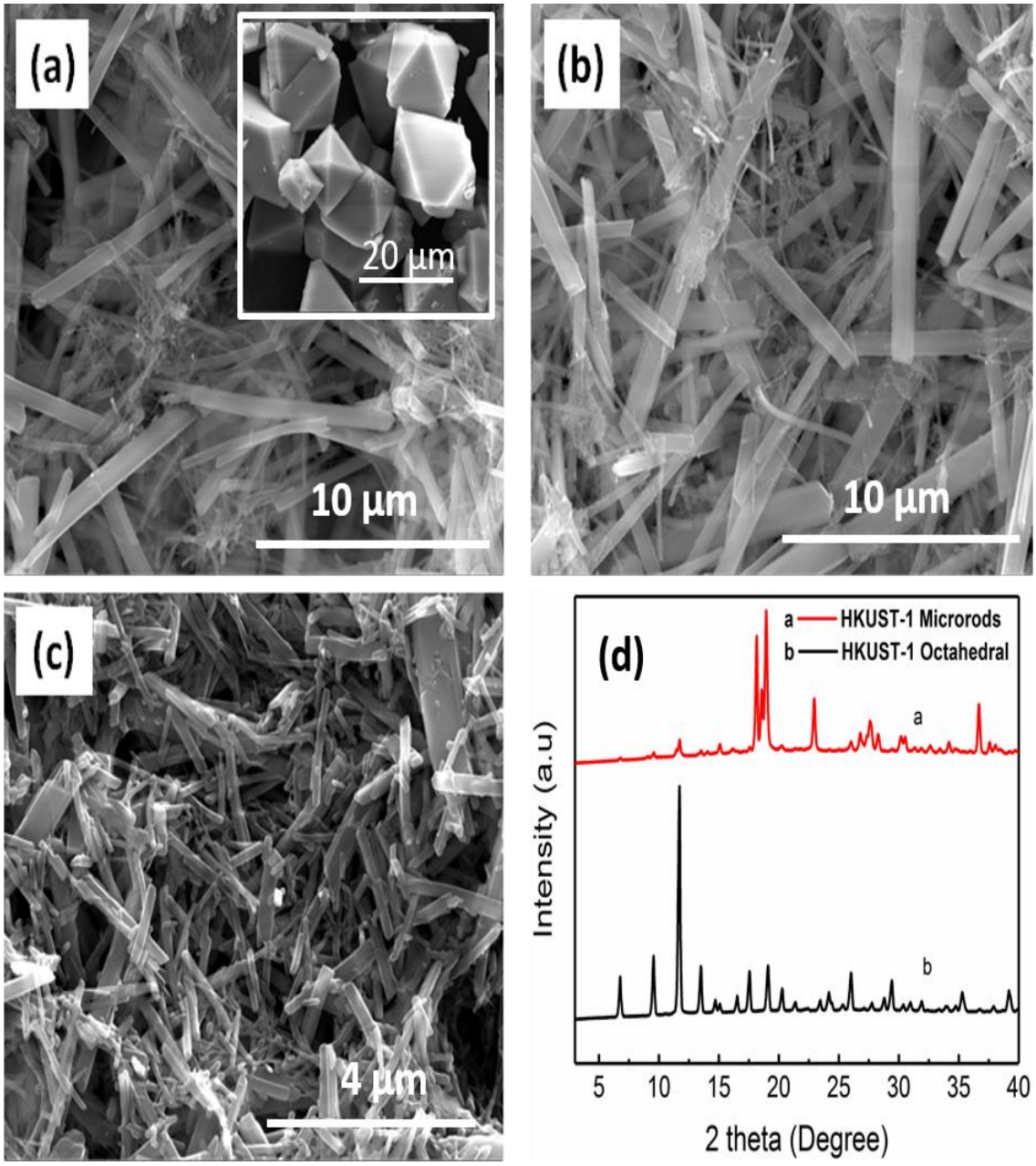

Figure 3.5. SEM of HKUST-1 in water with grinding at different times (a) 20 sec and inset is the original morphology of HKUST-1 octahedral diamonds, (b) 60 sec, (c) 20 min, and (d) XRD.

energy for cracking weak bonds of Cu ions in the framework structure and separate the formed microrods, which supports these microrods to intensively contact with water molecules and grow more rapidly. It was found that the full conversion from octahedral crystals to microrods was achieved within very short 20 sec to 20 minutes in contrast to the 24 hr required in water with no agitation. Series of SEM images of obtained HKUST-1 microrods for different grinding times are presented in Figure 3.5a-c. The length of these rod structures was from 10 to 20 μm, while their diameters are ranging from a majority of 50-100 nm to a minority of micrometres indicating an influence of the grinding times on their dimensions.

XRD results of HKUST-1s before and after their conversion into microrods were presented in Figure 3.5d. The shift in XRD spectrum of HKUST-1 diamonds shows a good agreement with the previous studies by a number of peaks at diffraction angles (2θ) of 6.78°, 9.56°, 11.72°, 13.5°, 17.56°, 19.1°, 26.4° corresponding to the (200), (220), (222), (400), (511), (440), (731) planes, respectively [53].

Meanwhile, the XRD spectrum of HKUST-1 microrods illustrates two new strong peaks at 36.68°, 43.2°, which are attributed to the crystal planes of Cu_2O (111), Cu_2O (200), respectively. Moreover, it is also observed that the other peaks belong to the copper (Cu) remaining in the formed microrods at 18.16°, 18.94°, 22.96°, which are in turn assigned to the (511), (400), and (444) planes, respectively. These results show that water and grinding can rapidly transform HKUST-1 octahedral crystals into new 1D microrods shapes without causing a complete collapse of the framework. With the used XRD equipment, the relative pecent of HKUST-1 and Cu_2O is possible to determine with a sofware for the calculation of peak intensity and FWHM of the phase. In addition, with the SEM images in Figure 3.5, it is supposed that all diamond HKUST-1s are transformed into HKUST-1 microrods with Cu_2O and Cu ions existing in their chemical structure. Other organic solvents, including ethanol, acetone and DMF, were also mixed with HKUST-1 in the same grinding approach; however, they did not produce the microrod morphology, (Figure 3.6a-d). The reason may be due to the large sizes of these solvent molecules and their chemical properties, which prevent them from intercalating and reacting with copper ions in the framework. These confirm that water is not only the most effective but also the most selective solvent to convert HKUST-1 from a well-known diamond-like shape into its microrod structure amongst typical organic solvents investigated.

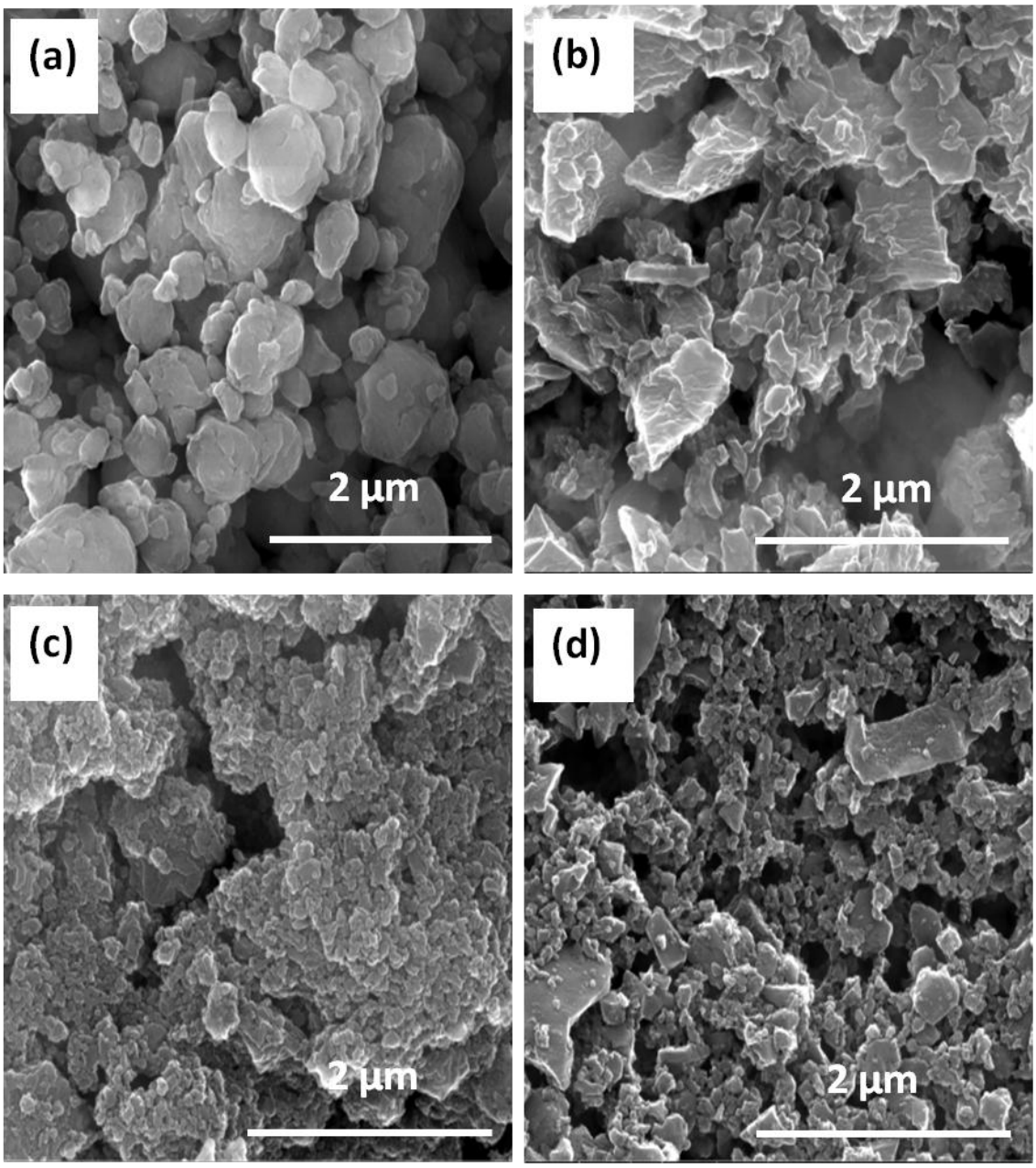

Figure 3.6. HKUST-1 diamonds ground in other solvents: (a) in the dry state, (b) ethanol, (c) acetone, and (d) DMF.

The phenomenon of HKUST-1 microrods grown in an aqueous solution plays an essential role in a well-dispersed mixing method. The SEM images of the GO/HKUST-1 composite prepared by mixing HKUST-1 and GO in an aqueous solution are presented in Figure 3.7a-b. It is clearly observed that the microrods randomly distributed and intercalated into the GO sheet matrix, and some of microrod crystals stacked on the surface of the GO sheets which are likely due to static interactions between HKUST-1 microrods and the oxygen-containing functional groups of GO.

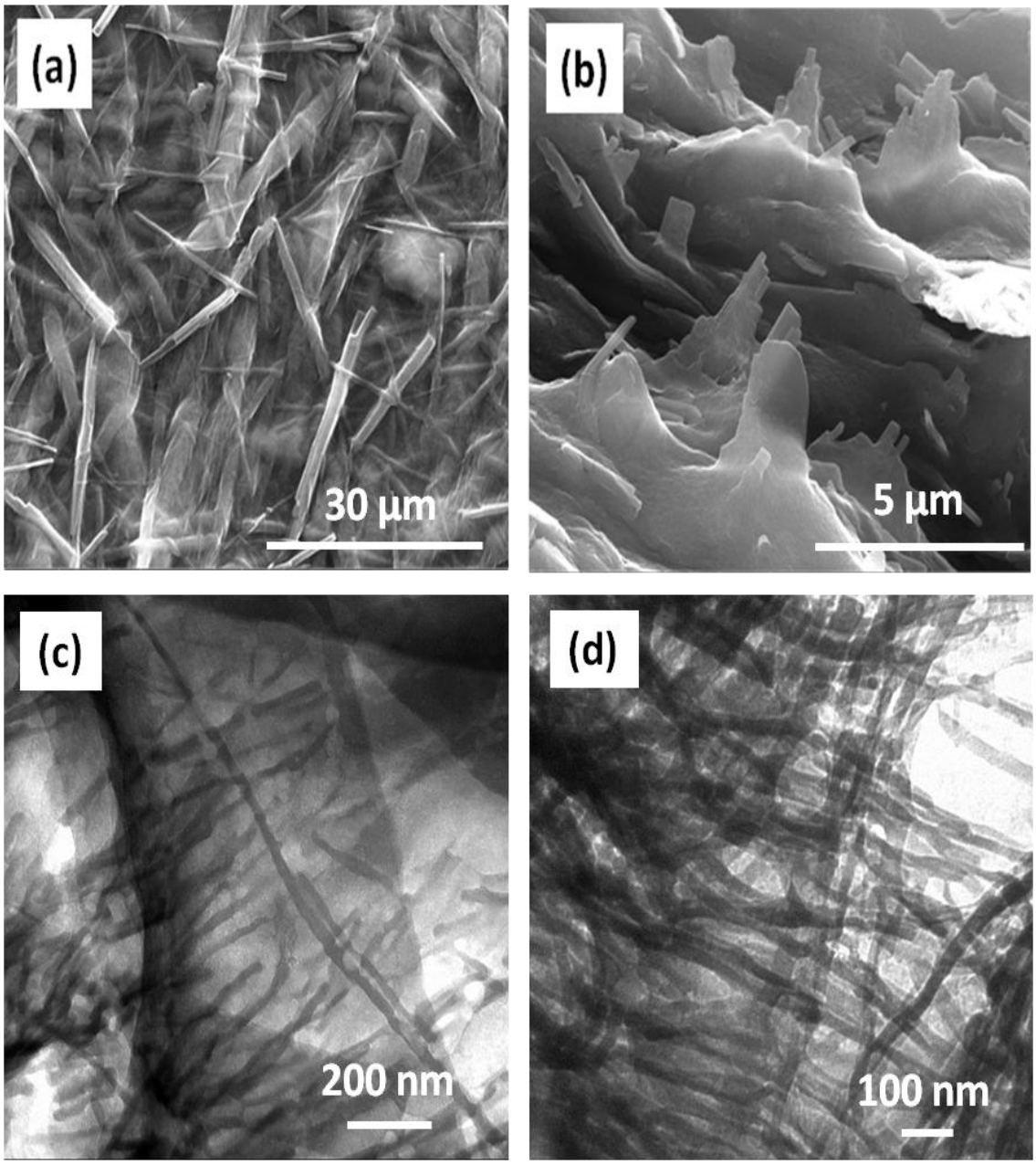

Figure 3.7 Morphology structure of GO/HKUST-1; (a) SEM image of the top view, (b) SEM image of the cross-section surface, and (c, d) TEM images with HKUST-1 microrods are the darker lines and GO sheets are the brighter areas.

The intercalation of the microrods stems from the effect of the shear force during the grinding process, and they act as the spacers between GO sheets. The TEM images of GO/HKUST-1 composite (Figure 3.7c-d) provides more evidence of the HKUST-1 microrods grown in GO matrix at the nanoscale.

3.3.2 Highly porous L-rGO-C-MOF nanocomposites for designing supercapacitors

HKUST-1 microrods exhibit a highly chemical sensitivity to the common reducing agents like hydrazine and hydroiodic acid (HI), in which Cu atoms and Cu_2O are dissolved in these chemical agents, leading to the total collapse of the HKUST-1 microrod structure. To preserve the structure of the GO/HKUST-1 composite after reduction, the laser scribing was applied yielding a composite material, satifying the critical features of high electrical conductivity and high surface areas for high-performance supercapacitor electrodes. The laser scribing, which has been previously unused to treat MOFs-GO composites, has multiple benefits including the simultaneous reduction transformation of GO into L-rGO, carbonization of HKUST-1 microrods to conductive carbons (C-MOFs), and the production of an open porous network of L-rGO unique laser scribed graphene composite films [54, 55].

SEM images of the top-view and cross-section surface of the L-rGO-C-MOF composite film after the laser scribing process show the substantially morphological changes of composite materials, as shown in Figure 3.8a-d. The HKUST-1 microrods were carbonised and converted their morphology from microrods into porous nanoparticles forming a characteristic 3D network with L-rGO structures. The C-MOF structure was formed upon the decomposition of the organic ligands under the local effect of laser energy during the treatment process. The created L-rGO-C-MOF composite shows a 3D hybrid structures with high porosity and a high specific surface area of ~ 600 m^2/g measured by the methylene blue (MB) absorption method. Such a high specific surface area allows an increased electrolyte ion interaction with the electrodes, which significantly increases the performance of supercapacitors. The higher specific surface area of L-rGO-C-MOF in comparison with that of L-rGO (around 115 m^2/g) suggests that the porous C-MOF has a significant contribution to the formation of the porous composite structure and the scribed laser is an excellent method to produce the typical type of materials.

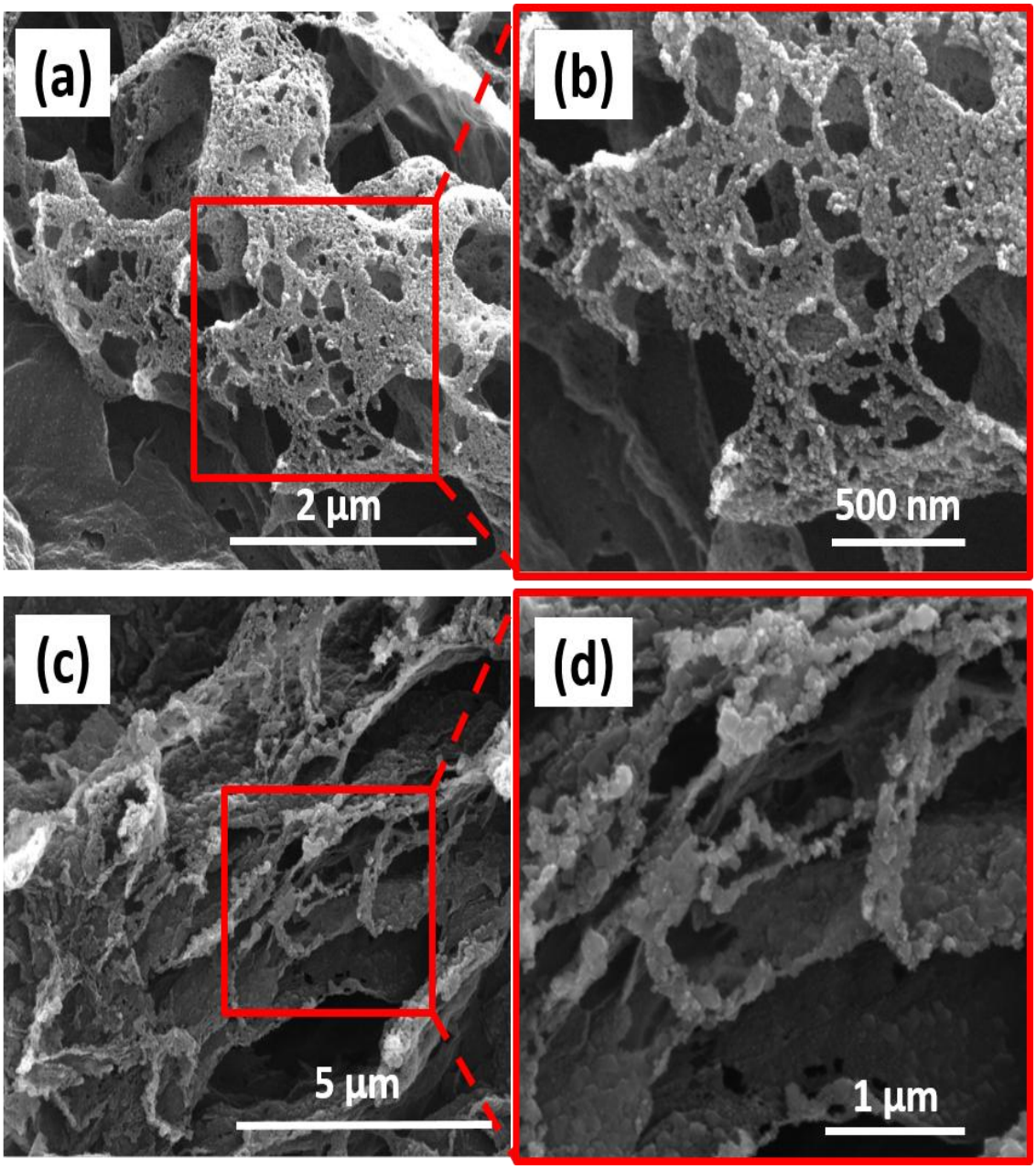

Figure 3.8. SEM images of L-rGO-C-MOF composite (a, b) top-view and (c, d) cross-section surface.

In order to determine the effectiveness of the reduction and degree of carbonization of L-rGO and L-rGO-C-MOF composites, XRD characterisation was performed, as shown in Figure 3.9a. The XRD pattern of L-rGO material (curve a) shows a sharp diffraction peak at 25.72°, which confirms the recovery of C-sp^2 graphene structure from the C-sp^3 structure of GO and the removal of oxygen-containing functional groups on GO under the impact of laser energy. The XRD spectrum of L-rGO-C-MOF composite (curve b) exhibits many diffraction peaks at 9.58°, 11.49°, 16.93°, 18.83°, 19.46°, 21.37°, and 22.91°, which correspond to the (220), (222), (422), (440), (600), (620), and (444) planes

in the crystal structure of C-MOFs, respectively. These diffracted peaks confirm the evidence of the presence of remaining Cu after laser treatment. Moreover, the shifted sharp peak of L-rGO-C-MOF was at 26.08°, confirming the recovery of the graphene structure, and the peaks at around 43.39° and 74.11° confirm the presence of Cu_2O.

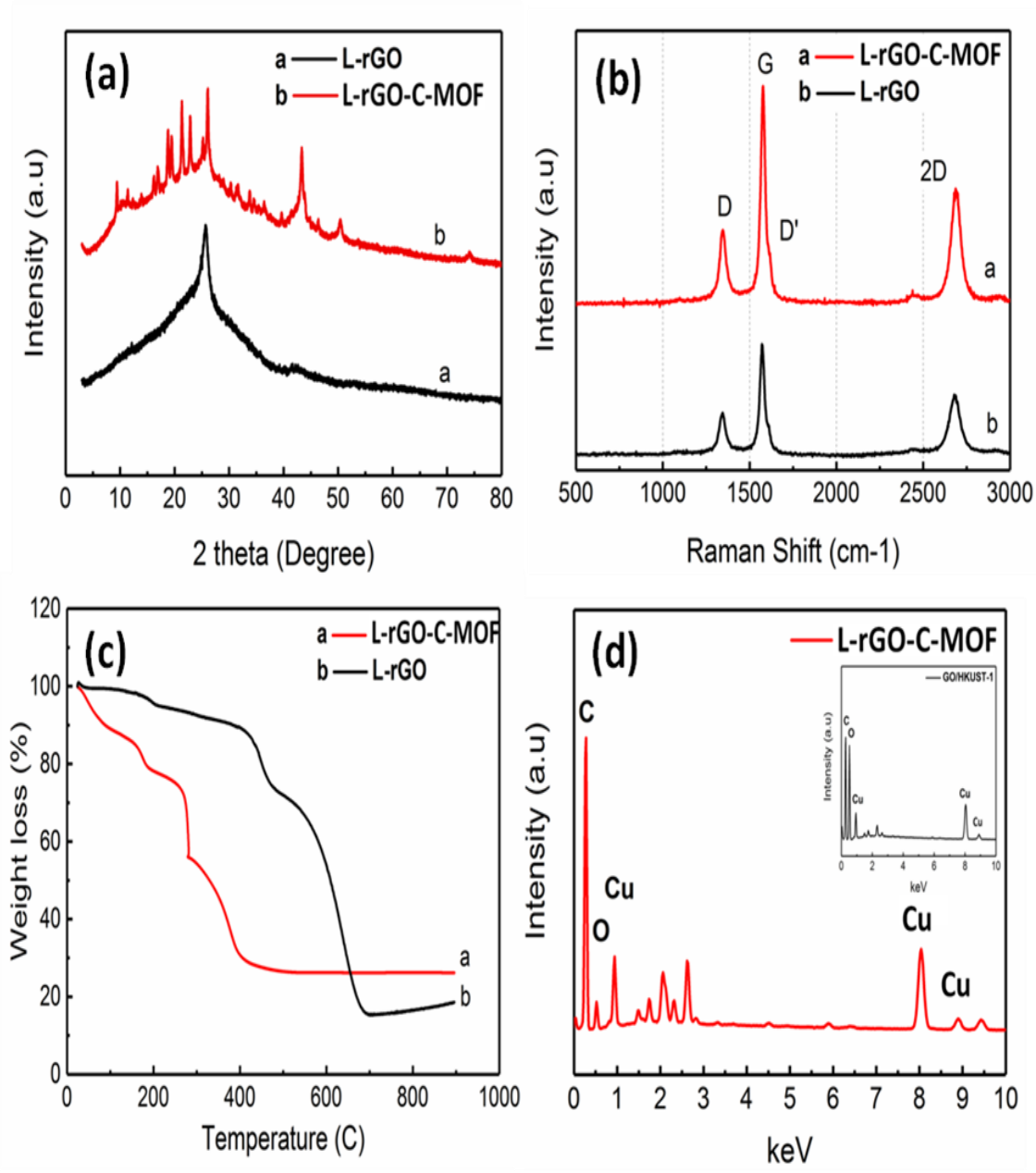

Figure 3.9. X-ray diffraction spectra (a), Raman spectra (b), Thermal gravity analysis (c) of L-rGO and L-rGO-C-MOF composite, and EDAX spectrum of L-rGO-C-MOF composite (d) with inset is the EDAX of GO/HKUST-1 composite.

Raman characterisation of the L-rGO and L-rGO/C-MOF composites prepared by laser scribed approach indicates that the GO has been reduced and HKUST-1 microrods carbonised as clearly observed in Figure 3.9b. The Raman spectra of both L-rGO and L-

rGO-C-MOF showed two dominant bands of D, G, which were appeared at approximately 1350 and 1580 cm^{-1}, respectively. The D and G band presents the defect level and tangential vibration of carbon, respectively, and the analysis of the intensity ratio of I_D/I_G provides a useful indicator to estimate the disordered levels of crystal structures of carbon. Raman analyses of the L-rGO-C-MOF composite and L-rGO showed a significant decrease in the I_D/I_G ratio, 0.626 and 0.422, respectively, compared with that of GO (0.83), confirming the decreasing disordered graphene sheets [56].

The decrease of I_D/I_G ratio suggests the low defect level of graphene in L-rGO and L-rGO-C-MOF composite by removing oxygen functional groups on GO and recovering the sp^2 conjugate network of graphene [57]. The significantly higher intensity ratio of I_D/I_G in L-rGO-C-MOF composite in comparison with that of L-rGO is due to the hybridised structure of expanded rGO and C-MOF patterns, leading to the more disordered structure of graphene in the composite. The 2D band, which was at 2700 cm^{-1}, and the intensity ratio of I_{2D}/I_G also provides useful information about the layer number of graphene. The Raman analyses presented that I_{2D}/I_G of both L-rGO and L-rGO-C-MOF composite was less than one, indicating the multi-layered structure of graphene [58]. However, the I_{2D}/I_G ratio of L-rGO-C-MOF was significantly higher than that of L-rGO, suggesting that the graphene in L-rGO-C-MOF composite consists of fewer layers than in L-rGO [58], which was resulted from the intercalation of microrods between GO sheets, preventing these sheets from restacking. Finally, the shoulder peak (D') at the frequency of 1620 cm^{-1}, which was partially merged with G band, also appeared in the spectra of L-rGO and L-rGO-C-MOF composite. The presence of this band provides the evidence of the formation of active carbon under the laser energy, in which nonzero phonon states above G band became activated due to the phonon confinement [59]. The absence of Cu from Raman spectra is possibly due to the random measurements and the tiny amount of Cu in the composite in comparison with that of C and the other elements. The more graphitic structure of L-rGO-C-MOF composite compared with that of L-rGO was obtained from the analysis of $I_{D'}/I_G$ ratios, respectively, which was owing to the contribution of C-MOF in the composite structure. The intensity ratios of Raman bands were summarised in Table 3.2.

Table 3.2 Comparison of band intensity ratios of L-rGO and L-rGO-C-MOF.

Material	Band intensity ratio		
	I_D/I_G	$I_{D'}/I_G$	I_{2D}/I_G
L-rGO	0.422	0.315	0.576
L-rGO/C-MOF	0.626	0.563	0.734

To determine the degree of the reduction and carbonisation, both L-rGO and L-rGO-C-MOF composite were further measured by TGA to evaluate their thermal characteristics (weight loss vs temperature). A significant difference in the thermal stability of L-rGO and L-rGO-C-MOF composite was observed in the TGA (Figure 3.9c). The L-rGO thin film is highly stable to 430°C with only a slight decrease in weight (~10 %), which is due to the evaporation of the remaining water. After 430°C, a significant change in material occurs as the rGO decomposes, leaving less than 15% of material undecomposed, which may be impurities. Meanwhile, L-rGO-C-MOF composite exhibits low thermal stability in the temperature range of 25°C-430 °C with a major weight loss of ~70 %, which is due to the evaporation of high content of water trapped in microrod structure and the decomposition of remained unburned organic ligands after laser treatment. After that, the temperature until 900^{o}C witnesses a stable thermal property of L-rGO-C-MOF composite with a constant weight of ~25 %, which includes Cu and Cu_2O. Although the data of Raman spectroscopy and TGA measurement of unscribed HKUST-1/GO composite is propably proper to observe, in the current work it has been unneccessary to have that in clarifying the effect of laser. This will be considered as the future work.

In order to further confirm the reduction and carbonisation, L-rGO-C-MOF composite was characterised by EDAX to determine the presence of chemical elements, as shown in Figure 3.9d. The EDAX spectrum shows the presence of three main elements in L-rGO-C-MOF composite, including carbon, oxygen, and copper. The higher content of carbon in L-rGO-C-MOF composite in comparison with that in L-rGO material results from the formation of active carbon via the carbonisation process of HKUST-1 microrods. The atomic ratio of C/O in GO, GO-HKUST-1 composite (Figure 3.9d inset), and L-rGO/C-MOF were 1.2 [46], 1.45 and 18.1 (this work), respectively. These results confirm the effective removal of oxygen functional groups and the recovery of the C-sp^2 structure of graphene by laser.

Table 3.3 Weight and atomic percentages of elements in L-rGO-C-MOF

Elements	Weight %	Weight σ	Atomic %
C	80.75	0.61	92.06
O	5.92	0.61	5.07
Cu	13.33	0.28	2.87

To investigate the supercapacitor performance of the unique structure L-rGO-C-MOF electrodes, the symmetrical supercapacitor in an aqueous electrolyte of 1 M $NaNO_3$ was fabricated. $NaNO_3$ salt was specifically selected to prevent the dissolution of Cu and Cu_2O that is impossible with other conventional electrolytes such as H_2SO_4 acid. Figure 3.10 summarises the electrochemical characteristics of the L-rGO and L-rGO-C-MOF supercapacitors performed by a series of measurements including gravimetric capacitance, charge-discharge behaviour and cyclic retention. The cyclic voltammetry curves (CVs) show that the L-rGO electrode has a rectangular CV curve, indicating ideal EDL capacitive behaviour, as observed in Figure 3.10a. When the laser beam carbonised HKUST-1 microrods, it produced Cu_2O residuals embedded between the graphene sheets, which store charges through fast and reversible Faradaic redox reactions [60]. As a result, a significant improvement in the current density is observed, indicating the higher performance of supercapacitor not only from the contribution of Cu_2O but also for the 3D structure of L-rGO-C-MOF electrodes as seen in Figure 3.10a. The L-rGO-C-MOF electrodes exhibit a reproducible and stable capacitive behaviour with increasing scan rates from 5 to 100 mV/s (Figure 3.10b).

The galvanostatic charge-discharge (CD) curves of L-rGO and L-rGO-C-MOF at 1 A/g are illustrated in Figure 3.10c-d, respectively. The L-rGO thin film shows a CD curve with a symmetric triangular-shape, confirming ideal EDL behaviour. However, L-rGO-C-MOF composite displays a deviation from linearity and longer charge and discharge time than L-rGO due to the contribution of the pseudocapacitance nature of Cu_2O and the porous structure of L-rGO-C-MOF that enhances the energy storage capacity as shown in Figure 3.10c. The galvanostatic CD behaviours of the symmetric supercapacitor were tested with different current densities with the voltage window of 0-1 V (Figure 3.10d). When the current density increased from 2 to 5 A/g, the CD curves shape unchanged, indicating the robustness and excellent reversibility of the hybrid composite materials during the CD process.

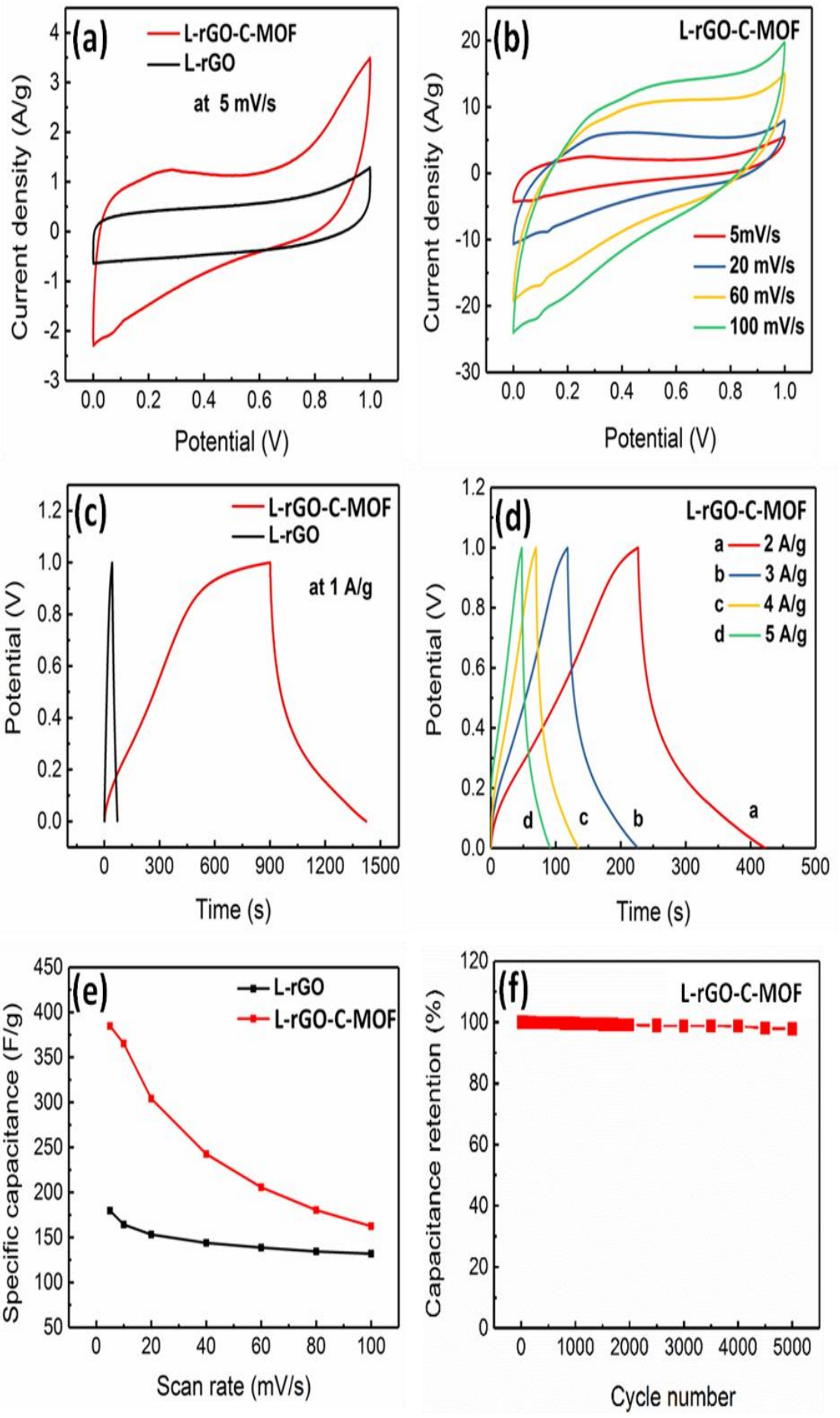
(a)
L-rGO-C-MOF
L-rGO
at 5 mV/s
Current density (A/g)
Potential (V)
(b)
L-rGO-C-MOF
5mV/s
20 mV/s
60 mV/s
100 mV/s
Current density (A/g)
Potential (V)
(c)
L-rGO-C-MOF
L-rGO
at 1 A/g
Potential (V)
Time (s)
(d)
L-rGO-C-MOF
a 2 A/g
b 3 A/g
c 4 A/g
d 5 A/g
Potential (V)
Time (s)
(e)
L-rGO
L-rGO-C-MOF
Specific capacitance (F/g)
Scan rate (mV/s)
(f)
L-rGO-C-MOF
Capacitance retention (%)
Cycle number

Figure 3.10 A comparison of cyclic voltammetry of L-rGO-C-MOF composite and L-rGO (a), cyclic voltammetry of L-rGO-C-MOF at different scan rates (b), charging and discharging behaviour of L-rGO-C-MOF and L-rGO at 1 A/g (c), charge and discharge behaviours of L-rGO-C-MOF composite at different current densities (d), a comparison of specific capacitance of L-rGO-C-MOF and L-rGO at different scan rates (e), and the cyclic retention of L-rGO-C-MOF composite (f).

As shown in Figure 3.10e, the specific capacitance of both L-rGO and L-rGO-C-MOF electrodes decreased significantly with the increase of scan rate. More specifically, the L-rGO-C-MOF composite delivered specific capacitances of 390, 361.6, 300, 240.4, 203.7 178.6, and 160.8 F/g at different scan rates of 5, 10, 20, 40, 60, 80 and 100 mV/s, respectively. That can be attributed to the limited diffusion of $NaNO_3$ electrolyte ions to the surface of electrodes from the stable double layers at a high scan rate [61]. That decreasing trend of the supercapacitor capacitance indicates that the symmetric supercapacitor has a good rate capability, which is attributable to the high specific surface area, carbonised and porous structure of the composites.

The cyclic stability of the L-rGO-C-MOF electrode was tested by CD testing at a current density of 10 A/g in Figure 3.10f. The results show that the symmetric supercapacitor exhibits superior cyclic durability with a high cyclic retention rate of 97.8% after 5000 cycles. This final test indicates that the carbonised and porous composite material fabricated in this work has outstanding cycling stability at a high current density.

Figure 3.11 presents Ragone plot, which is a relationship between specific power and specific energy. The L-rGO-C-MOF composite exhibits high specific energy of 52.9 Wh/kg at a specific power of 952.3 W/kg due to its unique porous structure. The specific energy decreased versus increased specific power; however, the 3D porous composite delivers specific energy of 22.3 Wh/kg at a very high specific power of 8037.5 W/kg. These results are much higher than other reported values for MOF-derived nanoporous carbons or metal oxides achieved by conventional methods, as shown in Table 3.4, which displays the benchmark data reported in the literature. For example, the rGO/Fe_2O_3 composite showed a high energy density of 79.2 Wh/kg at a power density of 405 W/kg, and an energy density of 25.8 Wh/kg at high power density of 8010 W/kg [44], carbon/NiO (25 Wh/kg at 225 W/kg) [62], and MOF derived CeO_2 (95.8 Wh/kg at 150 W/kg) [63]. Overall, the performance of the present supercapacitor based on 3D composites structure is well-benchmarked with that presented in the literature and reached

the top specific energy for current research of graphene capacitors. The reason could be explained for this high performance of L-rGO-C-MOF composite is owing to the fast faradic reactions occurred at copper oxide surfaces, and highly porous carbon structure, which provides large channels and conductive network to facilitate the electrolyte ions and electrons transportation.

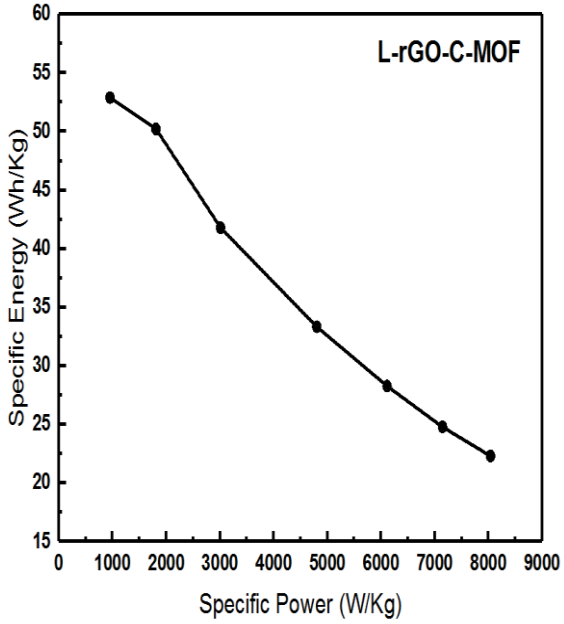

Figure 3.11. Ragone plot of L-rGO-C-MOF composite supercapacitor electrodes.

Table 3.4. Literature reported gravimetric capacitance of some MOF-graphene-based composites.

Material	Treatment method	C_{wt} (F/g)	Specific power (W/kg)	Specific energy (Wh/kg)	Cycling	Ref.
Cu-MOF-GO to L-rGO-C-MOF	CO_2–Laser	~390 (5 mV/s)	952.3 8037.5	52.9 22.3	97.8%/ 5000 cycles	**This work**
Cu-MOF/CNT to carbon	Thermal	157.9 (2 A/g)	3500	9.1	95%/10000 cycles	[64]
Mo-MOF–GO/rGO–MoO_3	Thermal	404 (0.5 A/g)	500	14	80%/5000 cycles	[65]
Ce-BTC to CeO_2	-	502 (0.2 A/g)	150	95.8	100%/5000 cycles	[63]
MIL-101 (Cr) to Cr_2O_3	Thermal	300 (2 mV/s)	-	-	-	[66]
MOF-199 to Cu–Cu2O–CuO	Thermal	750 (2 mV/s)	-	-	-	[32]
ZIF-67 to Co_3O_4	Thermal	1100 (1.25A/g)	-	24.4	95.1%/6000 cycles	[67]
Ni-BDC to carbon and NiO	Hydro thermal	886 (1 A/g)	225	25	87%/1000 cycles	[62]
Fe-MOF-GO to rGO–Fe_2O_3	Thermal	869.2 (1 A/g)	405	79.2	96.3%/5000 cycles	[44]
Mn-MOF-Gr to Gr-Mn_2O_3	Thermal	471.1 (0.2 A/g)	-	-	~ 100%/1800 cycles	[42]
Co-MOF-Gr to Gr-Co_3O_4	Thermal	321 (1 A/g)	794	7.5	88%/2000 cycles	[43]

Conclusion

A simple, green approach for the preparation of graphene and HKUST-1 composites is presented in this chapter. The GO-HKUST-1 structure can be achieved through mechanical stimuli, in which the octahedral HKUST-1 crystals chemically reacted with water and transform into microrods that intercalated between GO sheets avoiding their restacking. By employing a CO_2 laser treatment, the GO-HKUST-1 composites are simultaneously reduced GO and carbonised HKUST-1 under the ultrafast laser irradiation. The highly porous 3D architectural L-rGO-C-MOF composite materials have a high specific surface area of 600 m^2/g as well as high electrical conductivity. When the fabricated composite is applied as electrode materials in a supercapacitor, it displays a 390 F/g at 5 mV/s, the outstanding cyclic stability at 10 A/g after 5000 cycles with capacitance retention of 97.8 %. The fabricated symmetrical supercapacitor delivers a power density of 8037.5 W/kg with an energy density of 44.6 Wh/kg, which is good compared to the previous works in the literature. This work has provided new insights into the practical applications of a novel morphology, porous material for high-performance energy storage devices.

References

1. Dubal, D.P., et al., *Towards flexible solid-state supercapacitors for smart and wearable electronics.* Chemical Society Reviews, 2018. **47**(6): p. 2065-2129.
2. Hu, C., et al., *Tailored graphene systems for unconventional applications in energy conversion and storage devices.* Energy & Environmental Science, 2015. **8**(1): p. 31-54.
3. Niu, Z., et al., *Programmable Nanocarbon-Based Architectures for Flexible Supercapacitors.* Advanced Energy Materials, 2015. **5**(23): p. 1500677.
4. Shao, Y., et al., *Graphene-based materials for flexible supercapacitors.* Chemical Society Reviews, 2015. **44**(11): p. 3639-3665.
5. Wang, Q., J. Yan, and Z. Fan, *Carbon materials for high volumetric performance supercapacitors: design, progress, challenges and opportunities.* Energy & Environmental Science, 2016. **9**(3): p. 729-762.
6. Zhou, Y., et al., *In-Situ Fabrication of Graphene Oxide Hybrid Ni-Based Metal–Organic Framework (Ni–MOFs@GO) with Ultrahigh Capacitance as Electrochemical Pseudocapacitor Materials.* ACS Applied Materials & Interfaces, 2016. **8**(42): p. 28904-28916.
7. Zhu, Y., et al., *Graphene and graphene oxide: synthesis, properties, and applications.* Advanced materials, 2010. **22**(35): p. 3906-3924.
8. Liu, Y., X. Dong, and P. Chen, *Biological and chemical sensors based on graphene materials.* Chemical Society Reviews, 2012. **41**(6): p. 2283-2307.
9. Li, X., et al., *Transfer of large-area graphene films for high-performance transparent conductive electrodes.* Nano letters, 2009. **9**(12): p. 4359-4363.
10. Kim, T., et al., *Activated Graphene-Based Carbons as Supercapacitor Electrodes with Macro- and Mesopores.* ACS Nano, 2013. **7**(8): p. 6899-6905.
11. Kim, T.Y., et al., *High-Performance Supercapacitors Based on Poly(ionic liquid)-Modified Graphene Electrodes.* ACS Nano, 2011. **5**(1): p. 436-442.
12. Wu Q, X.Y., Yao Z, Liu A, & Shi G*, *Supercapacitors Based on Flexible Graphene/Polyaniline Nanofiber Composite Films.* 2010.
13. Liu, Y.L., Gaoran Guo, Yi Ying, Yulong Peng, Xinsheng, *Flexible and Binder-Free Hierarchical Porous Carbon Film for Supercapacitor Electrodes Derived from MOFs/CNT.* ACS Applied Materials & Interfaces, 2017. **9**(16): p. 14043-14050.
14. Xu, Y., et al., *Holey graphene frameworks for highly efficient capacitive energy storage.* Nature Communications, 2014. **5**: p. 4554.
15. Some, S., et al., *Highly sensitive and selective gas sensor using hydrophilic and hydrophobic graphenes.* Scientific reports, 2013. **3**.
16. Bloch, W.M., et al., *Capturing snapshots of post-synthetic metallation chemistry in metal–organic frameworks.* Nature Chemistry, 2014. **6**: p. 906.
17. Zhai, F., et al., *Crystal transformation synthesis of a highly stable phosphonate MOF for selective adsorption of CO2.* CrystEngComm, 2013. **15**(11): p. 2040-2043.
18. Al-Janabi, N., et al., *Mapping the Cu-BTC metal–organic framework (HKUST-1) stability envelope in the presence of water vapour for CO2 adsorption from flue gases.* Chemical Engineering Journal, 2015. **281**: p. 669-677.
19. Rowsell, J.L. and O.M. Yaghi, *Strategies for hydrogen storage in metal--organic frameworks.* Angew Chem Int Ed Engl, 2005. **44**(30): p. 4670-9.
20. Lin, K.-S., et al., *Synthesis and characterization of porous HKUST-1 metal organic frameworks for hydrogen storage.* International Journal of Hydrogen Energy, 2012. **37**(18): p. 13865-13871.
21. Ranjan, R. and M. Tsapatsis, *Microporous Metal Organic Framework Membrane on Porous Support Using the Seeded Growth Method.* Chemistry of Materials, 2009. **21**(20): p. 4920-4924.
22. Kreno, L.E., et al., *Metal-organic framework materials as chemical sensors.* Chem Rev, 2012. **112**(2): p. 1105-25.

23. Lee, J., et al., *Metal-organic framework materials as catalysts.* Chem Soc Rev, 2009. **38**(5): p. 1450-9.
24. Horcajada, P., et al., *Metal–Organic Frameworks as Efficient Materials for Drug Delivery.* Angewandte Chemie, 2006. **118**(36): p. 6120-6124.
25. Zhao, Y., et al., *Metal organic frameworks for energy storage and conversion.* Energy Storage Materials, 2016. **2**: p. 35-62.
26. Wang, H., et al., *Metal-Organic Frameworks for Energy Applications.* Chem, 2017. **2**(1): p. 52-80.
27. Maiti, S., et al., *Cu 3 (1,3,5-benzenetricarboxylate) 2 metal-organic framework: A promising anode material for lithium-ion battery.* Microporous and Mesoporous Materials, 2016. **226**: p. 353-359.
28. Kim, A.Y., et al., *One-Step Catalytic Synthesis of CuO/Cu2O in a Graphitized Porous C Matrix Derived from the Cu-Based Metal-Organic Framework for Li- and Na-Ion Batteries.* ACS Appl Mater Interfaces, 2016. **8**(30): p. 19514-23.
29. Ji, D., et al., *Facile fabrication of MOF-derived octahedral CuO wrapped 3D graphene network as binder-free anode for high performance lithium-ion batteries.* Chemical Engineering Journal, 2017. **313**: p. 1623-1632.
30. Yan, X., et al., *Porous carbons prepared by direct carbonization of MOFs for supercapacitors.* Applied Surface Science, 2014. **308**: p. 306-310.
31. Wang, L., et al., *Metal–organic frameworks for energy storage: Batteries and supercapacitors.* Coordination Chemistry Reviews, 2016. **307**: p. 361-381.
32. Khan, I.A., et al., *A copper based metal-organic framework as single source for the synthesis of electrode materials for high-performance supercapacitors and glucose sensing applications.* International Journal of Hydrogen Energy, 2014. **39**(34): p. 19609-19620.
33. Ke, F.-S., Y.-S. Wu, and H. Deng, *Metal-organic frameworks for lithium ion batteries and supercapacitors.* Journal of Solid State Chemistry, 2015. **223**: p. 109-121.
34. Shoaee, M., M.W. Anderson, and M.P. Attfield, *Crystal growth of the nanoporous metal-organic framework HKUST-1 revealed by in situ atomic force microscopy.* Angew Chem Int Ed Engl, 2008. **47**(44): p. 8525-8.
35. Foley, S., et al., *Copper Sulfide (CuxS) Nanowire-in-Carbon Composites Formed from Direct Sulfurization of the Metal-Organic Framework HKUST-1 and Their Use as Li-Ion Battery Cathodes.* Advanced Functional Materials, 2018. **28**(19): p. 1800587.
36. Majano, G. and J. Pérez-Ramírez, *Scalable Room-Temperature Conversion of Copper(II) Hydroxide into HKUST-1 (Cu3(btc)2).* Advanced Materials, 2013. **25**(7): p. 1052-1057.
37. DeCoste, J.B., et al., *The effect of water adsorption on the structure of the carboxylate containing metal-organic frameworks Cu-BTC, Mg-MOF-74, and UiO-66.* Journal of Materials Chemistry A, 2013. **1**(38): p. 11922-11932.
38. Wu, R., et al., *MOFs-derived copper sulfides embedded within porous carbon octahedra for electrochemical capacitor applications.* Chemical Communications, 2015. **51**(15): p. 3109-3112.
39. Sundriyal, S., et al., *Metal-organic frameworks and their composites as efficient electrodes for supercapacitor applications.* Coordination Chemistry Reviews, 2018. **369**: p. 15-38.
40. Salunkhe, R.R., Y.V. Kaneti, and Y. Yamauchi, *Metal–Organic Framework-Derived Nanoporous Metal Oxides toward Supercapacitor Applications: Progress and Prospects.* ACS Nano, 2017. **11**(6): p. 5293-5308.
41. Cao, X., et al., *Reduced Graphene Oxide-Wrapped MoO3 Composites Prepared by Using Metal–Organic Frameworks as Precursor for All-Solid-State Flexible Supercapacitors.* Advanced Materials, 2015. **27**(32): p. 4695-4701.
42. Ji, D., et al., *Facile synthesis of a metal–organic framework-derived Mn2O3 nanowire coated three-dimensional graphene network for high-performance free-standing*

supercapacitor electrodes. Journal of Materials Chemistry A, 2016. **4**(21): p. 8283-8290.

43. Deng, X., et al., *Metal–organic frameworks-derived honeycomb-like Co3O4/three-dimensional graphene networks/Ni foam hybrid as a binder-free electrode for supercapacitors.* Journal of Alloys and Compounds, 2017. **693**: p. 16-24.
44. Xu, X., et al., *Facile Fabrication of Three-Dimensional Graphene and Metal–Organic Framework Composites and Their Derivatives for Flexible All-Solid-State Supercapacitors.* Chemistry of Materials, 2017. **29**(14): p. 6058-6065.
45. Pei, S., et al., *Direct reduction of graphene oxide films into highly conductive and flexible graphene films by hydrohalic acids.* Carbon, 2010. **48**(15): p. 4466-4474.
46. Park, S., et al., *Hydrazine-reduction of graphite- and graphene oxide.* Carbon, 2011. **49**(9): p. 3019-3023.
47. Renteria, J.D., et al., *Strongly Anisotropic Thermal Conductivity of Free-Standing Reduced Graphene Oxide Films Annealed at High Temperature.* Advanced Functional Materials, 2015. **25**(29): p. 4664-4672.
48. Tran, D.N.H., et al., *Engineered graphene–nanoparticle aerogel composites for efficient removal of phosphate from water.* Journal of Materials Chemistry A, 2015. **3**(13): p. 6844-6852.
49. Moussa, M., et al., *Recent progress and performance evaluation for polyaniline/graphene nanocomposites as supercapacitor electrodes.* Nanotechnology, 2016. **27**(44): p. 442001.
50. Mao, J., et al., *Electrocatalytic four-electron reduction of oxygen with Copper (II)-based metal-organic frameworks*. Vol. 19. 2012. 29–31.
51. Majano, G., et al., *Solvent-Mediated Reconstruction of the Metal-Organic Framework HKUST-1 (Cu3(BTC)2).* Advanced Functional Materials, 2014. **24**(25): p. 3855-3865.
52. Chui, S.S.Y., et al., *A chemically functionalizable nanoporous material Cu-3(TMA)(2)(H2O)(3) (n).* Science, 1999. **283**(5405): p. 1148-1150.
53. Alvarez, J.R., et al., *Structure stability of HKUST-1 towards water and ethanol and their effect on its CO2 capture properties.* Dalton Transactions, 2017. **46**(28): p. 9192-9200.
54. El-Kady, M.F., et al., *Laser Scribing of High-Performance and Flexible Graphene-Based Electrochemical Capacitors.* Science, 2012. **335**(6074): p. 1326-1330.
55. El-Kady, M.F. and R.B. Kaner, *Scalable fabrication of high-power graphene micro-supercapacitors for flexible and on-chip energy storage.* Nature Communications, 2013. **4**: p. 1475.
56. Tran, D.N.H., S. Kabiri, and D. Losic, *A green approach for the reduction of graphene oxide nanosheets using non-aromatic amino acids.* Carbon, 2014. **76**: p. 193-202.
57. Alotaibi, F., et al., *Scanning atmospheric plasma for ultrafast reduction of graphene oxide and fabrication of highly conductive graphene films and patterns.* Carbon, 2018. **127**: p. 113-121.
58. Khan, Q.A., et al., *Characterization of reduced graphene oxide produced through a modified Hoffman method.* Cogent Chemistry, 2017. **3**(1).
59. Kudin, K.N., et al., *Raman Spectra of Graphite Oxide and Functionalized Graphene Sheets.* Nano Letters, 2008. **8**(1): p. 36-41.
60. Dubal, D.P., et al., *Fabrication of copper oxide multilayer nanosheets for supercapacitor application.* Journal of Alloys and Compounds, 2010. **492**(1-2): p. 26-30.
61. Yu, F., et al., *High performance all-solid-state symmetric supercapacitor based on porous carbon made from a metal-organic framework compound.* Journal of Power Sources, 2017. **364**: p. 9-15.
62. Wu, M.-S. and W.-H. Hsu, *Nickel nanoparticles embedded in partially graphitic porous carbon fabricated by direct carbonization of nickel-organic framework for high-performance supercapacitors.* Journal of Power Sources, 2015. **274**: p. 1055-1062.

63. Maiti, S., A. Pramanik, and S. Mahanty, *Extraordinarily high pseudocapacitance of metal organic framework derived nanostructured cerium oxide.* Chemical Communications, 2014. **50**(79): p. 11717-11720.
64. Liu, Y., et al., *Flexible and Binder-Free Hierarchical Porous Carbon Film for Supercapacitor Electrodes Derived from MOFs/CNT.* ACS Applied Materials & Interfaces, 2017. **9**(16): p. 14043-14050.
65. Cao, X., et al., *Reduced graphene oxide-wrapped MoO3 composites prepared by using metal-organic frameworks as precursor for all-solid-state flexible supercapacitors.* Adv Mater, 2015. **27**(32): p. 4695-701.
66. Ullah, S., et al., *A novel Cr2O3-carbon composite as a high performance pseudo-capacitor electrode material.* Electrochimica Acta, 2015. **171**: p. 142-149.
67. Zhang, Y.-Z., et al., *Porous hollow Co3O4 with rhombic dodecahedral structures for high-performance supercapacitors.* Nanoscale, 2014. **6**(23): p. 14354-14359.

Chapter 4. Synthesis and characterisation of GQDs and HKUST-1@GQDs nanocomposites

This chapter reports the synthesis of GQDs and the nanocomposites made of GQDs and HKUST-1 microrods, followed by their characterisations. Firstly, the GQDs were successfully synthesised by the ultrasonic shearing method, and the nanocomposites of HKUST-1@GQDs were fabricated by the grinding approach. To investigate the particle size characteristic and the optical properties of GQDs and the nanocomposites, Nanosight measurement, PL and UV-Vis spectrometers were used. The results show that the smallest lateral dimension of GQDs ranges from 30 to 50 nm, which are produced after 15 hours of sonication. By combining with HKUST-1 microrods the nanocomposite material exhibits a higher PL intensity compared to that of GQDs only. The results suggest that the fabricated nanocomposites are potential to use for diverse optical applications, including photoluminescent sensors.

4.1. Introduction

GQDs (GOQDs) have recently attracted significant interests as an ideal material for optical sensing applications owing to their quantum confinements and edge effects [1]. These materials have been employed as the sensing probes for detection of substances and bioimaging purposes with immense advantages. For instance, Ananthanarayanan *et al.* reported the GQDs with ~3 nm in diameter produced from 3D graphene, which specifically enabled to detect iron (III) ions (Fe^{3+}) [1]. Tam *et al.* synthesised N-doped GQDs as the sensing probe of the fluorescent sensor for Fe^{3+} detection, which exhibits the enhancement of the quantum yield (QY) of 30.7% in comparison with blue GQDs [2]. Cu^{2+} ions were detected in the range of 0-15 μM by GQDs with a high sensitivity of 0.226 μM [3]. Sun *et al.* functionalized GQDs with amino groups to enhance the QY from 2.5 % to 16.4 %, and these functionalized GQDs were employed as the highly selective sensor for Cu^{2+} ions [4]. Furthermore, GQDs were used to detect and monitor other substances such as blood glucose [5, 6], phosphate [7], protein kinase [8]. It is found that the higher QY of GQDs and higher selectivity of the sensors were only achieved by modification and functionalization of GQDs.

MOF materials are suitable for sensing applications, especially optical sensors because of their high porosity, huge surface area (up to 7,000 m^2/g) [9] and complex functionalities [10]. These optical sensors are based on the luminescent and fluorescent emission of MOF materials which are attractive to academia as well as industries. Chen *et al.* reported the luminescent MOF for detecting anions (Cl^-, F^-, Br^- etc.) [11]. Chen *et al.* produced luminescence by opening the metal sites of MOFs for detection of small molecules [12]. Gole *et al.* reported the fluorescent Zn-based MOF material for detecting nitroaromatic explosives [13], etc.

Up to date, the cooperation of GQD and MOFs into nanocomposites for optical sensors (fluorescent, luminescent or even photoluminescent sensors) has not been investigated. With the unique structure and excellent properties of GQDs and MOFs, they are possibly combined to form a newly desired nanocomposite with various functionalities and complex structures, which can exhibit outstanding optical properties for many sensing applications.

As the second objective of the thesis, the chapter aims to prepare the nanocomposite made of GQDs and HKUST-1, followed by characterisation of their optical properties, and then explore their potentials for optical sensing applications. However, due to the

limited time frame of the Master of Philosophy, this work has just focused on the preparation and conducted several typical characterisations, including PL and UV-Vis, for studying optical properties. Further development of the nanocomposites and fabrication of sensing devices are considered as the potential future work.

4.2 Experimental

4.2.1 Preparation of GQD-HKUST-1 nanocomposites

10 mg of HKUST-1 was mixed with 1.0 mL of as-received GQDs (1mg/mL), which was prepared by 15 h sonicating in aqueous solution, in an agate mortar. The mixture was then ground for 20 min, followed by adding 10 mL of Milli-Q water to obtain the solution with the concentration of ~1.0 mg/mL.

4.2.2 PL characterisation

The PL spectrometer (Fluoromax-4, Horriba, Jobin Yvon) was used for characterising the excitation, and emission spectra with the wavelength ranged from 200 to 800 nm. The optimised emission peaks were determined by investigating scanning the commonly wide range of excitation wavelength. The samples were prepared the same as those of UV-Vis measurement. The PL of blank solvent suspension was completed before those of the samples were measured. The angle between the detector and the incident light source is 90 degree.

4.2.3 Nano sight measurement

The Nano sight measurement was also used to measure the particle size and their size distribution of GQDs. QGDs samples were prepared by sonicating for 1 h and diluting from 100 to 200 times to obtain the 0.005-0.01 mg/mL solution of QGDs.

4.3 Results and Discussions

4.3.1 Characterisation of prepared GQDs

Figure 4.1 shows the particle size distribution of GQDs with respect to the sonicating time and their 3D images of GQDs at different sonication times**.** The particle size distribution of GQDs after 5 h sonicating exhibit the dominant sizes of ~105, 155 nm,

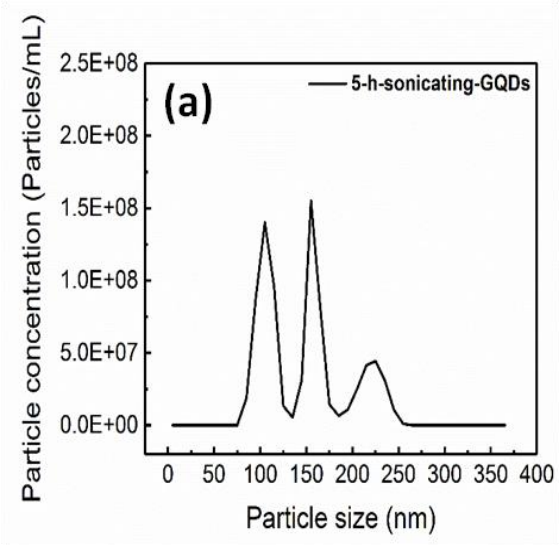
(a)
5-h-sonicating-GQDs
Particle concentration (Particles/mL)
2.5E+08
2.0E+08
1.5E+08
1.0E+08
5.0E+07
0.0E+00
0 50 100 150 200 250 300 350 400
Particle size (nm)

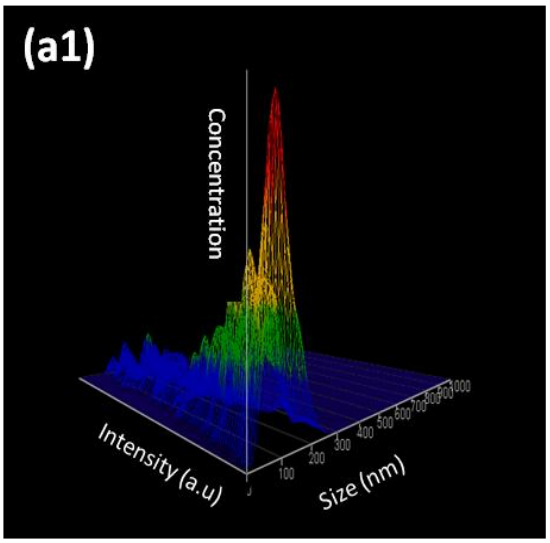
(a1)
Concentration
Intensity (a.u)
Size (nm)

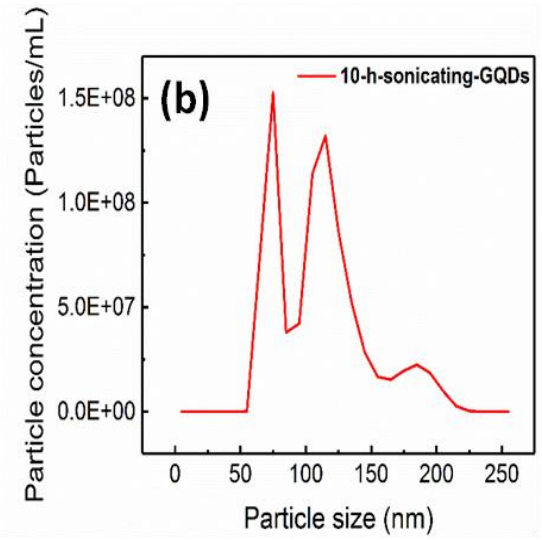
(b)
10-h-sonicating-GQDs
Particle concentration (Particles/mL)
1.5E+08
1.0E+08
5.0E+07
0.0E+00
0 50 100 150 200 250
Particle size (nm)

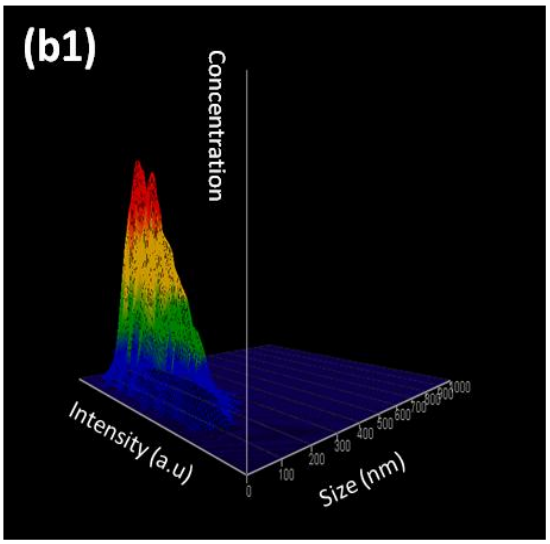
(b1)
Concentration
Intensity (a.u)
Size (nm)

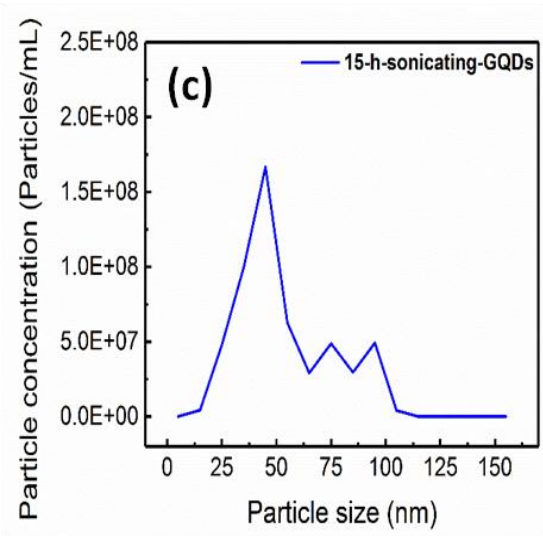
(c)
15-h-sonicating-GQDs
Particle concentration (Particles/mL)
2.5E+08
2.0E+08
1.5E+08
1.0E+08
5.0E+07
0.0E+00
0 25 50 75 100 125 150
Particle size (nm)

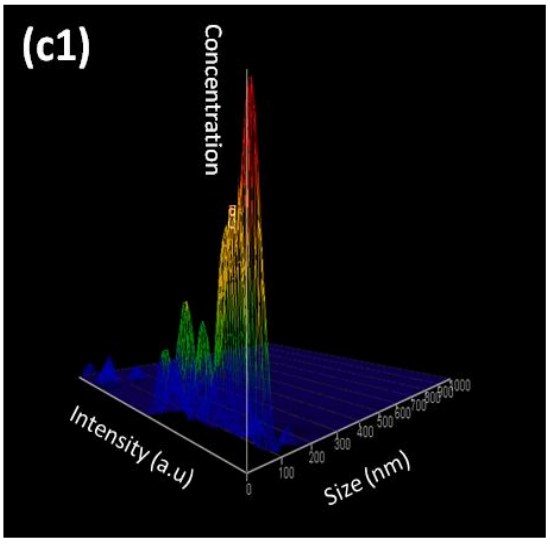
(c1)
Concentration
Intensity (a.u)
Size (nm)

Figure 4.1 Particle size distributions for different sonicating times (a) 5 h, (b) 10 h, and (c) 15 h, and their 3D images (a1), (b1), and (c1), respectively.

as shown in Figure 4.1 a and a1. For the GQDs with 10 h of sonication, the distribution of particle sizes is mainly at ~75 and ~115 nm, with a higher concentration at 75 nm (Figure 4.1b and b1). When the sonicating time reached 15 h, the most common size of GQDs shows homogenous particles with a size of approximately 50 nm (Figure 4.1c and c1).

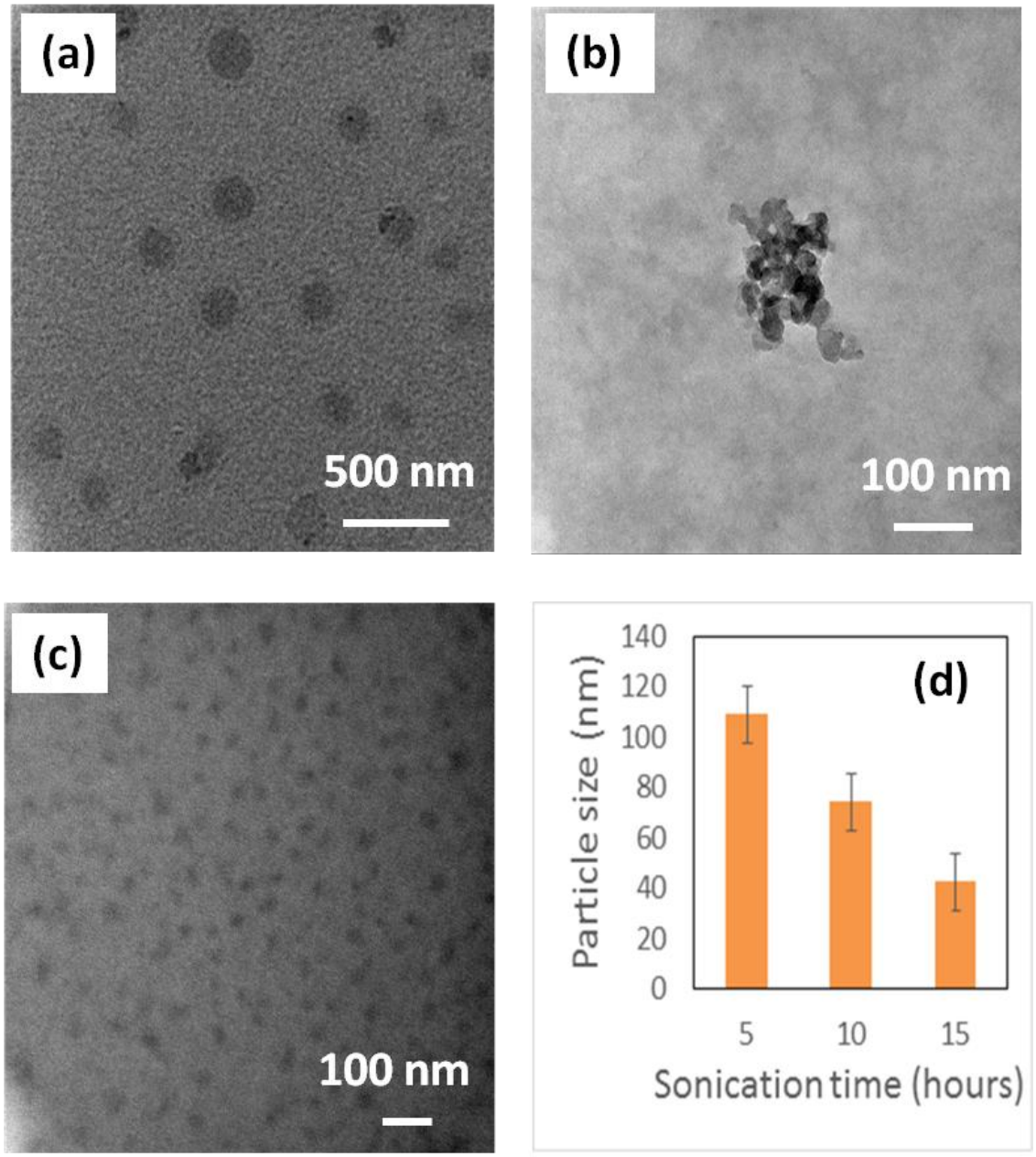

Figure 4.2 TEM images of GQDs at 5 h (a), 10 h (b), and 15 h (c) sonicating, and the relationship between the particle sizes of GQDs vs sonication time.

The TEM images display that after 5 h, 10 h, and 15 h sonicating the diameters of GQDs are in the range of 100-120, 65-85, and 30-50 nm, respectively, as shown in Figure 4.2a, b, and c. These results are relatively consistent with those from Nanosight measurement, which are shown in Figure 4.2d. In water medium, the low-pressure and high-pressure waves are possibly generated from ultrasound, which causes high-speed impinging liquid jets, deagglomeration, and strong hydrodynamic shear forces [14]. The energy from the ultrasonic source then cut graphene sheets into GQDs. During the cutting process of graphene sheets, tiny particles with a protrudent edge are formed [14]; therefore, most of GQDs with their circle-like shapes are formed, which can be seen from Figure 4.2. For a longer time of sonication, the diameters of QGDs become smaller since there is more energy from the ultrasonic source consumed to cut graphene sheets. Besides, it also shows the nearly linear relationship between the sonication time and particle size of GQDs as denoted in Figure 4.2d.

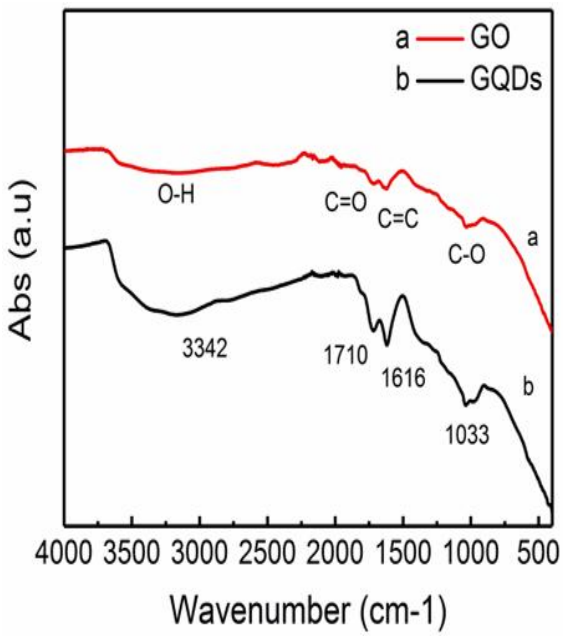

Figure 4.3 FTIR spectra of GO and GQDs

Figure 4.3 shows the FTIR of GO and GQDs, in which the oxygen functional grounds including O-H, C=O, C=C, C-O still exist on their structures, indicating that there has been no reduction of GQDs because the temperature is kept at less than 40ºC during the sonicating process. The broad band at 3342 cm^{-1} is due to the stretch vibration of O-H groups. The stretching of C=O and C-O groups are at 1710 and 1033 cm^{-1}, respectively, while the band occurring at 1616 cm^{-1} is assigned to the stretch of C=C groups.

4.3.2 Characterisation of GQD-HKUST-1 nanocomposite

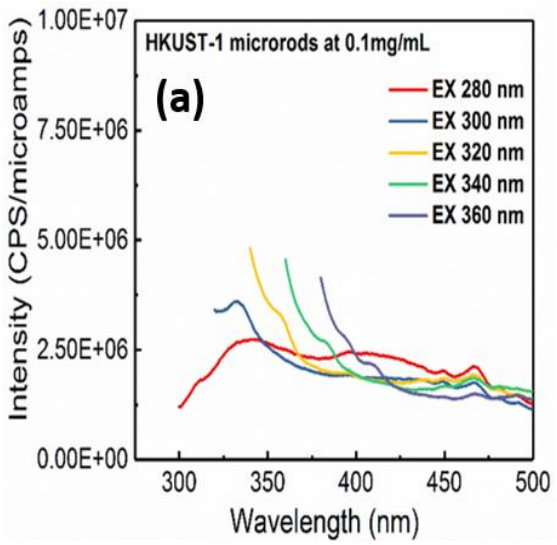

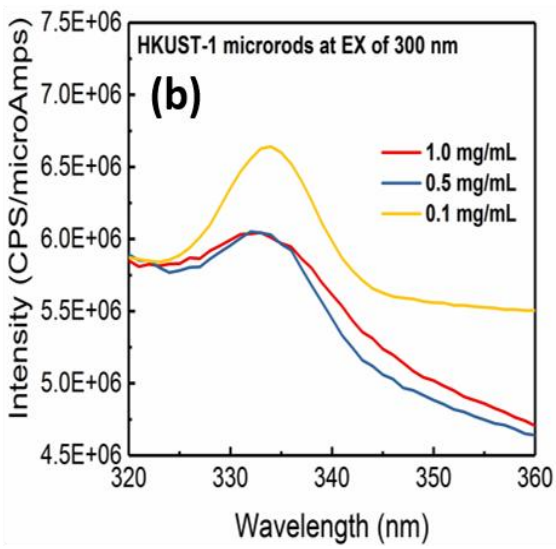

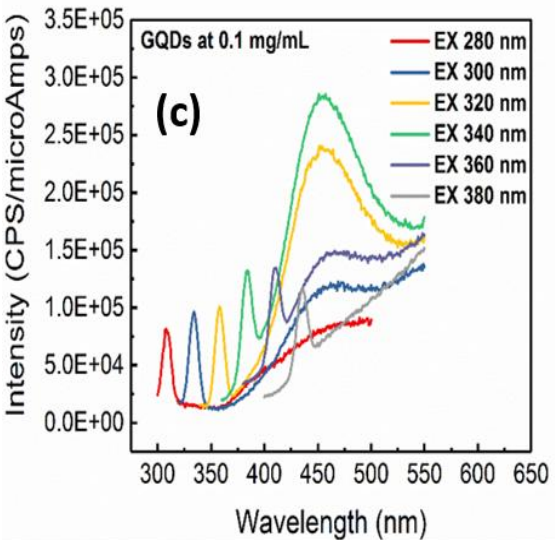

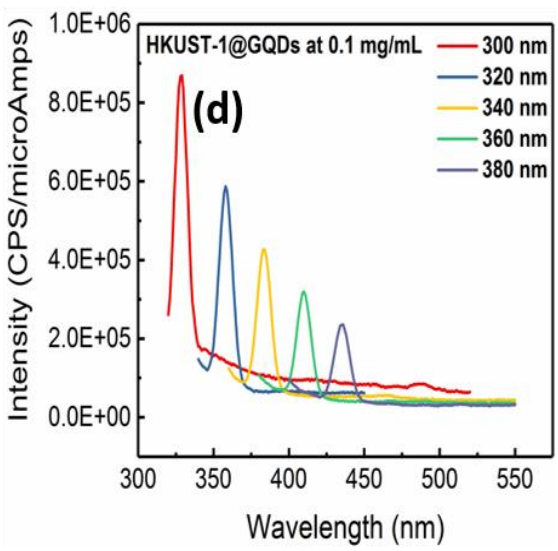

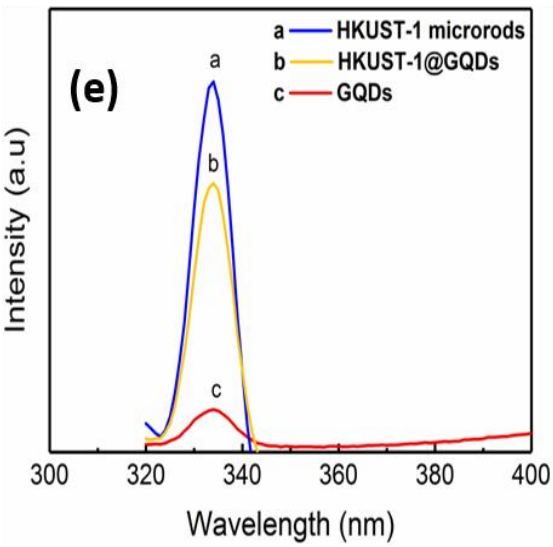

Figure 4.4 PL spectra of GQDs, HKUST-1 microrods @10%wt GQDs, and HKUST-1 microrods at the EX wavelength of 300 nm and concentration of 0.1 mg/mL.

Figure 4.4 shows the PL spectra of GQDs, HKUST-1 microrods, and HKUST-1@GQDs nanocomposites. To optimise the emission (EM) spectra, the HKUST-1 was excited at different excitation (EX) wavelengths ranging from 280 to 360 nm (Figure 4.4a). The EM spectra peaked at the EX of 300 nm and to optimise the concentration of materials, HKUST-1 microrods were excited at the EX 300 nm for different concentrations of 0.1, 0.5 and 1 mg/mL. The results show that the concentration of 0.1 mg/mL is the optimum value, as shown in Figure 4.4b. GQDs with oxygen functional groups in their structures are well-dispersed in water. The PL properties are strongly dependent on the size of GQDs; however, in this study, only GQDs with 15 h of sonication are used because of their smallest sizes. Figure 4.4c shows the PL spectra of 0.1 mg/mL GQD solution excited in the range of wavelength from 280 to 380 nm. GQDs exhibit varying light absorption behaviours with the excitation-dependent PL [15] and excitation-independent PL [16].

All the PL spectra of GQDs are excitation-dependent, shifting from ~307 to ~435 nm corresponding to the EX range, and another spectrum absorbed at ~455 nm strongly increases with the increment of the EX wavelength until 340 nm as shown in Figure 4.4c. The spectra of 0.1 mg/mL HKUST-1@GQDs show a strong absorption peak at 334 nm corresponding to the EX of 300 nm, followed by the spectra at the EX of 320 nm. When the EX wavelength increases, the intensities of the spectra decrease significantly as observed in Figure 4.4d. Figure 4.4e compares the spectra of three materials, including GQDs, HKUST-1 microrods and HKUST-1@GQDs nanocomposites at the EX wavelength of 300 nm. The results show that HKUST-1 microrods exhibit the highest intensity, followed by HKUST-1@GQDs, while the GQDs shows the lowest PL figure, which is much lower than that of HKUST-1s. This high PL of HKUST1s can be understood by the investigation of their photoluminescent property that is attributable to luminescent emission of powder azobenzene molecule due to Cu(II) in HKUST-1, which can quench the luminescence of the host framework [17]. Meanwhile, the GQDs possess a graphene core and attached oxygen-containing functional groups which control the PL, and the bandgap of the conjugated domains is thought to be the true intrinsic PL centre [18]. Furthermore, the GQDs' size plays also a

crucial role which dominates the quantum confinement effect (QCE). HKUST-1@GQDs nanocomposites with the PL intensity lying between those of HKUST-1s and GQDs can be explained to be due to the effect of the attachment of GQDs onto HKUST-1 microrods'surface. These findings indicate that HKUST-1 microrods enhanced the PL intensity of GQDs substantially.

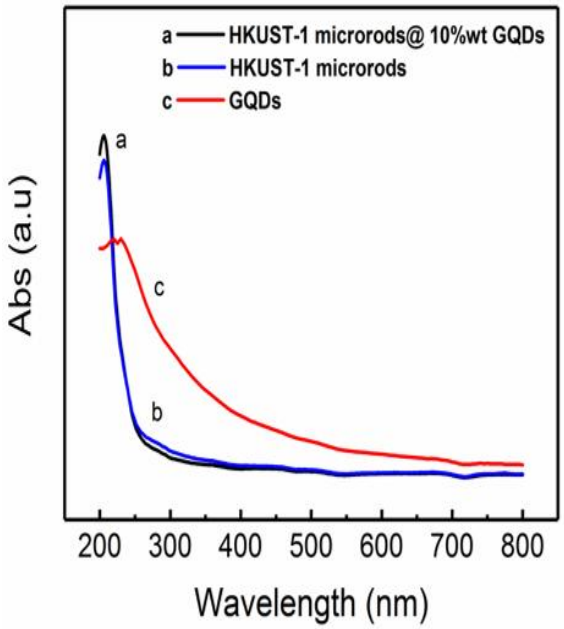

Figure 4.5 UV-Vis spectra of GQDs, HKUST-1 microrods @10%wt GQDs, and HKUST-1 microrods at a concentration of 0.1 mg/mL.

The UV-Vis spectra show that GQDs have an absorption peak at ~230 nm, a typical characteristic of aromatic materials, which is assigned to the π-π* transition of the sp^2 domain in the structure of GQDs [19]. Meanwhile, the absorption peaks of HKUST-1 microrods and HKUST-1@GQDs are observed at a lower wavelength of ~205 nm (Figure 4.5). These UV-Vis and PL results are obtained through the measurement several times, showing a high repeatability, although they can be different from the theory of UV-Vis and PL for HKUST-1. The difference in UV-Vis and PL results between the transferred 1D microrods of HKUST-1 MOF and the raw diamond-like shape HKUST-1 MOF is perhaps due to the weak absorption of HKUST-1 microrods at the wavelenght of 300 nm. This changed optical property is related to shapes and crystallinity level of HKUST-1 MOF. However, the discrimation in these results needs to be taken into further consideration in the near future.

Although the fabricated HKUST-1@GQDs nanocomposites have considerable advantages to apply for PL sensing application, further characterisations should be carried out as the future work to confirm the feasibility of these materials for practical applications.

Conclusion

GQDs, HKUST-1@ GQD nanocomposites were successfully synthesised, followed by their characterisation of the morphologies, structures, and the optical properties. The TEM images of GQDs indicate that the sizes of GQDs decrease from 100-120 nm to 30-50 nm in diameter as the sonication time increases from 5h to 15h. FTIR spectrum of GQDs confirms the existence of the functional groups on the structure of GQDs. The PL and UV-Vis spectra of GQDs, HKUST-1, and HKUST-1@GQDs nanocomposites show that HKUST-1@QGDs can be used as the PL sensing probes. The further characterisation should be carried out to investigate the PL properties of the nanocomposites and explore their potential for sensing applications.

References

1. Ananthanarayanan, A., et al., *Facile Synthesis of Graphene Quantum Dots from 3D Graphene and their Application for Fe3+Sensing.* Advanced Functional Materials, 2014. **24**(20): p. 3021-3026.
2. Tam, T.V., et al., *One-pot synthesis of N-doped graphene quantum dots as a fluorescent sensing platform for Fe3+ ions detection.* Sensors and Actuators B: Chemical, 2014. **202**: p. 568-573.
3. Wang, F., et al., *Graphene quantum dots as a fluorescent sensing platform for highly efficient detection of copper(II) ions.* Sensors and Actuators B: Chemical, 2014. **190**: p. 516-522.
4. Sun, H., et al., *Highly photoluminescent amino-functionalized graphene quantum dots used for sensing copper ions.* Chemistry, 2013. **19**(40): p. 13362-8.
5. He, Y., et al., *Fluorescent blood glucose monitor by hemin-functionalized graphene quantum dots based sensing system.* Analytica Chimica Acta, 2014. **810**: p. 71-78.
6. Zhang, L., et al., *Boron-Doped Graphene Quantum Dots for Selective Glucose Sensing Based on the "Abnormal" Aggregation-Induced Photoluminescence Enhancement.* Analytical Chemistry, 2014. **86**(9): p. 4423-4430.
7. Bai, J.M., et al., *Graphene quantum dots combined with europium ions as photoluminescent probes for phosphate sensing.* Chemistry, 2013. **19**(12): p. 3822-6.
8. Wang, Y., et al., *Using Graphene Quantum Dots as Photoluminescent Probes for Protein Kinase Sensing.* Analytical Chemistry, 2013. **85**(19): p. 9148-9155.
9. Ke, F.-S., Y.-S. Wu, and H. Deng, *Metal-organic frameworks for lithium ion batteries and supercapacitors.* Journal of Solid State Chemistry, 2015. **223**: p. 109-121.
10. Kreno, L.E., et al., *Metal–Organic Framework Materials as Chemical Sensors.* Chemical Reviews, 2012. **112**(2): p. 1105-1125.
11. Chen, B., et al., *A Luminescent Microporous Metal−Organic Framework for the Recognition and Sensing of Anions.* Journal of the American Chemical Society, 2008. **130**(21): p. 6718-6719.
12. Chen, B., et al., *Luminescent Open Metal Sites within a Metal–Organic Framework for Sensing Small Molecules.* Advanced Materials, 2007. **19**(13): p. 1693-1696.
13. Gole, B., A.K. Bar, and P.S. Mukherjee, *Fluorescent metal–organic framework for selective sensing of nitroaromatic explosives.* Chemical Communications, 2011. **47**(44): p. 12137-12139.
14. Zhuo, S., M. Shao, and S.-T. Lee, *Upconversion and downconversion fluorescent graphene quantum dots: ultrasonic preparation and photocatalysis.* ACS nano, 2012. **6**(2): p. 1059-1064.

15. Gan, Z., H. Xu, and Y. Hao, *Mechanism for excitation-dependent photoluminescence from graphene quantum dots and other graphene oxide derivates: consensus, debates and challenges.* Nanoscale, 2016. **8**(15): p. 7794-7807.
16. Sarkar, S., et al., *Graphene quantum dots from graphite by liquid exfoliation showing excitation-independent emission, fluorescence upconversion and delayed fluorescence.* Physical Chemistry Chemical Physics, 2016. **18**(31): p. 21278-21287.
17. Fu, W.-Q., et al., *Liquid Phase Epitaxial Growth and Optical Properties of Photochromic Guest-Encapsulated MOF Thin Film.* Crystal Growth & Design, 2016. **16**(9): p. 5487-5492.
18. Zhu, S., et al., *Photoluminescence mechanism in graphene quantum dots: Quantum confinement effect and surface/edge state.* Nano Today, 2017. **13**: p. 10-14.
19. Zhu, X., et al., *Hydrothermal Preparation of Photoluminescent Graphene Quantum Dots Characterized Excitation-Independent Emission and its Application as a Bioimaging Reagent.* Particle & Particle Systems Characterization, 2014. **31**(7): p. 801-809.

Chapter 5. Graphene-MOF nanocomposites for chemical vapour sensors

This chapter reports the results achieved in synthesising and characterising pG-MOF nanocomposites and possibly using them as sensing materials for chemical vapour sensors. High-quality pG material is prepared via the solvent exfoliation method, and the pG-MOF nanocomposites were synthesised by blending with the aid of a shear mixing method. The sensing devices were successfully fabricated by spray coating pG-MOF dispersion on interdigitated electrodes, followed by their characterisations. The results show that the fabricated sensors exhibit sensing responses and discriminations to the organic vapours such as acetone, ethanol, methanol and chloroform. These findings suggest the pG–MOF nanocomposites could be used as a chemical sensing platform for volatile organic compounds (VOCs) detection.

Journal paper in preparation

Chemoresistive Sensors made of Graphene and Metal-Organic Framework Composites for VOC Biomarkers Analysis.

Tran Thanh Tung[1], Manh Trung Tran[2], Mickaël Castro[2], Jean-François Feller[2]*, Truc Van Ngo[1], Kamrul Hassan[1], Campbell J Coghlan[1], Md. J. Nine[1], Dusan Losic[1]*.

[1] *School of Chemical Engineering, University of Adelaide, Adelaide, Australia*

[2] *Smart Plastics Group, Bretagne Loire University (UBL), IRDL CNRS 6027 – UBS, Lorient, France.*

Corresponding: Prof Dusan Losic¸ School of Chemical Engineering, University of Adelaide, Adelaide 5005 SA, Australia; and Prof. Jean-François Feller, Bretagne Loire University (UBL), IRDL CNRS 6027 –UBS, Lorient, France.

Corresponding author*

E-mail address: dusan.losic@adelaide.edu.au

Manuscript paper is preparing for submission in Sensor and Actuator B, 2019 (Elsevier).

5.1 Introduction

MOF materials, with their high pore volume, surface area, and functionalities on their structures, uniform channels, nanosize cavities [1], have emerged as the promising candidates for gas/vapour sensing devices. Lu *et al.* reported the ZIF-8 MOF as a selective sensing probe for detecting chemical vapours and gases [1]. Kreno *et al.* fabricated the HKUST-1 MOF thin film for enhancement of gas sensor [2]. Dou *et al.* fabricated luminescent MIL-100 (In) MOF as a gas sensor for detecting oxygen with high selectivity and fast response [3]. The work conducted by Koo *et al.* reported a complex structure of Pd@ZnO-WO_3 for detection of chemical gases with a quick response [4].

Graphene is an ideal material for the gas sensor due to its large surface area, and its planar geometry, excellent conductivity with a small bandgap [5], allowing it to detect the gas molecules. Schedin *et al.* reported the graphene sensor device which can detect individual gases of NO_2, NH_3, H_2O and CO [6]. Rumyantsev *et al.* fabricated a transistor made of single pristine graphene to selectively detect chemical vapours, for example, ethanol and methanol [7]. Chen *et al.* fabricated the pG sensor with a supersensitivity for detection of common gases [8]. Another work conducted by Paul *et al.* used graphene nanomesh as the gas sensing device, which exhibited a high sensitivity with NH_3 and NO_2 [9].

Although MOF-based material and graphene for gas sensors demonstrated a significant contribution to the development of gas sensing field, there has been a limited number of publications on the combination of pG-MOF material and its potential applications for gas/vapour sensing platform.

This chapter focuses on designing new nanocomposites made of graphene and three different types of MOFs (HKUST-1, ZIF-8, and UiO-66) for chemical vapour sensors that corresponds to the third objective of the thesis. The morphology and crystallinity of nanocomposites were characterised by using SEM, TEM, and XRD. The sensing characterisation was carried by a collaborated partner, the CNRS 6027, UBS, Lorient, France. The content of this chapter will be partly used to write a research paper with sharing authorship.

5.2 Experimental

5.2.1 Materials

Zinc carbonate basic ($[ZnCO_3]_2 \cdot [Zn(OH)2]_3$, Sigma Aldrich), 2-methylimidazole ($C_4H_6N_2$, Aldrich, 99%), zirconium chloride ($ZrCl_4$, 99.5%; Aldrich), 1,4-benzenedicarboxylate (H2BDC, 98%; Aldrich), N,N-dimethylformamide ($HCON(CH_3)_2$, DMF, 99.8%; Sigma-Aldrich), methanol (CH_3OH, 99.5%; Sigma-Aldrich) were used directly without further purification.

5.2.2 Preparation of UiO-66 MOF

The UiO-66 synthesis was carried out, following the previously reported study [10]. Briefly, 58.4 mg of $ZrCl_4$ and 41.5 mg of H_2BDC were dispersed in DMF (22mg) and then sonicated for 5 min before they were transferred to a vessel. The vessel was sealed and placed in a water bath at the temperature of 50-55.5ºC for 3 days. The product was cooled, filtered and then washed with DMF.

5.2.3 Preparation of ZIF-8 MOF

The ZIF-8 MOF was synthesised, following the previously reported study [11]. Briefly, 2.8 mmol of zinc carbonate basic was dissolved in 1.4 mol of methanol in one round-bottom flask. Next, 64.4 mmol of 2-methylimidazole ($C_4H_6N_2$) and 1.4 mol of methanol were added to the solution and vigorously stirred for different times. The resulting solution was centrifuged at 3000 rpm and washed thoroughly with methanol (3 times). The product was dried at 120ºC overnight.

5.2.4 Preparation of pG-MOF nanocomposites

Three nanocomposite materials based on pG and MOFs were prepared by using shear mixing method. 50 mg of pG and 30 mg of each HKUST-1, ZIF-8, and UiO-66 in powder form are blended in a mortar and pestle for 20 min. These mixtures were then dispersed in methanol under the mild sonication for 1 h, except for the mixture of pG-HKUST-1, in which 5% HCl (5mL) was added to the mixture, and it was then dispersed in methanol before sonicating as above.

5.2.5 Fabrication of sensing devices

The fabrication of the sensing devices follows the approach in the previous reports [12, 13]. Briefly, the prepared dispersion of pG-MOF nanocomposites included G-HKUST-1, G-UiO-66, and G-ZIF-8 in methanol were sprayed onto interdigitated electrodes using the layer-by-layer method. The devices were dried carefully under the protective environment (Argon gas) and stored in a vacuum chamber.

5.2.6 Sensing characterisation

The sensing characterisation is conducted by a collaborated partner, the CNRS 6027, UBS, Lorient, France, where sensing characteristics were fully monitored and investigated as described in the previously reported study [13]. The chemo-resistive responses of the nanocomposites were recorded when the materials were exposed to the standard pure nitrogen and organic vapours. These volatile organic vapours (VOCs) such as acetone, ethanol, methanol and chloroform were used for testing at room temperature. The responses (Ar) of vapour sensors were recorded and defined by the following equation [13] :

$$A_r = \frac{R - R_0}{R_0}$$

where R and R_0 are the resistances of sensing materials when they are exposed to detected vapours and standard nitrogen, respectively.

5.3 Results and discussions

5.3.1 Morphologies and structures of nanocomposites

a. pG-HKUST-1 50/30 (G-HKUST-1 50/30) nanocomposites

Figure 5.1a-b show the morphology of G-HKUST-1 50/30 nanocomposites at different magnifications, respectively. The graphene sheets are restacked and have their typical lateral size of fewer than 15 μm, uniformly distributed in the nanocomposites. It also shows that HKUST-1 particles intercalated into graphene sheets. The TEM images also illustrate that HKUST-1 particles, with their typical diameters of~ 20-50 nm, intercalated and randomly distributed between restacked graphene sheets, confirming the successful formation of the nanocomposites. Figure 5.1d shows the high-resolution TEM image of the nanocomposite, but the structures of the HKUST-1 particles are not a high crystalline.

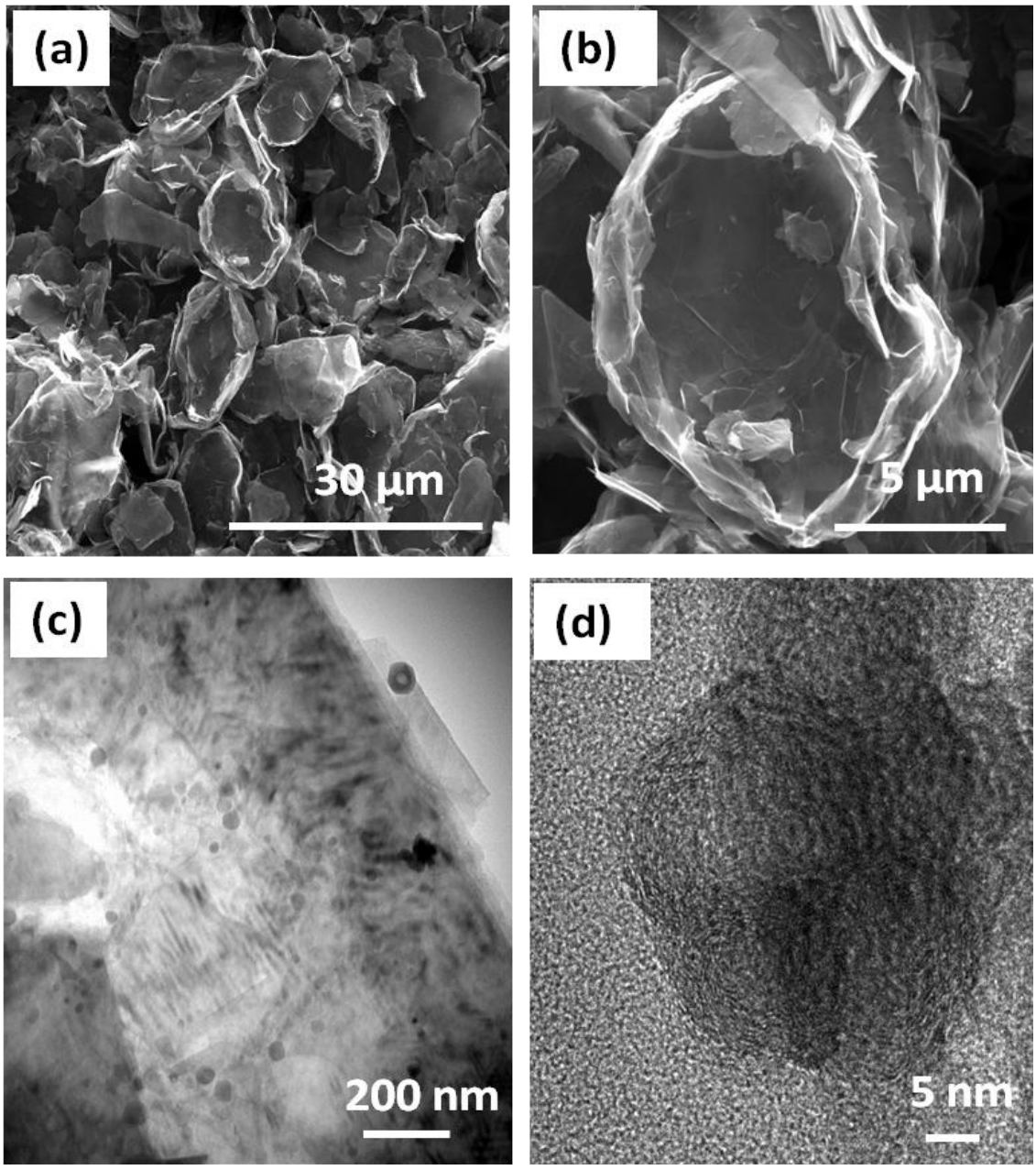

Figure 5.1 SEM images (a, b) and TEM images (c, d) of G-HKUST-1 50/30 nanocomposites.

b. pG-ZIF-8 50/30 (G-ZIF-8 50/30) nanocomposites

It is observed from Figure 5.2a-b that ZIF-8 particles were agglomerated and bounced by graphene sheets to form the G-ZiF-8 nanocomposites. TEM images also confirm the

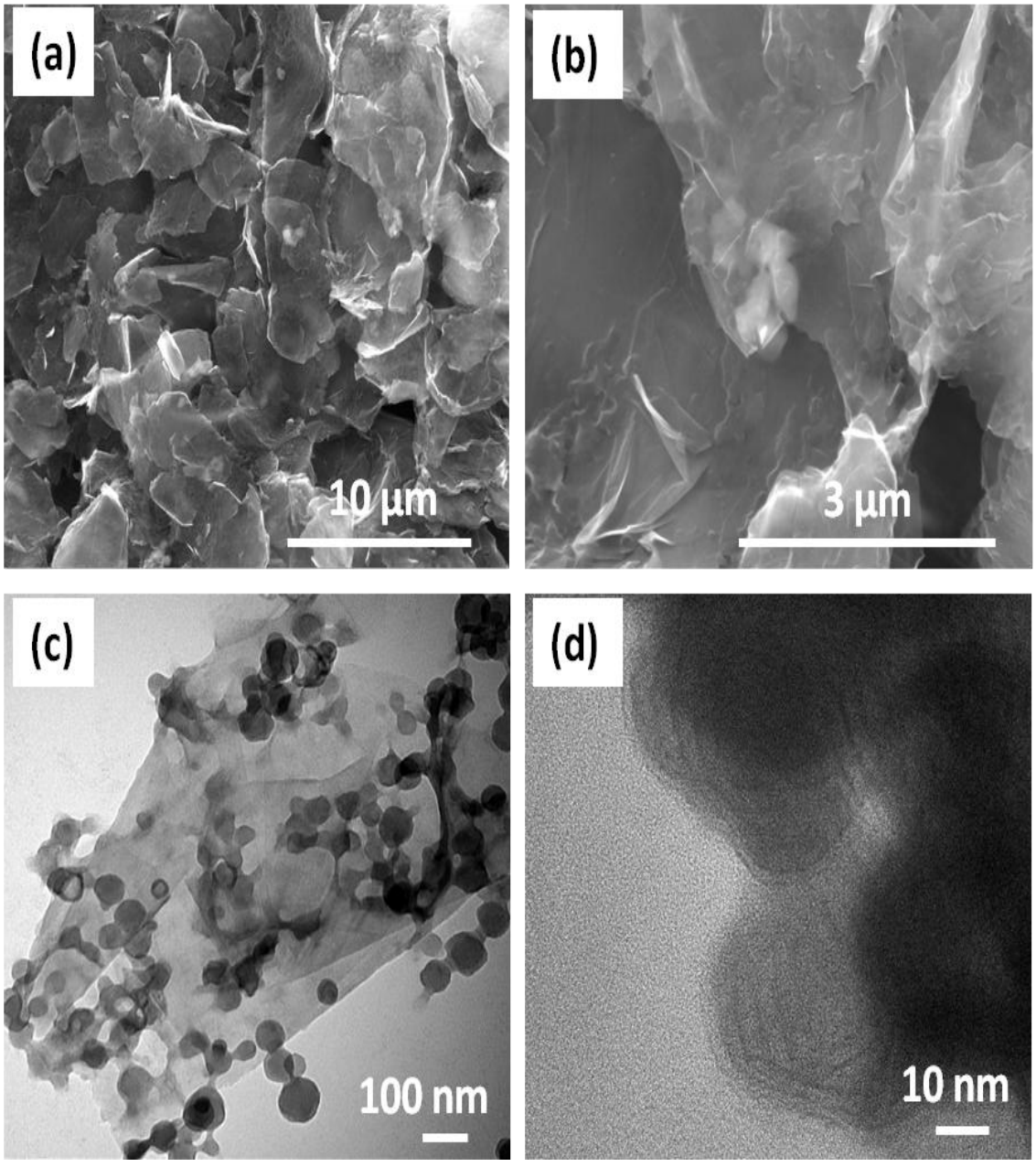

Figure 5.2 SEM images (a, b) and TEM images (c, d) of G-ZiF-8 50/30 nanocomposites.

ZIF-8 particles with their diameters of ~50-100 nm, intercalated in graphene sheets and stacked on the surface of graphene, providing more evidence of the nanocomposite formation, as in Figure 5.2c. Figure 5.2d shows the crystal feature of ZIF-8 particles at the high magnification, in which the structure of ZiF-8 particles is similar to the bunch of thin layers super-positioned together.

c. pG-UiO-66 50/30 (G-UiO-66 50/30) nanocomposites

Figure 5.3a-b show the morphologies of G-UiO-66 nanocomposites, in which UiO-66 particles with their diameters of 30-50 nm aggregated and randomly distributed onto and between graphene sheets. The evidence of the formation of the G-UiO-66 nanocomposite is further confirmed in Figure 5.3c, and a high crystallite of graphene is shown in Figure 5.3d.

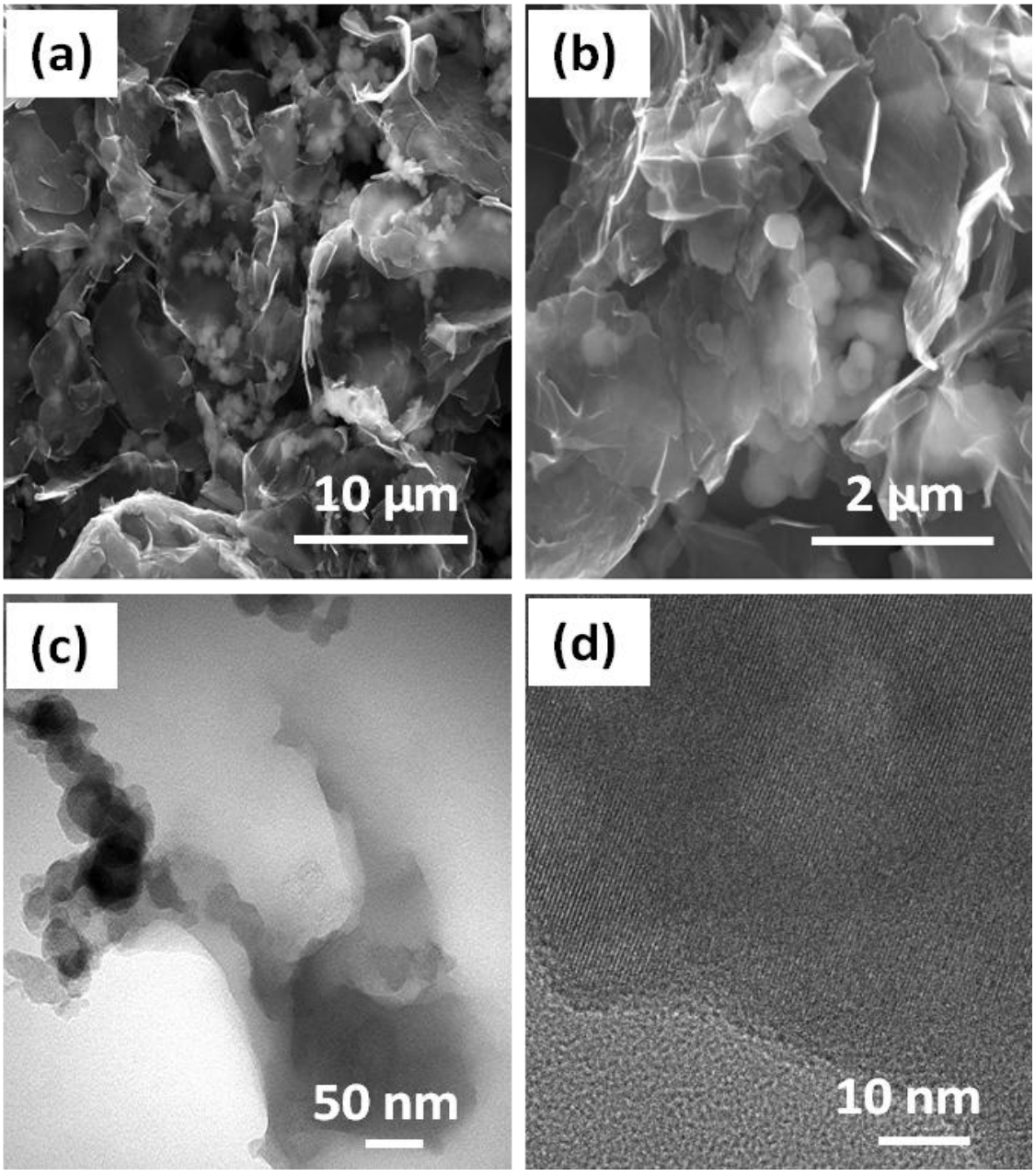

Figure 5.3 SEM images (a, b) and TEM images (c, d) of G-UiO-66 50/30 nanocomposites.

5.3.2 XRD of pG-MOF (G-MOF) nanocomposites

All XRD spectra of three nanocomposites show a sharp peak at the diffraction angle of ~27.4º, which confirms the presence of graphene in these nanocomposites as shown in Figure 5.4. When MOFs are composited with graphene to form nanocomposites, the structures of MOFs are collapsed, leading to their poor crystallinity in their nanocomposites, which are also supported by XRD.

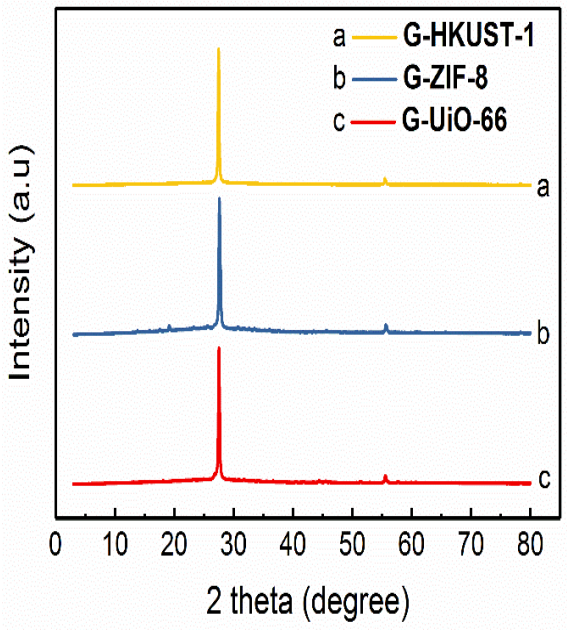

Figure 5.4 XRD spectra of three nanocomposites of (a) G-HKUST-1 50/30, (b) G-ZIF-8 50/30, and (c) G-UiO-66 50/30.

5.3.3 Sensing characterisation

From thispoint, G-Rubio and G-UiO-66 nanocomposites are interchangeably used forconveniene as they are the same materials. The performances of chemo-resistive sensors were conducted at room temperature for ethanol and acetone (100% each), in which the relative amplitude (A_r) was calculated from Equation (1) based on the recorded resistances of sensing materials. In the diagrams in Figure 5.5, the units of KOhm (or KΩ) and mOhm (or MΩ) after the sample names are the initial resistances (R) of sensor devices and they will change in different ways when they expose to the chemical vapours. These resistances are different for each sensor due to the distribution behaviors of MOFs on the graphene surface. For example, G-Cu 50/30 (G-HKUST-1) has its initial resistance of 76 KOhm, G-Rubio 50/30 has R~160 KOhm, while G-ZIF-8 50/30 has R~2.8 MOhm. Figure 5.5a compares the responses of three nanocomposites,

G-Cu 50/30 (G-HKUST-1), G-Rubio 50/30 (or G-UiO-66 50/30), and G-ZIF-8 50/30 to acetone. It is observed from the chart that all materials are sensitive to acetone. Their resistances increased with their sorption in acetone and returned to the initial state when desorption in standard nitrogen [13]. All materials exhibit the fast response and recovery (few seconds) when they are exposed to 100% acetone, and they also have high stability after 8 cycles, except for G-Rubio at the two first cycles when the sensors have not operated stably. G-Rubio shows the highest sensitivity to acetone, while G-Cu and G-ZIF-8 exhibit their much lower responses to acetone in comparison with G-Rubio. This result suggests that the high sensitivity of G-Rubio to acetone can result from the interaction between Zr sites in G-Rubio and oxygen in the acetone structure. Therefore, the sensitivities of these nanocomposites to acetone are ranked: A_r (G-Rubio 50/30 881 KΩ) > A_r (G-Cu 50/30 164 KΩ)~ A_r (G-ZIF-8 50/30 874 KΩ).

Similarly, Figure 5.5b shows the performances of chemo-resistive sensors made from the three nanocomposites to ethanol (100%). The G-Cu 50/30 nanocomposite exhibits the highest sensitivity to ethanol, followed by G-Rubio 50/30, while G-ZIF-8 50/30 is insensitive to ethanol. Hence, the sensitivities of these materials to acetone are: A_r (G-Cu 50/30) > A_r (G-Rubio 50/30) > A_r (G-ZIF-8 50/30). However, G-Cu 50/30 and G-Rubio 50/30 have a delay of the recovery time of ~400 sec before they completely desorb in nitrogen. This suggests that there are strong interactions between ethanol molecules with Cu and Zr sites, respectively.

Figure 5.5c,d show the performances of chemo-resistive sensors made from the two nanocomposites of G-Cu 50/50 (G-HKUST-1) at different resistances, and G-Rubio 50/50 (G-UiO-66) conducted at the room temperature to methanol and chloroform (100% each), respectively. The resistances of G-Cu 50/50 samples were at from 110, 145, 160 and 170 KΩ, while G-Rubio 50/50 (G-UiO-66) was at a constant value of 1.46 MΩ. It is observed that the response behaviours of G-Cu 50/50 (G-HKUST-1)-based gas sensor is dependent on the resistances of the nanocomposites.

For methanol, the highest response was the G-Cu 50/50 170 KΩ at an average A_r of 1.0, followed by G-Cu 50/50 160 KΩ, while the G-Cu 50/50 110 KΩ and G-Cu 50/50 145 KΩ showed their lowest similar response characteristics at approximately 0.2 through the whole range of testing time as shown in Figure 5.5c. The reason for this trend in the response behaviours of the G-Cu 50/50 composite to methanol can result

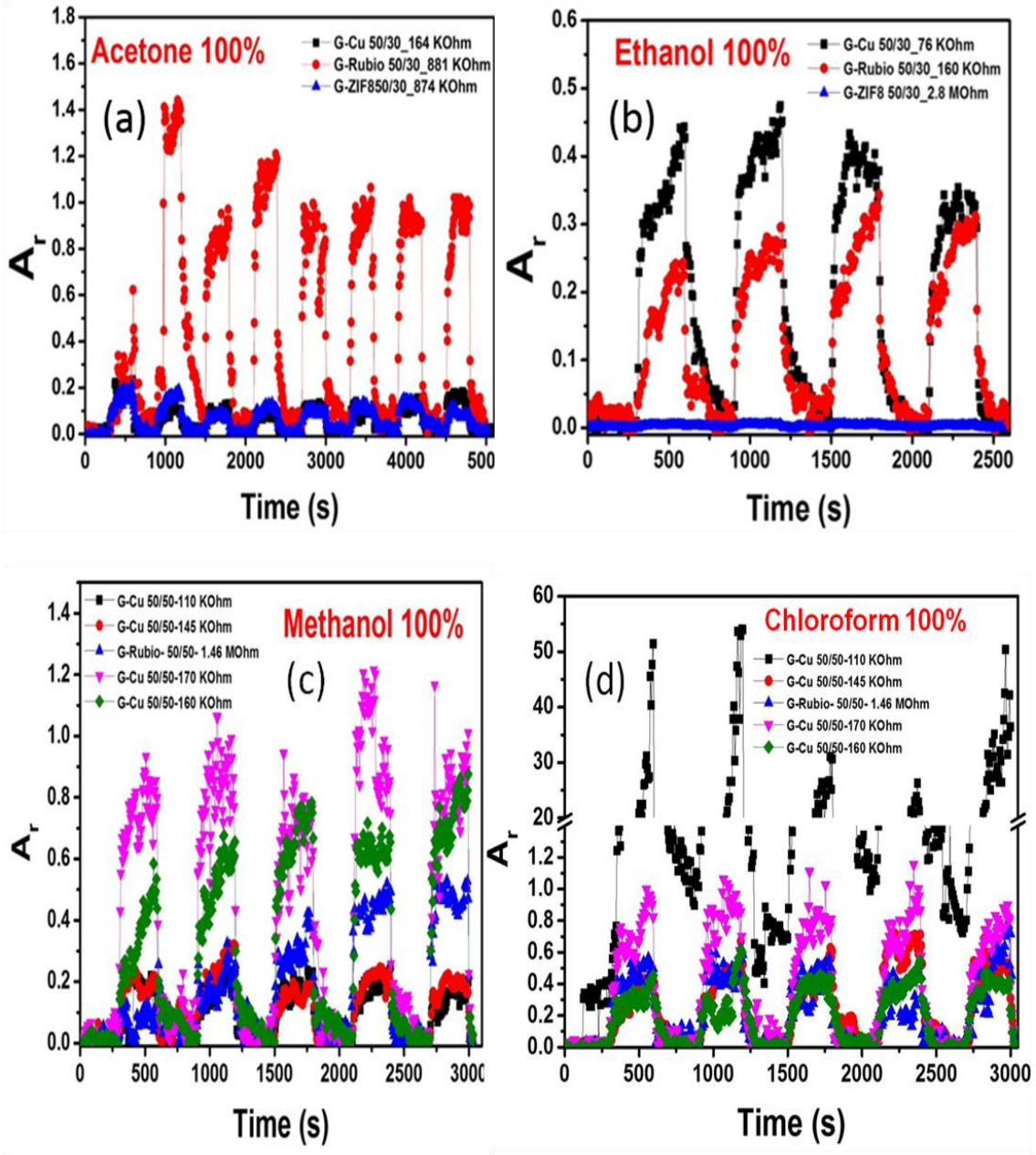

Figure 5.5 Chemo-resistive responses of G-MOF nanocomposites for VOCs: (a) acetone 100% and (b) ethanol 100%, (c) methanol 100% and (d) chloroform 100%.

from the stronger interactions between methanol molecules and Cu ion sites and holes in the structures of composites when the resistances are high, and at the resistance of fewer than 145 KΩ there is no much difference in the A_r of G-Cu 50/50 composites as can be seen from the chart. In order to compare with G-Cu 50/50, the G-Rubio 50/50 was also prepared, and its response behaviour was characterised. It is evidently shown that both G-Cu 50/50 and G-Rubio 50/50 composites have fast responses and recoveries when they are exposed to methanol (100%) in five cycles. However, G-Cu 50/50

composites exhibit relative stability in their responses even at different resistances of samples, whereas the figure for G-Rubio 50/50 increases throughout the entire period of testing up to 3000 secs. The increase in the response behaviour of G-Rubio 50/50 nanocomposite can be due to the increase in the interactive sites and holes in the structure of composites after desorption in the standard nitrogen. The response line of G-Rubio 50/50 was found lying between the response line of G-Cu 50/50 110/145 KΩ and G-Cu 50/50 160 KΩ as shown in the chart. The response lines of both G-Cu 50/50 and G-Rubio 50/50 composites show their stable repeatabilities through five cycles investigated. Therefore, the sensitivities of all these nanocomposites to methanol are ranked: A_r (G-Cu 50/50 170 KΩ) > A_r (G-Cu 50/50 160 KΩ) > A_r (G-Rubio 50/50 1.46 MΩ) > A_r (G-Cu 50/50 145 KΩ) > A_r (G-Cu 50/50 110 KΩ).

For chloroform, there was adverse response behaviour of G-Cu 50/50 nanocomposites to chloroform in comparison with methanol as in Figure 5.5d. Specifically, the highest response belonged to the G-Cu 50/50 110 KΩ at an average A_r of 40, followed by G-Cu 50/50 170 KΩ, while the G-Cu 50/50 160 KΩ and G-Cu 50/50 145 KΩ had their lowest similar response characteristics at approximately 0.5 during the entire testing time. The response figure for G-Cu 50/50 110 KΩ was significantly far higher than those of the other G-Cu 50/50 nanocomposites (at least 30 times). The reason can be due to the active interaction of Cl atoms in chloroform molecules with Cu sites and holes in the nanocomposites at a low resistance. The G-Rubio 50/50 nanocomposite shows the same response behaviours to chloroform as G-Cu 50/50 160 KΩ and G-Cu 50/50 145 KΩ over the entire testing process. It is evidently observed that both G-Cu 50/50 and G-Rubio 50/50 materials generally have fast responses and recoveries when exposing to chloroform (100%) in all five cycles. However, while most G-Cu 50/50 and G-Rubio 50/50 nanocomposites exhibit a relative stability in their responses, G-Cu 50/50 110 KΩ had unstable responses at the 3th and 4th cycles. Moreover, the response lines of all G-Cu 50/50 and G-Rubio 50/50 nanocomposites show their stable repeatability through five cycles. The sensitivities of these nanocomposites to chloroform are ranked: A_r (G-Cu 50/50 110 KΩ) > A_r (G-Cu 50/50 170 KΩ) > A_r (G-Rubio 50/50 1.46 MΩ) ~ A_r (G-Cu 50/50 145 KΩ) ~ A_r (G-Cu 50/50 110 KΩ).

Conclusion

The three different nanocomposite materials based on graphene and MOFs were successfully prepared by using shear mixing methods. The SEM and TEM images provide the evidence of the nanocomposite formation of pG-MOFs. Specifically, MOF nanoparticles with their diameters of HKUST-1 (20-50 nm), ZIF-8 (50-100nm) and Uio-66 (20-30nm) intercalated onto and between the graphene sheets. Also, there are some differences in the distribution of MOFs particles toward graphene sheets. To HKUST-1 and UiO-66 particles, the MOF particles intercalated and randomly distributed between graphene sheets, while ZIF-8 particles intercalated with a higher degree of agglomeration in graphene sheets and stacked on the surface of graphene. The XRD spectra of the pG-MOF nanocomposites show the sharp peak at ~27.4º, which confirms the presence of graphene in these nanocomposites. The sensing results show that all materials are sensitive to acetone, ethanol, methanol and chloroform, except for pG-ZIF-8 50/30 2.8 MΩ, which is insensitive to ethanol. G-Rubio 50/30 164 KΩ and G-Cu 50/30 76 KΩ nanocomposites exhibit their highest sensitivity and selectivity to acetone and ethanol respectively. Amongst G-Cu 50/50 and G-Rubio 50/50 nanocomposites, G-Cu 50/50 170 KΩ and G-Cu 50/50 110 KΩ are the most sensitive sensing materials for methanol and chloroform, respectively. Most of the mentioned nanocomposites show their high stabilities, repeatabilities and relatively fast responses.

References

1. Lu, G. and J.T. Hupp, *Metal−Organic Frameworks as Sensors: A ZIF-8 Based Fabry−Pérot Device as a Selective Sensor for Chemical Vapors and Gases.* Journal of the American Chemical Society, 2010. **132**(23): p. 7832-7833.
2. Kreno, L.E., J.T. Hupp, and R.P. Van Duyne, *Metal−Organic Framework Thin Film for Enhanced Localized Surface Plasmon Resonance Gas Sensing.* Analytical Chemistry, 2010. **82**(19): p. 8042-8046.
3. Dou, Z., et al., *Luminescent Metal–Organic Framework Films As Highly Sensitive and Fast-Response Oxygen Sensors.* Journal of the American Chemical Society, 2014. **136**(15): p. 5527-5530.
4. Koo, W.-T., et al., *Heterogeneous Sensitization of Metal–Organic Framework Driven Metal@Metal Oxide Complex Catalysts on an Oxide Nanofiber Scaffold Toward Superior Gas Sensors.* Journal of the American Chemical Society, 2016. **138**(40): p. 13431-13437.
5. Tung, T., et al., *Recent Advances in Sensing Applications of Graphene Assemblies and Their Composites*. 2017. 1702891.
6. Schedin, F., et al., *Detection of individual gas molecules adsorbed on graphene.* Nature Materials, 2007. **6**: p. 652.
7. Rumyantsev, S., et al., *Selective Gas Sensing with a Single Pristine Graphene Transistor.* Nano Letters, 2012. **12**(5): p. 2294-2298.
8. Chen, G., T.M. Paronyan, and A.R. Harutyunyan, *Sub-ppt gas detection with pristine graphene.* Applied Physics Letters, 2012. **101**(5): p. 053119.
9. Paul, R.K., et al., *Graphene Nanomesh As Highly Sensitive Chemiresistor Gas Sensor.* Analytical Chemistry, 2012. **84**(19): p. 8171-8178.
10. Zhao, Q., et al., *Synthesis and hydrogen storage studies of metal−organic framework UiO-66.* International Journal of Hydrogen Energy, 2013. **38**(29): p. 13104-13109.
11. Zhu, M., et al., *Room-Temperature Synthesis of ZIF-8: The Coexistence of ZnO Nanoneedles.* Chemistry of Materials, 2011. **23**(16): p. 3590-3592.
12. Tung, T.T., et al., *Graphene quantum resistive sensing skin for the detection of alteration biomarkers.* Journal of Materials Chemistry, 2012. **22**(40): p. 21754-21766.
13. Tung, T.T., et al., *Graphene–Fe3O4/PIL–PEDOT for the design of sensitive and stable quantum chemo-resistive VOC sensors.* Carbon, 2014. **74**: p. 104-112.

Chapter 6. Conclusions and future works

6.1 Conclusions

The content of the thesis contains the background of the development of graphene and its derivatives regarding structures, properties, synthesis methods, characterisations and potential applications which were discussed from the fundamental graphene materials and showcase the concepts for application. The main content of the thesis is the advanced graphene-MOF composites, which includes the L-rGO-C-MOF nanocomposites, HKUST-1@GQDs nanocomposites, and pG-MOF nanocomposites (pG-HKUST-1, pG-ZIF-8, and pG-UiO-66), have been successfully fabricated for high-performance supercapacitors, promising PL sensors, and chemical vapour sensors, respectively.

In the first chapter of the literature review, the fundamental information on the graphene and its derivatives, and MOF materials are introduced and analysed, showing the development of these materials and their applications. Graphene exhibits many excellent properties such as high thermal, electrical conductivity, electron mobility, and high transparent properties, which promote it as outstanding candidates for various practical applications. Its derivatives including GO, QGDs, element-doped graphene, and functionalized graphene, and MOF materials with their unique structures and high porosity, high surface area, and various functionalities on their structures are employed in many practical applications. An effective combination of graphene and MOF has created nanocomposites with their exceptional properties that are suitable to urgent demands for emerging applications such as sensing and supercapacitors.

In the second chapter, the methods for synthesis of graphene and its derivatives including pG, GO, and GQDs were described in details. They were all simple and scalable methods. Subsequently, the characterisations of nanocomposite materials were introduced, which provided insight studied nanoscale of designed hybrid materials.

Key outcomes are:

- Successful preparation of four key materials: pG, GO, GOQDs, and HKUST-1 MOF.
- Advanced characterisation techniques of these materials.

In the third chapter, the green, simple approach of the fabrication of a highly porous 3D-structured L-rGO-C-MOF nanocomposite has been demonstrated for the application of supercapacitor electrodes. With a high surface area and many active sites in the structure, the nanocomposite exhibits the high performance, delivering a high specific capacitance of 390 F/g at 5 mV/s and high specific power of 8037.5 W/kg at the specific energy of 22.3 Wh/kg. The improvements in specific energy and specific capacitance confirm that the synthesised nanocomposite materials have an excellent opportunity to apply in the energy storage devices. The content of the chapter is used to write a research paper, with the first author in the article.

Key outcomes are:

- Successful fabrication of porous L-rGO-C-MOF composite.
- Fabricated high-performing supercapacitors.
- Significantly improved specific energy of graphene-MOF supercapacitor.

In the fourth chapter, the GQDs and HKUST-1@GQDs nanocomposites were successfully synthesised, followed by their characterisations. GQDs materials were synthesised by the ultrasonic shearing method, and their diameters ranged from 100-120 nm, 65-85 nm to ~30-50 nm for 5 h, 10 h and 15 h sonicating, respectively, which confirms the effectiveness of the synthesis method. The synthesised HKUST-1@GQDs nanocomposites exhibit a high PL intensity in comparison with that of GQDs, suggesting that they have the potential to employ for photoluminescent sensors. Further study is needed to complete this work and possibly communicate the interesting data in a research paper.

Key outcomes are:

- Successful synthesis of GOQDs, and nanocomposite of HKUST-1@GOQDs.
- Complete measurement of GOQDs size.
- Characterisation of PL spectrum of the nanocomposites and its potential optical sensor application.

In the fifth chapter, three different MOFs of HKUST-1, ZIF-8, UiO-66 were combined with pG for the formation of the graphene-MOF nanocomposite, followed by their characterisations. The SEM and TEM images show the formation of three

nanocomposites, in which MOF-derived particles were intercalated into and onto the graphene matrix. The XRD shows the high crystalline of graphene at the 2θ-angle of 27.4º. The sensing results show that G-Rubio 50/30 and G-Cu 50/30 nanocomposites are highly sensitive and selective to acetone and ethanol, respectively. Amongst other G-Cu 50/50 and G-Rubio 50/50 materials, G-Cu 50/50 170 KΩ and G-Cu 50/50 110 KΩ are the most sensitive materials to methanol and chloroform, respectively. This research is currently improving and will be communicated in a research paper.

Key outcomes are:

- Successful synthesis of three nanocomposites of G-Cu, G-Rubio, and G-ZIF 8.
- Sufficient characterisation of these materials.
- Testing of vapour chemical sensing properties.

6.2 Future works

As demonstrated from the presented research outcomes in the thesis, graphene-based composite materials have immense potentials for multifunctional applications in many fields of sensing and energy storage. Their unique structure and outstanding physical and chemical properties have promoted them ideal materials for making the new generation of graphene-based nanocomposites, which meet the urgent demands of both lightweight, flexible and wearable devices with high performance for energy storage devices, and ultrafast, highly sensitive, selective sensing devices. Furthermore, inexpensive materials and their availability of material sources are also a priority in fabricating the new generation of the graphene-based nanocomposites. Therefore, future works are:

1. Supercapacitor applications

In addition to the work in this thesis, three feasible ways can be employed to improve the supercapacitor performance including:

+ Strategy 1: Fabrication of graphene-MOF nanocomposite for supercapacitors can use other types of MOFs (ZIF-8 or UiO-66) due to their higher chemical stability. The 3D composite structures can be formed without any MOF structure damage, which is convenient for electrolyte ions to transport. This offers the use of other strong electrolytes such as H_2SO_4 acid, which can substantially improve the capacitance of supercapacitors.

+ Strategy 2: The post-treatment techniques of graphene-MOF nanocomposites can be plasma or thermal annealing, with the purpose of maintaining the inital structure of HKUST-1.

+ Strategy 3: The fabricated nanocomposite can be functionalized with a conducting polymer (CP) through the polymerization to enhance the electrical conductivity of the whole composite. The CPs work as binders to connect the graphene sheets, which can generally enhance the performance of supercapacitors.

2. PL sensors

+ Plan 1: Improvement of GQDs size: besides the synthesis method of GQDs mentioned; GQDs can be synthesised via chemical route, as recently reported to optimise the particle size, and therefore, enhance the QY and attachment of GQDs on HKUST-1 microrods.

+ Plan 2: The preparation methods of HKUST-1: HKUST-1 microrods can be grown in the natural way simply by immerging HKUST-1 diamonds in miliQ water for about 24 h to obtain the fine microrods.

3. Chemical vapour sensor

+ Strategy 1: The preparation method of G-MOF can be modified by using ball milling technique to intercalate the MOFs into graphene sheets.

+ Strategy 2: The sensing testing can be conducted on other volatile organic compounds (VOCs) to expand the applications.